

# Modeling Phase Separation in Grain-Fluid Mixture Flows by a Depth-Averaged Approach With Dilatancy Effects



### Key Points:

- Description of different flow regimes occurring simultaneously in grain-fluid mixture flows as a result of phase separation
- Description of the granular or fluid mass transfer between different flow regimes taking into account the granular dilatancy effect
- Modeling of the different granular frictional behaviors in pure grain and saturated mixture regimes using different rheological models

### Correspondence to:

Y. Wang,  
[wang@fdy.tu-darmstadt.de](mailto:wang@fdy.tu-darmstadt.de)

### Citation:



Sun, W., & Wang, Y. (2024). Modeling phase separation in grain-fluid mixture flows by a depth-averaged approach with dilatancy effects. *Journal of Geophysical Research: Earth Surface*, 129, e2023JF007416. <https://doi.org/10.1029/2023JF007416>

Received 29 AUG 2023

Accepted 21 OCT 2024

### Author Contributions:

**Conceptualization:** Weihang Sun, Yongqi Wang  
**Funding acquisition:** Yongqi Wang  
**Investigation:** Weihang Sun, Yongqi Wang  
**Methodology:** Weihang Sun, Yongqi Wang  
**Project administration:** Yongqi Wang  
**Supervision:** Yongqi Wang  
**Validation:** Weihang Sun, Yongqi Wang  
**Visualization:** Weihang Sun  
**Writing – original draft:** Weihang Sun  
**Writing – review & editing:** Yongqi Wang

Weihang Sun<sup>1</sup>  and Yongqi Wang<sup>1</sup> 

<sup>1</sup>Chair of Fluid Dynamics, Department of Mechanical Engineering, Technical University of Darmstadt, Darmstadt, Germany

**Abstract** In this work, we propose a comprehensive two-layer depth-averaged model to study the dynamic behavior of grain-fluid mixtures, which considers the granular dilatancy effects and the different frictional rheologies of grains in different states. Unlike single-phase flows, not only the interaction between granular and fluid phases significantly influence the dynamics of mixtures, but also the phase separation, so that different flow regimes can occur. These include five different possible regimes: two-layer regimes of (a) under-saturated mixture and (b) over-saturated mixture as well as single-layer regimes of (c) saturated mixture, (d) pure grains and (e) pure fluid. Most depth-averaged models in previous studies have considered only one of these flow regimes. The present model is an improved and integrated version of these depth-averaged models. Taking into account that the pure grains and pure fluid in the upper layer, which occur in the regimes of the under-saturated and over-saturated grain-fluid mixtures, respectively, exhibit different flow features than in the lower layer of the saturated mixture, we use a two-phase two-layer depth-averaged model to describe these regimes. This proposed model is possibly the first to employ a two-layer structure to describe all possible different flow regimes simultaneously. The proposed model is then solved numerically using a high-resolution central-upwind scheme and shows its ability to handle different flow regimes. To demonstrate the robustness of the numerical implementation and to evaluate the performance of the model, the numerical results are compared with several experiments reported in the literature, showing a certain qualitative agreement.

**Plain Language Summary** Debris flows are moving mixtures of grains and fluid. Phase separation between grains and fluid is a significant feature in grain-fluid mixture flows, leading to different flow regimes during their dynamic motion, such as fluid-saturated, over-saturated, under-saturated granular mixtures, as well as pure fluid and pure granular regimes. A model is essential to comprehensively describe the emergence, transition, and disappearance of these different flow regimes. Most models in previous studies include only one flow regime and cannot describe the different flow regimes and their transition. In this study, we propose a two-layer depth-averaged model to simultaneously consider all possible flow regimes and their dynamic transition. This two-layer depth-averaged model can qualitatively describe experimental results and is promising for the study of natural geophysical flows in the future.

## 1. Introduction

Grain-fluid mixture flows are complex systems that exhibit different behavior compared to pure grain flows. The dynamics of these flows are influenced by various factors, including the relative motion between the granular and fluid phases, the size of the particles, and the interaction forces between both phases. These flows have been extensively studied due to their applications in various industrial processes and their ability to cause natural hazards, such as landslides, submarine avalanches, and debris flows. Debris flows are extremely dangerous and destructive natural phenomena, as large masses of rock, soil and water flow down slopes at high speed due to gravity. As highlighted in many previous studies (Iverson, 1997; Savage & Iverson, 2003; Vallejo, 1997; Zanuttigh & Lamberti, 2007), one of the most destructive features of debris flows is the initial deep surge, which consists of under-saturated, coarse-grained material that is notably drier than the main part of the flow. More recently, Meng et al. (2022) further emphasized and investigated this distinctive feature of debris flows. In their study, they referenced a debris flow event in Aconcagua Park, Argentina, on 27 January 2015. During this event, the front of the flow exhibited the characteristics of a deep surge, containing boulders and larger particles (see Figure 1a in their work). Following the bouldery surge, the flow gradually decreased in height and transitioned to a more watery state (Figure 1b in their work). Another catastrophic debris flow events in Oso, Washington, in March 2014 resulted in the loss of 43 lives and extensive damage to homes and infrastructure (see Iverson

© 2024. The Author(s).

This is an open access article under the terms of the [Creative Commons Attribution License](https://creativecommons.org/licenses/by/4.0/), which permits use, distribution and reproduction in any medium, provided the original work is properly cited.

et al., 2015; Wartman et al., 2016). Hence, understanding and predicting grain-fluid mixture flows is crucial for minimizing harm to individuals and infrastructure.

In the past two decades, numerous experimental and numerical studies have been conducted on grain-fluid mixture flows. Despite this, developing an accurate and rigorous model to describe the dynamics of these flows remains a significant challenge. The works of Iverson (1997) and Iverson and Denlinger (2001) examined the behavior of debris flows composed of cohesionless grains and viscous fluids, and showed that the presence of interstitial fluid significantly modifies the dynamics of the mixtures and should be considered in the constitutive laws of the flows. In their model, the difference between granular and fluid velocities was negligible, and they only generalized the Savage and Hutter theory for pure granular flows (e.g., Savage & Hutter, 1989) to include the effects of viscous pore fluid with varying pressure.

The US Geological Survey (USGS) conducted large-flume experiments (see Iverson et al., 2000) that revealed loosely packed fluid-saturated granular material accelerates rapidly when the pore fluid pressure exceeds a threshold value, whereas in densely packed case, the material deforms slowly and moves intermittently. Additionally, experiments of underwater granular flows (see e.g. Pailha et al., 2008; Pailha & Pouliquen, 2009; Rondon et al., 2011) provide evidence for fast-moving and slow-moving underwater granular flows that differ only in their initial solid volume fraction. Boyer et al. (2011) studied the rheology of dense suspensions using an original pressurized shear cell in which particles suspended in a fluid of viscosity  $\eta_f$  were sheared at constant particle pressure  $P^p$ . They showed that dense suspensions exhibit a visco-plastic behavior similarly to granular media, successfully described by a friction rheology and fully characterized by the evolution of the friction coefficient  $\mu$  and the solid volume fraction  $\phi$  with a dimensionless viscous number  $I_v$ . Furthermore, Pellegrino et al. (2014) extended this rheology to include granular-fluid mixture flows with a particle density greater than that of the interstitial viscous fluid.

De Haas et al. (2015) conducted small-scale debris flow experiments and discovered that the composition of debris flows significantly impacts depositional processes, runout, and deposit shape. Leonardi et al. (2015) reported experiments using a rotating drum and showed that the process of phase segregation is an important feature in grain-fluid mixtures. It was observed that at high drum speeds, an under-saturated mixture region occurred at the front, whereas at low drum speeds, the fluid moved ahead of the particle front, leading to the formation of an over-saturated mixture or a pure fluid front (see Figure 2 and Figure 5 in their work), which was consistent with the findings of Kaitna et al. (2011). Laboratory experiments of subaerial fluid-saturated granular collapses were investigated by Bougouin et al. (2019). They showed that the trigger of the collapse and the shape of the final deposit are mostly influenced by the viscosity of the interstitial fluid, the size of the grains, the geometry of the initial column and the initial solid volume fraction. Additionally, He et al. (2022) examined the impact of interstitial water on the collapse of partially saturated granular columns by experimental and numerical methods, and the results indicated that the presence of interstitial water accelerates the collapse of columns with coarse grains but slows it down for columns made up of fine particles. Taylor-Noonan et al. (2022) conducted a series of down-slope experiments to compare the behavior of identical granular-material in a dry and a saturated initial state, where the granular material was selected with a large enough grains size to limit the effects of the interstitial fluid to buoyancy and drag only. The results demonstrate that the existence of a pore fluid significantly increases the mobility of saturated granular flows compared to dry ones.

In addition to experimental studies on the behavior of grain-fluid mixture flows, various theoretical models have been proposed to explain their dynamics. Trujillo-Vela et al. (2022) provided a comprehensive overview of the different mathematical modeling approaches for debris flows. In most geophysical applications, the length of debris flows is greater than their thickness, which justifies the use of depth-averaged theory to describe the dynamics of grain-fluid mixture flows. Depth-averaged theories take advantage of the fact that the typical flow thickness  $H$  is much smaller than the typical flow length  $L$ , enabling an asymptotic expansion to be performed with respect to aspect ratio  $\varepsilon = H/L \ll 1$  for mass and momentum balance equations. Depth-averaged theories have been widely applied to various types of flows, such as flood flows (e.g., Abril & Knight, 2004; Mignot et al., 2006), snow avalanche flows (e.g., Gray & Edwards, 2014; Savage & Hutter, 1989), debris flows (e.g., Bouchut et al., 2016, 2017; Iverson, 1997; Meng & Wang, 2018), and submarine granular flows (e.g., Bouchut et al., 2016, 2017; Fernández-Nieto et al., 2008; Sun et al., 2023).

The model proposed by Pitman and Le (2005) extends the depth-averaged, quasi single-phase mixture model of Iverson (1997) and Iverson and Denlinger (2001) to a two-phase depth-averaged approach, in which each phase of fluid and grains has its own velocity. The interaction force between the granular and fluid phases is accounted for by a Darcy model. Furthermore, Pelanti et al. (2008, 2011) solved the model proposed by Pitman and Le (2005) numerically using a Roe-type scheme and a Riemann solver, respectively. Later on, Bouchut et al. (2015) showed that a closure relation was missing in these models. Apart from interactions like buoyancy and drag forces between the granular and fluid phases, the dilatancy effects of the particles also have a significant impact on the motion of grain-fluid mixture flows. The change in solid volume fraction due to dilatation or compaction of the particles within the saturated mixture under shear results in relative motion between the grains and the fluid perpendicular to the flow direction and pore fluid pressure gradient, which can in turn affect the deformation of the saturated mixture. This coupling between the dilatancy effect of the particles and the pore fluid pressure has been extensively investigated in numerous previous studies (see e.g. Baumgarten & Kamrin, 2019; Bouchut et al., 2016, 2017; Iverson, 2005; Iverson & George, 2014; Iverson et al., 2009; Meng & Wang, 2018; Pailha & Pouliquen, 2009; Sun et al., 2023). In these studies, Iverson (2005) assumed a constant dilatancy angle in their model, while the other studies employed a critical state theory to model the granular dilatancy angle. Kowalski and McElwaine (2013) considered the internal sedimentation and resuspension of particles in a fluid-saturated grain mixture and developed a depth-averaged model in which the balance laws for mass and momentum are extended by a depth-averaged particle concentration equation. Iverson and George (2014) particularly focused on the motion of fluid-saturated sediments, in which the percolation of the fluid through the skeleton of grains in the flow direction is not considered, but the relative motion between grains and fluid perpendicular to the flow direction, caused by the granular dilatancy effect, is modeled. As their model is a single-layer model, they introduced a virtual surface to account for the fluid mass transfer induced by the particle dilation rate, but the solid and fluid mass are not conserved in their model. Moreover, Meng and Wang (2018) extended the work of Iverson and George (2014) by using a depth-averaged two-velocity grain-fluid mixture model in which the velocity difference between the granular and fluid phases is coupled with the granular dilatancy.

In many natural applications, grain-fluid mixture flows are over-saturated or under-saturated, at least in sub-regions where a fluid-saturated granular lower layer is overlain by a pure fluid or a pure grain upper layer (see Iverson et al., 2010; Meng et al., 2022; Tai et al., 2019; Taylor-Noonan et al., 2022). Some two-layer depth-averaged models have been developed to analyze such grain-fluid mixture flows. Bouchut et al. (2016) combined the averaging theory of Anderson and Jackson (1967) and the dilatancy law of Roux and Radjai (2001) to develop a two-phase two-layer depth-averaged model to describe debris flows and underwater granular flows. This model accounts for both horizontal and vertical percolation of fluid through the granular matrix. The fluid exchange between the layers depends on the dilatancy effects of particles and the velocity differences between the grains and fluid in the flow direction. In order to compare their numerical simulations with the uniform flow experiments of Pailha and Pouliquen (2009), they simplified their model in the numerical implementation and captured the different flow behavior of initially loosely and densely packed underwater granular flows. Later, in Bouchut et al. (2017), they applied this model to simulate the submarine granular collapse experiments of Rondon et al. (2011). Meng et al. (2017) proposed a two-phase two-layer depth-averaged model to investigate the dynamics of an under-saturated grain-fluid mixture flow, where a fluid-saturated granular layer is overlaid by pure granular material. The model considers the transfer of granular mass at the interface between the upper and lower layers and treats the granular material in both layers as a frictional Coulomb-like continuum, but neglects the granular dilatancy effects.

More recently, Meng et al. (2022) developed a new depth-averaged mixture theory for debris flows, based on experimental observations by Davies (1990) and Johnson et al. (2012), which combines shear-induced transport and relative motion between the solid and fluid phases. Their model describes separate free surfaces for water and grains, hence allows for both over-saturated and under-saturated flows where the water free surface lies above or below the free surface of the grains. Subsequently, Meng et al. (2024) used their model to simulate the large-landslide flume experiments of Taylor-Noonan et al. (2022). However, the assumption of a constant and uniform solid volume fraction in their model throughout the granular phase precludes the effect of the excess pore fluid pressure. Sun et al. (2023) introduced a two-layer depth-averaged model and considered granular dilatancy effects to investigate submarine landslides and the resulting water waves, but assumed a shallow depth in the direction perpendicular to the flow for both the lower layer of the avalanche mixture and the upper layer of pure water. For the numerical implementation, they reformulated their model in a global coordinate system so that the

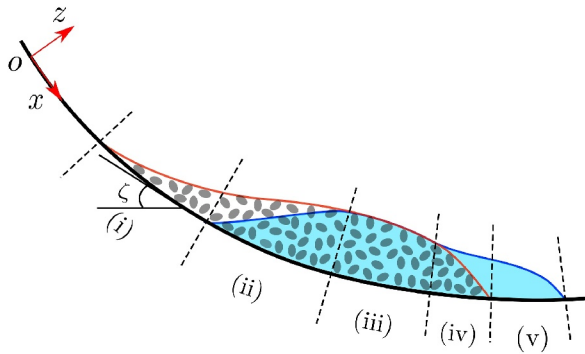


**Figure 1.** Schematic diagram of a typical grain-fluid mixture flow sliding down a plane inclined at an angle  $\zeta$  to the horizontal. In a general grain-fluid mixture flow, different flow states can occur, for example, (i) a pure grain regime, (ii) an under-saturated mixture regime consisting of a saturated mixture lower layer and a pure granular upper layer, (iii) a saturated mixture regime, (iv) an over-saturated mixture regime including a saturated mixture lower layer and a pure fluid upper layer, and (v) a pure fluid regime. The fluid region is shaded in blue and its surface is marked by blue line, while the granular surface is indicated by red line. A terrain-following coordinate system  $oxz$  is defined with the  $x$ -coordinate along the downslope direction and the  $z$ -coordinate pointing to the normal direction of the topography.

numerical solutions are insensitive to the choice of discretization of nonconservative products. However, it was shown in the model of Delgado-Sánchez et al. (2020) that change of reference frame should be done for the avalanche (in a topography-related reference frame) and water layer (in a Cartesian horizontal/vertical frame). Furthermore, Poulain et al. (2023) conducted a numerical and experimental investigation of landslide-generated tsunamis. They proposed a two-layer HySea model in which depth-averaging was performed in a Cartesian horizontal/vertical coordinate system for both the granular and water layers. Their model accounted for the (non-hydrostatic) dispersion effect in the propagation of water waves, but not the granular dilatancy effects.

Inspired by the works conducted by Luca et al. (2012), Bouchut et al. (2016), and Sun et al. (2023) on over-saturated mixture flows and Meng et al. (2017) on under-saturated mixture flows, the aim of this paper is to develop a two-layer depth-averaged model that is an improved and integrated version of previously proposed depth-averaged models to simultaneously consider all possible flow regimes and their dynamic transitions. As shown in Figure 1, five different flow regimes may occur in a general grain-fluid mixture flow, including (a) the pure grain regime, (b) the under-saturated mixture regime, (c) the saturated mixture regime, (d) the over-saturated mixture regime and (e) the pure fluid regime. We begin by introducing the sets of the governing equations describing the saturated grain-fluid mixture, the pure granular flow

and the pure fluid flow, respectively. Then, we perform a depth integration of these governing equations for the over-saturated and under-saturated mixture regimes over the lower layer of the saturated mixture and over the upper layer of the pure grains or the pure fluid, respectively, for which the corresponding boundary conditions at the bottom and at the free surface, as well as the jump conditions at the layer interface are incorporated. This results in the two-layer depth-averaged governing equations for the saturated grain-fluid mixture in the lower layer and for the pure grains or the pure fluid in the upper layer in the under-saturated and over-saturated mixture regimes. The depth-averaged mass and momentum balance equations for the simple single-layer regimes, including the saturated mixture, the pure fluid and the pure granular regime, can be obtained by the corresponding degeneracy of the two-layer depth-averaged mass and momentum balance equations for the under-saturated and over-saturated mixture regimes. These depth-averaged equation sets, each appropriate for different flow regimes, can together comprehensively describe the dynamics of the different flow regimes, including their emergence, transition, and disappearance. It should be emphasized that the derived single-layer depth-averaged models closely resemble the classical models for pure grains, pure fluid, and saturated grain-fluid mixtures. Moreover, the two-layer models presented in this study share similarities with the models proposed by Luca et al. (2012), Bouchut et al. (2016), Meng et al. (2017), and Sun et al. (2023), although some significant differences exist. In addition, the two-layer depth-averaged model can independently describe the different flow behaviors of a single medium (pure grains or pure fluid) in the upper layer and a saturated grain-fluid mixture in the lower layer. This feature distinguishes the present model from that proposed by Meng et al. (2022), which can also describe the flow dynamics in different regimes using a single-layer approach. Table 1 summarizes the main features of several widely recognized depth-averaged models that are used in different flow regimes. This overview by no means claims to be an exhaustive description of the various models, but is merely intended to show some modeling examples that are closely related to the model proposed here in the corresponding flow regimes. The present study introduces an innovation by using a two-phase two-layer depth-averaged model to simultaneously capture the flow dynamics of the different flow regimes that can occur simultaneously in a granular-fluid mixture flow. In addition, our model incorporates the granular dilatancy effect in the saturated mixture region. In contrast to most previous studies that used only a single granular rheology, we utilize a  $\mu(I)$  rheology in the pure grain region and a  $\mu(I_v)$  rheology in the saturated mixture region. The similarities and differences between our present model and several previously proposed relevant models are presented and explained in detail in Section 2.9. We then apply a high-resolution central-upwind scheme to numerically solve the depth-averaged model for different flow regimes simultaneously. To achieve the transformation of the depth-averaged model for the different flow regimes in the entire computational domain, specific assessment conditions are incorporated in our numerical scheme to determine which flow regime occurs in each computational cell for each time step. To validate the

**Table 1**  
*List of Several Depth-Averaged Models Suitable for the Different Flow Regimes, Labeled (i)–(v) in Figure 1*

Flow	Reference	Phase	Layer	Dilatancy	Rheological model	
					Grains	Fluid
(i)	Savage and Hutter (1989)	Single	Single	–	Coulomb	–
	Gray and Edwards (2014)	Single	Single	–	$\mu(I)$	–
	Bouchut et al. (2021)	Single	Single	✓	$\mu(I)$	–
(ii)	Meng et al. (2017)	Two	Two	–	Coulomb	Na
(iii)	Iverson and Denlinger (2001)	Mix	Single	–	Coulomb	N
	Pitman and Le (2005)	Two	Single	–	Coulomb	–
	Iverson and George (2014)	Mix	VS	✓	Coulomb	N
(iv)	Meng and Wang (2016)	Two	–	–	Coulomb	N + Na
	Meng and Wang (2018)	Two	VS	✓	Coulomb	N + Na
	Fernández-Nieto et al. (2008)	Mix	Two	–	Coulomb	Chézy
	Pailha and Pouliquen (2009)	Two	Single	✓	Coulomb	–
	Luca et al. (2012)	Two	Two	–	Coulomb	Chézy
(v)	Bouchut et al. (2016, 2017)	Two	Two	✓	Coulomb	Na
	Sun et al. (2023)	Mix	Two	✓	Coulomb	N
	Chertock et al. (2015)	Single	Single	–	–	Chézy + Ma
(i)–(v)	Meng et al. (2022, 2024)	Two	Single	–	$\mu(I)$	Chézy + Ma
	Present study	Two	Two	✓	$\mu(I, I_v)$	Chézy + Ma

*Note.* The abbreviations used in the table are: Single: Single-phase/layer model; Two: Two-phase/layer model; Mix: Mixture model; VS: Virtual free surface; Coulomb: Coulomb friction model;  $\mu(I)$ :  $\mu(I)$  rheology;  $\mu(I_v)$ :  $\mu(I_v)$  rheology; N: Newtonian fluid law; Na: Navier fluid friction condition; Chézy: Chézy formula; Ma: Manning formulation. Most of their physical meanings will become clear in the following sections.

numerical implementation and evaluate the performance of the proposed two-layer depth-averaged model, we compare the simulated results with data obtained from several previous experimental studies.

## 2. Field Formulation

As shown in Figure 1, in a grain-fluid mixture flow, saturated mixture, pure fluid and pure granular regions can occur simultaneously. These regions interact with each other at their interfaces and exchange mass, resulting in phase separation. The corresponding governing equations and boundary conditions, in particular the jump conditions at the interfaces, are described in this section.

### 2.1. Saturated Mixture Theory

In order to precisely describe the dynamics of grain-fluid saturated mixture flows, it is necessary to consider the interaction between the solid and fluid phases using the mixture theory of continuum mechanics (see Bouchut et al., 2016; Iverson, 1997; Jackson, 2000; Meng & Wang, 2016; Pitman & Le, 2005; Truesdell, 1984). According to the mixture theory, every point in space is assumed to be occupied simultaneously by both phases with the individual volume fractions denoted by  $\phi^\alpha$ , where  $\alpha = s, f$  represents the solid and fluid phases, respectively. For a grain-fluid saturated mixture,  $\phi^f + \phi^s = 1$ . The mixture theory can describe the dynamics of each constituent using the individual mass and momentum balance equations, which are given as follows:

$$\frac{\partial \rho^\alpha}{\partial t} + \nabla \cdot (\rho^\alpha \mathbf{u}^\alpha) = 0, \quad (1)$$

$$\frac{\partial}{\partial t}(\rho^\alpha \mathbf{u}^\alpha) + \nabla \cdot (\rho^\alpha \mathbf{u}^\alpha \otimes \mathbf{u}^\alpha) = \nabla \cdot \boldsymbol{\sigma}^\alpha + \rho^\alpha \mathbf{g} + \boldsymbol{\beta}^\alpha, \quad (2)$$

where  $\varrho^\alpha$  denotes the partial density, which is related to the intrinsic or true density  $\varrho^{\alpha*}$  by  $\varrho^\alpha = \varrho^{\alpha*} \phi^\alpha$ . The term “partial” refers to the physical properties of either the granular or the fluid constituent within the mixture, while the term “intrinsic” refers to the physical properties of the granular material or the fluid on its own, independent of the mixture. In the present application, it is assumed that the intrinsic density  $\varrho^{\alpha*} = \text{const.}$  for both the granular and fluid constituents. The partial velocity, denoted by  $\mathbf{u}^\alpha$ , is equal to the intrinsic velocity, that is,  $\mathbf{u}^\alpha = \mathbf{u}^{\alpha*}$ .  $\boldsymbol{\sigma}^\alpha$  represents the partial stress, and  $\boldsymbol{\beta}^\alpha$  is the interaction force acting on the  $\alpha$  phase.

The partial stress tensor of the fluid phase  $\boldsymbol{\sigma}^f$ , can be expressed as

$$\boldsymbol{\sigma}^f = -\phi^f p^{f*} \mathbf{1} + \boldsymbol{\tau}^f, \quad (3)$$

in which  $p^{f*}$  represents the pore fluid pressure and  $\boldsymbol{\tau}^f$  denotes the fluid deviatoric stress obeying Newtonian fluid law, given by

$$\boldsymbol{\tau}^f = \phi^f \eta^f (\nabla \mathbf{u}^f + (\nabla \mathbf{u}^f)^T), \quad (4)$$

where  $\eta^f$  stands for the dynamic viscosity. The partial fluid deviatoric stress has been assumed to be proportional to its local fluid volume fraction (see Nunziato et al., 1986). The partial granular stress  $\boldsymbol{\sigma}^s$  can be defined as

$$\boldsymbol{\sigma}^s = -\phi^s p^{f*} \mathbf{1} - \boldsymbol{\sigma}^e, \quad (5)$$

where  $\boldsymbol{\sigma}^e$  denotes the solid effective stress, as introduced by Terzaghi (1943), and it has an opposite sign to that of the Cauchy stress. The interaction drag usually takes the form

$$\boldsymbol{\beta}^s = -\boldsymbol{\beta}^f = p^{f*} \nabla \phi^s + C^d (\mathbf{u}^f - \mathbf{u}^s), \quad (6)$$

in which the first term on the right-hand side  $p^{f*} \nabla \phi^s$  combined with  $-\nabla(\phi^s p^{f*})$  after substituting (5) and (6) into (2) yields  $-\phi^s \nabla p^{f*}$ , commonly known as the buoyancy force in classical fluid mechanics. The second term on the right-hand side represents the Darcy drag acting on particles, where  $C^d$  denotes the drag coefficient. Various studies have proposed different formulations for this drag coefficient (see Bouchut et al., 2016; Iverson, 1997; Meng & Wang, 2016; Meng et al., 2017; Pailha & Pouliquen, 2009; Pitman & Le, 2005; Pudasaini, 2012). In our study, we adopt the formulation of the drag coefficient from Pailha and Pouliquen (2009), as given by

$$C^d = \frac{\eta^f (\phi^f)^2}{k}, \quad \text{where the permeability is } k = \frac{(\phi^f)^3 d^2}{150 (\phi^s)^2}, \quad (7)$$

and  $d$  represents the grain diameter.

After substituting the constitutive laws (3) and (5) as well as the interaction drags (6) into (2), the momentum balance equations for the solid and fluid phases can be expressed as follows:

$$\frac{\partial}{\partial t} (\varrho^s \mathbf{u}^s) + \nabla \cdot (\varrho^s \mathbf{u}^s \otimes \mathbf{u}^s) = -\nabla \cdot \boldsymbol{\sigma}^e - \phi^s \nabla p^{f*} + \varrho^s \mathbf{g} + C^d (\mathbf{u}^f - \mathbf{u}^s), \quad (8)$$

$$\frac{\partial}{\partial t} (\varrho^f \mathbf{u}^f) + \nabla \cdot (\varrho^f \mathbf{u}^f \otimes \mathbf{u}^f) = \nabla \cdot \boldsymbol{\tau}^f - \phi^f \nabla p^{f*} + \varrho^f \mathbf{g} - C^d (\mathbf{u}^f - \mathbf{u}^s). \quad (9)$$

These momentum balance equations are analogous to those employed to investigate debris flows by Iverson and Denlinger (2001), Bouchut et al. (2016, 2017), Meng and Wang (2016); Meng and Wang (2018) and Meng et al. (2022), underwater granular avalanches by Pailha and Pouliquen (2009), Bouchut et al. (2016, 2017) and general fluid-sediment flows by Baumgarten and Kamrin (2019).

## 2.2. Single Phase Governing Equations

The mass and momentum balance Equations 1, 8, and 9 obtained from the two-phase saturated mixture theory can be simplified to the balance equations that describe the dynamics of a single phase flow, such as the pure grain flow or the pure fluid flow, which are presented below.

### 2.2.1. Pure Grain Flow

In a pure grain flow, the fluid phase vanishes,  $\phi^f = 0$ , and the solid volume fraction  $\phi^s$  is less than or equal to the maximum solid volume fraction  $\phi_{\max}^s = 0.675$  corresponding to the closest packing of identical spherical grains (see Meng et al., 2017). The buoyancy force  $-\phi^s \nabla p^{f*}$  and the interaction force  $C^d(\mathbf{u}^f - \mathbf{u}^s)$  in Equation 8 vanish. Consequently, the mass and momentum balance equations simplify to

$$\frac{\partial \varrho^s}{\partial t} + \nabla \cdot (\varrho^s \mathbf{u}^s) = 0, \quad (10)$$

$$\frac{\partial}{\partial t}(\varrho^s \mathbf{u}^s) + \nabla \cdot (\varrho^s \mathbf{u}^s \otimes \mathbf{u}^s) = -\nabla \cdot \boldsymbol{\sigma}^e + \varrho^s \mathbf{g}. \quad (11)$$

If the granular dilatancy effect is not considered in a grain flow, the solid volume fraction  $\phi^s$  is assumed to be constant. Together with  $\varrho^{s*} = \text{const}$  and  $\phi^s = \text{const}$ , Equations 10 and 11 can be further reduced to those as described by Savage and Hutter (1989).

### 2.2.2. Pure Fluid Flow

Similarly, in a pure fluid flow,  $\phi^f = 1$ ,  $\phi^s = 0$ , and the interaction force vanishes. With the assumption of incompressibility  $\varrho^{f*} = \text{const}$ , Equations 1 and 9 are reduced to the mass and momentum balance equations of an incompressible fluid

$$\nabla \cdot \mathbf{u}^f = 0, \quad (12)$$

$$\varrho^{f*} \left\{ \frac{\partial \mathbf{u}^f}{\partial t} + \nabla \cdot (\mathbf{u}^f \otimes \mathbf{u}^f) \right\} = \nabla \cdot \boldsymbol{\tau}^f - \nabla p^{f*} + \varrho^{f*} \mathbf{g}. \quad (13)$$

They are the Navier-Stokes equations for a Newtonian fluid with the constitutive law (4).

## 2.3. Dilatancy Model

Granular dilatancy refers to the phenomenon that occurs in granular materials when they are subjected to shearing stresses. Granular materials tend to dilate or contract when sheared. This behavior arises due to the rearrangement of particles within the material, which can cause a change in the solid volume fraction. The granular dilatancy effect is of particular importance in the study of grain-fluid mixtures, as it can significantly influence the flow dynamics and the interactions between the granular and fluid phases. Experiments by Iverson et al. (2000) and Pailha et al. (2008) have demonstrated its importance. Following Bouchut et al. (2016), the granular dilatancy effect has been modeled by Roux and Radjai (1997) and Roux and Radjai (2001) using the following equation:

$$-\frac{1}{\phi^s} \frac{d\phi^s}{dt} = \dot{\gamma}^s \tan \psi, \quad (14)$$

where  $\psi$  is the so-called dilatancy angle,  $\dot{\gamma}^s$  the shear rate of the granular material, and  $d/dt$  represents the substantial derivative.

Eliminating the substantial derivative on the left-hand side of Equation 14 using the granular mass balance Equation 10 yields

$$\nabla \cdot \mathbf{u}^s = \dot{\gamma}^s \tan \psi. \quad (15)$$

This equation shows that the behavior of the granular material under shear determines the sign of the dilatancy angle. When the particles dilute under shear, the dilatancy angle is positive ( $\psi > 0$ ). Conversely, the dilatancy angle is negative ( $\psi < 0$ ) when the particles contract under shear. Furthermore, in a grain-fluid saturated mixture the combination of the mass balance equations for the granular and fluid phases, that is, Equation 1 for  $\alpha = s, f$ , implies that shear-induced granular dilatancy is also influenced by the relative motion between the two phases by

$$\nabla \cdot [\phi^f (\mathbf{u}^s - \mathbf{u}^f)] = \dot{\gamma}^s \tan \psi. \quad (16)$$

Roux and Radjai (1997) assumed that the dilatancy angle  $\psi$  is proportional to the difference between the actual solid volume fraction  $\phi^s$  and the equilibrium packing fraction  $\phi^{eq}$  corresponding to the steady state, expressed as

$$\tan \psi = K_3 (\phi^s - \phi^{eq}), \quad (17)$$

where  $K_3$  is a non-dimensional parameter. Moreover, Pailha and Pouliquen (2009) proposed a granular rheology for the viscous regime in which  $\phi^{eq}$  is a decreasing function of viscous number  $I_v = \eta^f \dot{\gamma}^s / p^p$ , where  $p^p$  is the pressure acting on grains. The relation between  $\phi^{eq}$  and  $I_v$  can be given by

$$\phi^{eq} = \phi^c - K_2 I_v, \quad (18)$$

where  $\phi^c$  is the critical volume fraction observed when a continuous quasi-static deformation occurs. This parameter  $\phi^c$  determines if the initial packing is dense or loose. The parameter  $K_2$  controls the compactness of particles under steady shear and will be calibrated in the subsequent numerical simulations.

Nevertheless, in the case of pure grain flows, the contribution of dilatancy effect to their dynamics is less pronounced in comparison to that of grain-fluid saturated mixture flows (Bouchut et al., 2021). This is due to the fact that, on the one hand, the solid volume fraction of pure grain flows undergoes only a small variation during the flow in comparison with grain-fluid saturated mixture flows, on the other hand, the absence of the fluid phase precludes any coupling between the dilatancy effect of the particles and the pore fluid pressure. Our test simulations have also demonstrated this behavior. Therefore, for simplicity, the dilatancy effect of the particles is not taken into account in regions of pure granular materials, that is, in the pure grain regime and in the pure granular upper layer of the under-saturated mixture regime. The dilatancy effect is considered only in the grain-fluid saturated mixture regions.

#### 2.4. Boundary Conditions

The present study employs a terrain-following curvilinear coordinate system  $oxz$ , where the  $x$ -axis follows the topography and the  $z$ -axis points in the normal direction of the basal surface, as illustrated in Figure 1. For simplicity, we assume that the flow is uniform in the lateral direction. The model can be easily extended to include a flat lateral coordinate, if required (Gray et al., 1999; Wang et al., 2004; Wieland et al., 1999). However, it should be emphasized that incorporating curvature effects is essential when applying the model to simulate real events, as describe and shown by Bouchut and Westdickenberg (2004) and Peruzzetto et al. (2021). Figure 2 illustrates the vertical structures of different possible regimes in a general grain-fluid mixture flow, as shown in Figure 1. The grain free surface is defined by  $F^s(x, z, t) = z - \xi^s(x, t) = 0$ , the fluid free surface by  $F^f(x, z, t) = z - \xi^f(x, t) = 0$ , and the basal surface by  $F^b(x, z) = z - b(x) = 0$ . Here, if needed, a complex shallow three-dimensional basal topography can be introduced by its elevation  $z = b(x)$  above the reference coordinate surface  $z = 0$ . For the later derivation of the depth-averaged governing equations, we will assume  $b(x) = 0$ . The interface  $F^i(x, z, t) = z - \xi^i(x, t) = 0$  in the under-saturated mixture regime represents a fluid surface that separates the pure granular upper layer from the grain-fluid saturated mixture lower layer, illustrated in Figure 2d, whereas in the over-saturated mixture regime, the interface between the pure fluid upper layer and the saturated mixture lower layer is a grain surface, as depicted in Figure 2e. In each surface, the upward pointing unit normal is  $\mathbf{n}^\alpha = \nabla F^\alpha / |\nabla F^\alpha|$ , where  $\alpha = s, f, i, b$ . The corresponding boundary conditions at the free surface, at the layer interface and at the basal surface are specified below for different flow regimes, respectively.

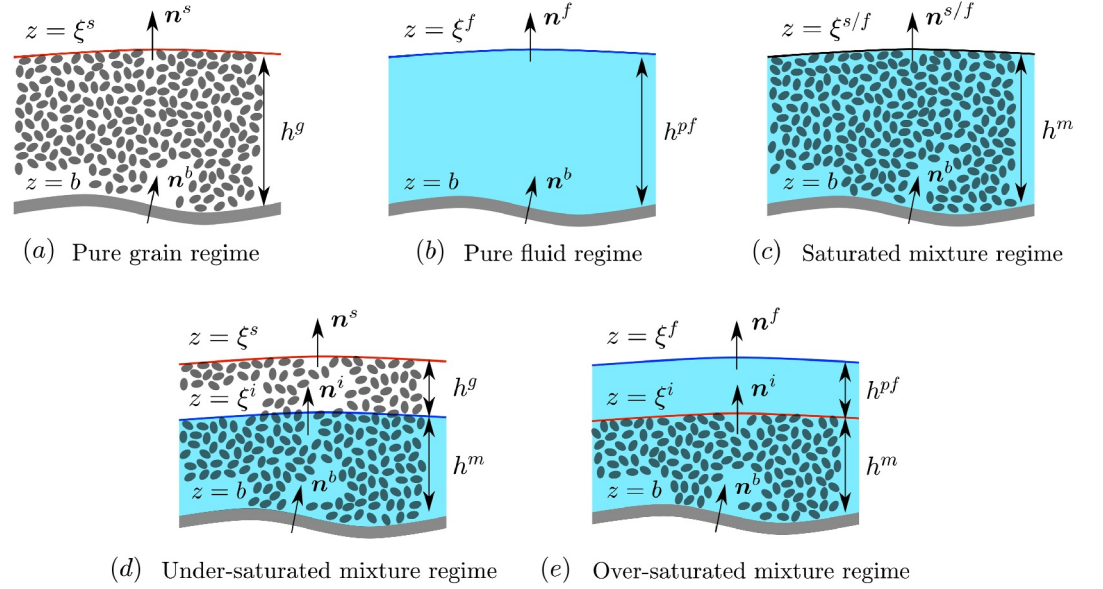


**Figure 2.** Schematic diagram illustrating the vertical structures of various regimes possibly occurring in a grain-fluid mixture flow, including (a) the pure grain regime, (b) the pure fluid regime, (c) the saturated mixture regime, (d) the under-saturated mixture regime, and (e) the over-saturated mixture regime. In panel (c), the free surface at  $z = \xi^{s/f}(x, t)$  represents the common boundary for the solid and fluid phases. In panel (d), the grain free surface at  $z = \xi^s(x, t)$  is positioned above the fluid surface at  $z = \xi^i(x, t)$ , while in the over-saturated mixture regime (e), the situation is reversed (courtesy of Meng et al. (2022)). The flow base is located at  $z = b(x)$ . The heights of the pure grain, pure fluid, and saturated mixture regimes are denoted by  $h^g$ ,  $h^{pf}$ , and  $h^m$ , respectively.

#### 2.4.1. Pure Grain Regime

For the pure grain regime, as shown in Figure 2a, the kinematic boundary conditions at the grain free surface  $F^s(x, z, t) = 0$  and the basal surface  $F^b(x, z) = 0$  are given by

$$\frac{\partial F^s}{\partial t} + \mathbf{u}^s \cdot \nabla F^s = 0, \quad \text{at } F^s(x, z, t) = 0, \quad (19)$$

$$\mathbf{u}^s \cdot \nabla F^b = 0, \quad \text{at } F^b(x, z) = 0. \quad (20)$$

It is assumed that no bed erosion occurs, so that  $F^b$  is time-independent. The traction-free conditions are satisfied at the grain free surface, while at the basal surface, the granular shear stress is assumed to be proportional to the granular normal stress, expressed as

$$\boldsymbol{\sigma}^e \mathbf{n}^s = \mathbf{0}, \quad \text{at } F^s(x, z, t) = 0, \quad (21)$$

$$\boldsymbol{\sigma}^e \mathbf{n}^b - (\mathbf{n}^b \cdot \boldsymbol{\sigma}^e \mathbf{n}^b) \mathbf{n}^b = -\frac{\mathbf{u}_b^s}{|\mathbf{u}_b^s|} \mu^b (\mathbf{n}^b \cdot \boldsymbol{\sigma}^e \mathbf{n}^b), \quad \text{at } F^b(x, z) = 0, \quad (22)$$

where  $\mu^b$  is the basal friction coefficient. For pure grain flows, we employ the commonly used  $\mu(I)$  rheology to model the basal friction coefficient  $\mu^b$  (Bouchut et al., 2021; Forterre & Pouliquen, 2008; Gray & Edwards, 2014; Mangeney et al., 2007; Meng et al., 2022; Pouliquen & Forterre, 2002; Sarno, Tai, et al., 2021), which is based on a single dimensionless parameter known as the inertial number  $I$ , governing the basal friction law. This will be discussed in detail in Section 2.8. These kinematic and dynamic boundary conditions closely align with those described by Savage and Hutter (1989) and Gray et al. (1999) for the classical Savage-Hutter model.

#### 2.4.2. Pure Fluid Regime

For the pure fluid regime, as illustrated in Figure 2b, the kinematic conditions at the pure fluid free surface  $F^f(x, z, t) = 0$  and the basal surface  $F^b(x, z) = 0$  can be given as follows

$$\frac{\partial F^f}{\partial t} + \mathbf{u}^f \cdot \nabla F^f = 0, \quad \text{at } F^f(x, z, t) = 0, \quad (23)$$

$$\mathbf{u}^f \cdot \nabla F^b = 0, \quad \text{at } F^b(x, z) = 0. \quad (24)$$

Traction-free condition holds on the fluid free surface

$$\boldsymbol{\sigma}^f \mathbf{n}^f = \mathbf{0}, \quad \text{at } F^f(x, z, t) = 0. \quad (25)$$

Here, it is assumed that the fluid pressure  $p^{f*}$  at the free surface ceases, that is, a vanishing atmospheric pressure. At the basal surface, we use a Chézy formula (see Chaudhry, 2008) to describe the fluid basal friction, given by

$$\boldsymbol{\sigma}^f \mathbf{n}^b - (\mathbf{n}^b \cdot \boldsymbol{\sigma}^f \mathbf{n}^b) \mathbf{n}^b = \rho^{f*} C^f |\bar{\mathbf{u}}^f| \bar{\mathbf{u}}^f, \quad \text{at } F^b(x, z) = 0 \quad (26)$$

where  $C^f$  is the Chézy drag coefficient and  $\bar{\mathbf{u}}^f$  is the depth-averaged fluid velocity. This basal friction condition (26) for the fluid is identical to that employed in the study by Luca et al. (2012) and Meng et al. (2022). However, in the study conducted by Bouchut et al. (2016), a Navier friction condition for the fluid was applied at the bottom. The fluid friction coefficient  $C^f$  will be formulated in detail in Section 2.8.

#### 2.4.3. Saturated Grain-Fluid Mixture Regime

In the regime of a saturated grain-fluid mixture, as indicated in Figure 2c, the kinematic conditions on the free surface and the basal surface for both the solid and fluid phases are equivalent to those of the pure grain and pure fluid regimes, respectively, as given in Equations 19, 20, 23, and 24. The traction-free conditions at the free surface and the basal friction law expressions at the basal surface for the solid and fluid phases are identical to conditions (21) and (22) of the pure grain regime and (25) and (26) of the pure fluid regime, respectively. It should be noted that in the case of saturated grain-fluid mixture flows, the presence of the fluid phase requires the use of a  $\mu(I_v)$  rheology to model the granular basal friction coefficient  $\mu^b$  emerging in Equation 22, as recommended by Boyer et al. (2011). The detailed formulation of the  $\mu(I_v)$  rheology will be presented in Section 2.8.

#### 2.4.4. Under-Saturated Grain-Fluid Mixture Regime

As shown in Figure 2d, the under-saturated grain-fluid regime is characterized by a pure grain upper layer overlying a saturated mixture lower layer. At the grain free surface, the kinematic and traction-free conditions are the same as those in Equations 19 and 21 in the pure grain regime. On the basal surface, the kinematic and dynamic boundary conditions for the solid and fluid phases are identical to those in the saturated mixture regime. In this flow regime, we adopt the kinematic and dynamic conditions at the interface as proposed by Meng et al. (2017) in the following. The interface  $F^i(x, z, t) = 0$  between layers is a material surface for the fluid phase, satisfying the kinematic condition

$$\frac{\partial F^i}{\partial t} + \mathbf{u}^f \cdot \nabla F^i = 0, \quad \text{at } F^i(x, z, t) = 0. \quad (27)$$

Across this interface, a mass transfer of grains can occur. The granular mass jump condition is given by

$$[[[\boldsymbol{\varphi}^s(\mathbf{u}^s - \mathbf{u}^f)]]] \cdot \mathbf{n}^i = 0, \quad \text{at } F^i(x, z, t) = 0, \quad (28)$$

where the jump brackets  $[[ \ ]]$  denote the difference between the quantity within the brackets on the upper (+) and lower (−) sides of the interface, that is,  $[[\Psi]] = \Psi^+ - \Psi^-$ . Equation 28 represents the mass conservation of

grains across the fluid interface. To simplify the derivation, we introduce the notation  $M^s$  to represent the granular mass transfer (corresponding to the symbol  $J$  in the work of Meng et al. (2017)), which is expressed as follows

$$M^s = \varrho^{s*} \phi^{s+} (\mathbf{u}^{s+} - \mathbf{u}^{f-}) \cdot \mathbf{n}^i = \varrho^{s*} \phi^{s-} (\mathbf{u}^{s-} - \mathbf{u}^{f-}) \cdot \mathbf{n}^i. \quad (29)$$

where  $\phi^{s\pm}$  and  $\mathbf{u}^{s\pm}$  denote the solid volume fraction and grain velocities on the upper and lower sides of the interface, respectively.  $\mathbf{u}^{f-}$  is the velocity of the fluid phase on the lower side of the interface, coinciding with the velocity of the interface.

In addition, at the interface in the under-saturated mixture regime, we assume that the traction-free condition holds for the fluid phase and the momentum balance between the upper layer granular material and the lower layer granular phase holds, as described in the work of Meng et al. (2017). This leads to the momentum conditions at the interface

$$\boldsymbol{\sigma}^f \mathbf{n}^i = \mathbf{0}, \quad \text{at } F^i(x, z, t) = 0, \quad (30)$$

$$[[ -\boldsymbol{\sigma}^s - \varrho^s \mathbf{u}^s (\mathbf{u}^s - \mathbf{u}^f) ]] \cdot \mathbf{n}^i = 0, \quad \text{at } F^i(x, z, t) = 0. \quad (31)$$

Due to the assumption of a vanishing atmospheric pressure, that is, a vanishing fluid pressure at the interface (a free fluid surface),  $p^{f*} = 0$ ,  $\boldsymbol{\sigma}^s$  in Equation 31 can also be replaced by  $\boldsymbol{\sigma}^e$ . Furthermore, similar to the rate-dependent friction condition at the interface presented by Meng et al. (2017) (refer to Equation (19) in their work), we also employ a tangential friction boundary condition for the granular constituent at the lower side of the interface

$$\boldsymbol{\sigma}^e \cdot \mathbf{n}^i - (\mathbf{n}^i \cdot \boldsymbol{\sigma}^e \cdot \mathbf{n}^i) \mathbf{n}^i = \frac{\mathbf{u}_\tau^{s-} - \mathbf{u}_\tau^{s+}}{|\mathbf{u}_\tau^{s-} - \mathbf{u}_\tau^{s+}|} \mu^i (\mathbf{n}^i \cdot \boldsymbol{\sigma}^e \cdot \mathbf{n}^i), \quad \text{at } F^i(x, z) = 0, \quad (32)$$

where  $\mu^i$  is the granular friction coefficient for the pure grains in the upper layer at the interface and will be formulated in detail in Section 2.8.  $\mathbf{u}_\tau^{s\pm} = \mathbf{u}^{s\pm} - (\mathbf{u}^{s\pm} \cdot \mathbf{n}^i) \mathbf{n}^i$  refers to the tangential velocities of the grains on the upper and lower sides of the interface, respectively.

#### 2.4.5. Over-Saturated Grain-Fluid Mixture Regime

The over-saturated grain-fluid mixture regime also consists of a two-layer system with a pure fluid upper layer and a saturated mixture lower layer, as illustrated in Figure 2e. At the free surface of the fluid upper layer, the kinematic and traction-free dynamic conditions are the same as those in the pure fluid regime, as described by Equation 23 and 25. At the basal surface, the kinematic and friction conditions for the solid and fluid phases are identical to those in the saturated mixture regime, as in the under-saturated mixture regime. However, in contrast to the under-saturated mixture regime, the interface  $F^i(x, z, t) = 0$  between the layers in this case is a granular material surface. In the over-saturated grain-fluid mixture regime, we employ the kinematic and dynamic boundary conditions at the interface as presented in the study by Luca et al. (2012). Although many of these conditions share similarities to those proposed in Bouchut et al. (2016), certain differences exist, which will be expounded upon in detail in the subsequent context. The kinematic condition on the interface is given by

$$\frac{\partial F^i}{\partial t} + \mathbf{u}^s \cdot \nabla F^i = 0, \quad \text{at } F^i(x, z, t) = 0. \quad (33)$$

Fluid mass transfer can occur across the granular material interface, and the fluid volume fraction jumps from  $\phi^f = 1 - \phi^s$  to  $\phi^f = 1$ . Similar to the granular mass jump condition (28) in the under-saturated mixture regime, the fluid mass jump condition takes the following form as

$$[[ \varrho^f (\mathbf{u}^f - \mathbf{u}^s) ]] \cdot \mathbf{n}^i = 0, \quad \text{at } F^i(x, z, t) = 0. \quad (34)$$

Additionally, the notation  $M^f$  is introduced to express the fluid mass transfer across the interface (associated with the notation  $M_{\text{int}}$  in Luca et al. (2012),  $\nu_f$  in Bouchut et al. (2016) and  $M$  in Sun et al. (2023)), which is defined as

$$M^f = \varrho^{f*} (\mathbf{u}^{f+} - \mathbf{u}^{s-}) \cdot \mathbf{n}^i = \varrho^{f*} \phi^{f-} (\mathbf{u}^{f-} - \mathbf{u}^{s-}) \cdot \mathbf{n}^i. \quad (35)$$

Here,  $\mathbf{u}^{f\pm}$  represent the fluid velocities on the upper and lower sides of the interface, respectively, while  $\mathbf{u}^{s-}$  denotes the velocity of the granular phase on the lower side of the interface, coinciding with the interface velocity.

Moreover, at the interface in the over-saturated mixture regime, the momentum balance at the interface between the upper layer pure fluid and the lower layer mixture as a whole must be fulfilled, as described in Luca et al. (2012) and Bouchut et al. (2016), by the momentum jump condition

$$[[\boldsymbol{\sigma} - \varrho^f \mathbf{u}^f (\mathbf{u}^f - \mathbf{u}^s)]] \cdot \mathbf{n}^i = 0, \quad \text{at } F^i(x, z, t) = 0, \quad (36)$$

which is a well-established momentum jump condition at the interface with the fluid mass transfer. On the upper side of the interface, we have  $\boldsymbol{\sigma} = \boldsymbol{\sigma}^{f+}$ , while on the lower side, the total mixture stress takes the form  $\boldsymbol{\sigma} = \boldsymbol{\sigma}^{s-} + \boldsymbol{\sigma}^{f-}$ , where  $\boldsymbol{\sigma}^{f+}$  represents the stress of the upper layer pure fluid, and  $\boldsymbol{\sigma}^{s-}$  and  $\boldsymbol{\sigma}^{f-}$  are the stresses of the lower layer granular and fluid constituents, respectively. Utilizing the definition of fluid mass transfer (35), we can explicitly formulate this condition (36) as

$$\boldsymbol{\sigma}^{f+} \mathbf{n}^i - M^f \mathbf{u}^{f+} = \boldsymbol{\sigma}^{f-} \mathbf{n}^i + \boldsymbol{\sigma}^{s-} \mathbf{n}^i - M^f \mathbf{u}^{f-}. \quad (37)$$

This condition represents the balance of the stress forces of both sides at the interface with the momentum transfer by the fluid mass transfer across the interface.

In addition to the condition (37), Luca et al. (2012) assumed the momentum jump condition for the fluid as follows

$$\boldsymbol{\sigma}^{f-} \mathbf{n}^i = \phi^{f-} (\boldsymbol{\sigma}^{f+} \mathbf{n}^i) - M^f (\mathbf{u}^{f+} - \mathbf{u}^{f-}), \quad (38)$$

which represents a balance between the fluid stress force in the lower layer mixture, the fluid stress force of the upper layer in the parts in contact with the fluid of the lower layer and the fluid momentum exchange due to the mass transfer across the interface. Subsequently, substituting (38) into (37) yields a physically plausible condition for the granular stress at the interface

$$\boldsymbol{\sigma}^{s-} \mathbf{n}^i = \phi^{s-} (\boldsymbol{\sigma}^{f+} \mathbf{n}^i), \quad (39)$$

which represents a force balance between the grain stress force in the lower layer mixture and the fluid stress force in the upper layer in the parts that are in contact with the grains of the lower layer.

In contrast, Bouchut et al. (2016) employed a stress transfer condition derived from an energy balance at the interface. This different stress condition leads to different source terms in the depth-averaged momentum equations for the pure fluid upper layer and the fluid phase in the mixture lower layer in both models.

Similar to the friction boundary condition (32) at the interface for the granular phase in the under-saturated mixture regime, a friction condition at the interface for the fluid must also be specified in the over-saturated mixture regime. In our model, the tangential friction acting on the upper pure fluid is assumed to obey the Chézy formula, as described in Luca et al. (2012), given by

$$\boldsymbol{\sigma}^{f+} \mathbf{n}^i - (\mathbf{n}^i \cdot \boldsymbol{\sigma}^{f+} \mathbf{n}^i) \mathbf{n}^i = \varrho^{f*} C^f |\bar{\mathbf{u}}^{f+} - \bar{\mathbf{u}}^{m-}| (\bar{\mathbf{u}}^{f+} - \bar{\mathbf{u}}^{m-}), \quad \text{at } F^i(x, z, t) = 0, \quad (40)$$

with the lower bulk depth-averaged velocity  $\bar{\mathbf{u}}^{m-} = (\varrho^s \bar{\mathbf{u}}^s + \varrho^f \bar{\mathbf{u}}^f) / \varrho^m$  and the bulk density  $\varrho^m = \varrho^{s*} \phi^s + \varrho^{f*} \phi^f$ . This friction condition is simplified to (26), if the saturated mixture lower layer is absent, that is,  $\bar{\mathbf{u}}^{m-} = 0$ . In comparison, Bouchut et al. (2016) used a Navier friction condition for the upper-layer fluid at the interface.

## 2.5. The Depth-Averaged Model Framework

In this section, we present depth-averaged models for the five distinct regimes, as shown in Figure 2. The depth-averaged approach is commonly used to reduce computational burden by solving the full three-dimensional model equations in the study of granular matter and grain-fluid mixture flows. This approach is justified because for most geophysical flows the typical flow thickness  $H$  of grain-fluid mixture flows is generally much smaller than their typical length  $L$ . Moreover, as discussed in Chiou et al. (2005) and Sun et al. (2023), this approach requires a slowly varying basal topography, that is, the characteristic radius of curvature of the basal topography  $R$  is much larger than the typical flow length  $L$ . In the present study, our model does not address complex topography.

By integrating Equations 10 and 11 through the layer of the pure grains, Equations 12 and 13 through the layer of the pure fluid, as well as Equations 1 and 2 through the layer of the grain-fluid saturated mixture, and applying the aforementioned boundary conditions, a set of tractable thickness-averaged equations can be obtained. The system of depth-averaged equations describes the thickness  $h^g$  and depth-averaged tangential velocity  $\bar{u}^g$  of the pure grain region, including the pure grain regime and the granular upper layer in the under-saturated mixture regime, the thickness  $h^{pf}$  and depth-averaged tangential velocity  $\bar{u}^{pf}$  of the pure fluid region, including the pure fluid regime and the fluid upper layer in the over-saturated mixture regime, the thickness  $h^m$  of the saturated mixture of grains and fluid, as well as the depth-averaged tangential velocities  $\bar{u}^s$  and  $\bar{u}^f$  of the solid and fluid phases in the saturated mixture, respectively. As discussed in Section 2.3, since the dilatancy effect in the pure grain region is not significant compared to the saturated mixture region, for simplicity, we assume the pure grain region is a density-preserving medium with a constant solid volume fraction  $\phi^g$ , while the solid volume fraction  $\phi^s$  in the saturated mixture region is a physical variable. In the following depth-averaging it is further assumed that the variation of  $\phi^s$  in the depth direction is negligibly small.

As indicated in Figure 2, the thicknesses  $h^g$ ,  $h^{pf}$ , and  $h^m$  are given by  $h^g = \xi^s - \xi^i$ ,  $h^{pf} = \xi^f - \xi^i$ , and  $h^m = \xi^i - b$ , respectively. The depth-averaged tangential velocities are defined as follows

$$\begin{aligned}\bar{u}^g &= \frac{1}{h^g} \int_{\xi^i}^{\xi^s} u^s(x, z, t) dz, & \bar{u}^{pf} &= \frac{1}{h^{pf}} \int_{\xi^i}^{\xi^f} u^f(x, z, t) dz, \\ \bar{u}^s &= \frac{1}{h^m} \int_b^{\xi^i} u^s(x, z, t) dz, & \bar{u}^f &= \frac{1}{h^m} \int_b^{\xi^i} u^f(x, z, t) dz.\end{aligned}\quad (41)$$

In the following, it is assumed that there is no shallow topography superimposed over the reference coordinate surface, that is,  $b = 0$ .

Using these notations, the depth-averaged mass and momentum balance equations for the five different regimes are formulated. In the following, we begin first by presenting the two-phase two-layer depth-averaged models for the under-saturated and over-saturated mixture regimes. The single-layer depth-averaged models for the pure grain, pure fluid, and saturated mixture regimes are subsequently derived from the two-phase two-layer depth-averaged models. The processes of the depth-averaging for the under-saturated and over-saturated mixture regimes are shown in Appendix A to Appendix D.

### 2.5.1. Two-Layer Depth-Averaged Model for the Under-Saturated Mixture Regime

The model equations for under-saturated mixture regime, derived by integrating conservation equations in the normal direction of the topography, respectively, for both the upper layer of the pure grains and the lower layer of the grain-fluid saturated mixture, together with the corresponding boundary conditions, take the forms for the mass conservation

$$\frac{\partial}{\partial t}(h^g \phi^g) + \frac{\partial}{\partial x}(h^g \phi^g \bar{u}^g) = \frac{M^g}{\rho^{s*}}, \quad (42)$$

$$\frac{\partial}{\partial t}(h^m \phi^s) + \frac{\partial}{\partial x}(h^m \phi^s \bar{u}^s) = -\frac{M^g}{\rho^{s*}}, \quad (43)$$

$$\frac{\partial}{\partial t}(h^m \phi^f) + \frac{\partial}{\partial x}(h^m \phi^f \bar{u}^f) = 0, \quad (44)$$

and for the momentum balance

$$\frac{\partial}{\partial t}(h^g \phi^g \bar{u}^g) + \frac{\partial}{\partial x} \left( \chi^g h^g \phi^g (\bar{u}^g)^2 + \frac{1}{2} (h^g)^2 \phi^g g \cos \zeta \right) = S_u^g, \quad (45)$$

$$\frac{\partial}{\partial t}(h^m \phi^s \bar{u}^s) + \frac{\partial}{\partial x} \left( \chi^s h^m \phi^s (\bar{u}^s)^2 + \frac{1}{2} (h^m)^2 \phi^s g \cos \zeta \right) = S_u^s, \quad (46)$$

$$\frac{\partial}{\partial t}(h^m \phi^f \bar{u}^f) + \frac{\partial}{\partial x} \left( \chi^f h^m \phi^f (\bar{u}^f)^2 + \frac{1}{2} (h^m)^2 \phi^f g \cos \zeta \right) = S_u^f. \quad (47)$$

The momentum balance Equations 45–47 incorporate the shape factor  $\chi^\alpha$ ,  $\alpha = g, s, f$ , which characterizes the ratio of the depth-averaged square of the velocity,  $(\bar{u}^\alpha)^2$ , to the depth-averaged velocity squared,  $(\bar{u}^\alpha)^2$ , for the pure grains and the solid and fluid phases in the saturated mixture, respectively, in the convective terms. Many previous works (see e.g. Bouchut et al., 2016; Meng et al., 2017; Meng & Wang, 2016; Pitman & Le, 2005; Sun et al., 2023), postulated that the shape factor  $\chi^\nu = 1$ , which is also assumed in this paper for the following depth-averaged models for other regimes. The right-hand side terms in mass balance Equations 42 and 43 represent the granular mass transfer across the layer interface. This can be the case, for example, when initially dense packing of grains in a saturated mixture dilutes under shear, some of the grains expands from the mixture into the pure grains upper layer. This results in the formation of an under-saturated mixture regime from the previous saturated mixture regime, leading to a positive granular mass product  $M^s$  in the right-hand side of Equation 42 and a negative product  $-M^s$  in Equation 43.

The source terms on the right-hand side of the momentum balance equations for the under-saturated mixture regime, Equations 45–47, are given by

$$S_u^g = \underbrace{h^g \phi^g g \sin \zeta}_{\text{Gravity}} + \underbrace{\frac{M^s \bar{u}^{s\pm}}{\varrho^{s*}}}_{\text{Momentum transfer}} + \underbrace{\frac{\bar{u}^s - \bar{u}^g}{|\bar{u}^s - \bar{u}^g|} \mu^i (h^g \phi^g g \cos \zeta + \kappa h^g \phi^g (\bar{u}^g)^2)}_{\text{Inter-layer friction}} - \underbrace{h^g \phi^g g \cos \zeta \frac{\partial h^m}{\partial x}}_{\text{Layered interplay}}, \quad (48)$$

$$S_u^s = \underbrace{h^m \phi^s g \sin \zeta}_{\text{Gravity}} - \underbrace{\frac{M^s \bar{u}^{s\pm}}{\varrho^{s*}}}_{\text{Momentum transfer}} + \underbrace{\frac{1}{2} \gamma (h^m)^2 g \cos \zeta \frac{\partial \phi^s}{\partial x}}_{\text{Phased interplay}} + \underbrace{\frac{C^d}{\varrho^{s*}} h^m (\bar{u}^f - \bar{u}^s)}_{\text{Drag force}} - \underbrace{\frac{\bar{u}^s - \bar{u}^g}{|\bar{u}^s - \bar{u}^g|} \mu^i (h^g \phi^g g \cos \zeta + \kappa h^g \phi^g (\bar{u}^g)^2)}_{\text{Inter-layer friction}} - \underbrace{h^m g \frac{\partial}{\partial x} (h^g \phi^g \cos \zeta)}_{\text{Layered interplay}} - \underbrace{\frac{\bar{u}^s}{|\bar{u}^s|} \mu^b \left[ \frac{P_b^p}{\varrho^{s*}} + \kappa h^m \phi^s \left( (\bar{u}^s)^2 - \gamma (\bar{u}^f)^2 \right) + h^g \phi^g g \cos \zeta + \kappa h^g \phi^g (\bar{u}^g)^2 \right]}_{\text{Granular basal friction}}, \quad (49)$$

$$S_u^f = \underbrace{h^m \phi^f g \sin \zeta}_{\text{Gravity}} + \underbrace{\frac{1}{2} (h^m)^2 g \cos \zeta \frac{\partial \phi^f}{\partial x}}_{\text{Phased interplay}} - \underbrace{\frac{C^d}{\varrho^{f*}} h^m (\bar{u}^f - \bar{u}^s)}_{\text{Drag force}} - \underbrace{\frac{C^f |\bar{u}^f| \bar{u}^f}{\varrho^{f*}}}_{\text{Fluid basal friction}}. \quad (50)$$

where  $\zeta$  is the local downslope inclination angle of the basal reference surface and  $\kappa$  denotes the curvature of the basal reference surface and is defined as  $\kappa = -d\zeta/dx$ .  $\mu^i$  in source terms (48) and (49) is the granular friction coefficient for the pure grains in the upper layer at the interface. The parameter  $\gamma$  appearing in the source terms (49), defined as  $\gamma = \rho^{f*}/\rho^{s*}$ , denotes the intrinsic density ratio between the fluid and grains. The terms  $M^s \bar{u}^{\pm}$  in Equations 48 and 49 represent the interfacial momentum transfer caused by the granular mass transfer across the interface. For the transfer of granular mass from the pure grain upper layer to the saturated mixture lower layer, that is,  $M^s < 0$ , the velocity  $\bar{u}^{\pm}$  appearing in these terms takes the grain velocity of the upper layer,  $\bar{u}^{\pm} = \bar{u}^g$ . Conversely, for  $M^s > 0$ , the velocity  $\bar{u}^{\pm}$  will take the velocity of the granular phase in the lower layer,  $\bar{u}^{\pm} = \bar{u}^s$ . The source terms in the depth-averaged mass and momentum balance equations require the expressions of the granular mass transfer  $M^s$ , the particle basal pressure  $p_b^p$ , and the friction coefficients  $\mu^i$  and  $\mu^b$ , as well as the Chézy drag coefficient  $C^f$ , which are presented later in Sections 2.6–2.8.

Furthermore, Section 2.9 provides a detailed comparison between the present model in our study and the model proposed by Meng et al. (2017) for the under-saturated mixture flows.

### 2.5.2. Two-Layer Depth-Averaged Model for the Over-Saturated Mixture Regime

Similarly, the model equations for the over-saturated mixture regime, consisting of the layers of the pure fluid and the saturated mixture of grains and fluid, are obtained by integrating conservation equations in the normal direction of the topography and employing the corresponding boundary conditions, respectively, for both the layers. The depth-averaged balance equations for mass are

$$\frac{\partial h^{pf}}{\partial t} + \frac{\partial}{\partial x}(h^{pf} \bar{u}^{pf}) = \frac{M^f}{\rho^{f*}}, \quad (51)$$

$$\frac{\partial}{\partial t}(h^m \phi^f) + \frac{\partial}{\partial x}(h^m \phi^f \bar{u}^f) = -\frac{M^f}{\rho^{f*}}, \quad (52)$$

$$\frac{\partial}{\partial t}(h^m \phi^s) + \frac{\partial}{\partial x}(h^m \phi^s \bar{u}^s) = 0, \quad (53)$$

and for momenta

$$\frac{\partial}{\partial t}(h^{pf} \bar{u}^{pf}) + \frac{\partial}{\partial x} \left( h^{pf} (\bar{u}^{pf})^2 + \frac{1}{2} (h^{pf})^2 g \cos \zeta \right) = S_o^{pf}, \quad (54)$$

$$\frac{\partial}{\partial t}(h^m \phi^f \bar{u}^f) + \frac{\partial}{\partial x} \left( h^m \phi^f (\bar{u}^f)^2 + \frac{1}{2} (h^m)^2 \phi^f g \cos \zeta \right) = S_o^f, \quad (55)$$

$$\frac{\partial}{\partial t}(h^m \phi^s \bar{u}^s) + \frac{\partial}{\partial x} \left( h^m \phi^s (\bar{u}^s)^2 + \frac{1}{2} (h^m)^2 \phi^s g \cos \zeta \right) = S_o^s. \quad (56)$$

Equation 51 describes the mass balance for the pure fluid upper layer, where  $M^f$  represents the fluid mass transfer across the layer interface. For an initially loosely packed saturated mixture compacts under shear, an amount of interstitial fluid is expelled from the voids between particles into the pure fluid upper layer. This leads to a positive fluid mass product  $M^f > 0$ , as described in Bouchut et al. (2016) and Sun et al. (2023).

The source terms on the right-hand side of the momentum balance equations for the over-saturated mixture regime, (54), (55), and (56), are given by

$$S_o^{pf} = \underbrace{h^{pf} g \sin \zeta}_{\text{Gravity}} + \underbrace{\frac{M^f \bar{u}^{f\pm}}{\rho^{f*}}}_{\text{Momentum transfer}} - \underbrace{C^f |\bar{u}^{pf} - \bar{u}^m| (\bar{u}^{pf} - \bar{u}^m)}_{\text{Inter-layer friction}} - \underbrace{h^{pf} g \cos \zeta \frac{\partial h^m}{\partial x}}_{\text{Layered interplay}}, \quad (57)$$

$$S_o^f = \underbrace{h^m \phi^f g \sin \zeta}_{\text{Gravity}} - \underbrace{\frac{M^f \bar{u}^{f\pm}}{\varrho^{f\star}}}_{\text{Momentum transfer}} + \underbrace{\phi^f C^f |\bar{u}^{pf} - \bar{u}^m| (\bar{u}^{pf} - \bar{u}^m)}_{\text{Inter-layer friction}} - \underbrace{h^m \phi^f g \frac{\partial(h^{pf} \cos \zeta)}{\partial x}}_{\text{Layered interplay}} - \underbrace{\frac{C^d}{\varrho^{f\star}} h^m (\bar{u}^f - \bar{u}^s)}_{\text{Drag force}} + \underbrace{\frac{1}{2} (h^m)^2 g \cos \zeta \frac{\partial \phi^f}{\partial x}}_{\text{Phased interplay}} - \underbrace{C^f |\bar{u}^f| \bar{u}^f}_{\text{Fluid basal friction}}, \quad (58)$$

$$S_o^s = \underbrace{h^m \phi^s g \sin \zeta}_{\text{Gravity}} + \underbrace{\gamma \phi^s C^f |\bar{u}^{pf} - \bar{u}^m| (\bar{u}^{pf} - \bar{u}^m)}_{\text{Inter-layer friction}} - \underbrace{\gamma h^m \phi^s g \frac{\partial(h^{pf} \cos \zeta)}{\partial x}}_{\text{Layered interplay}} + \underbrace{\frac{C^d}{\varrho^{s\star}} h^m (\bar{u}^f - \bar{u}^s)}_{\text{Drag force}} + \underbrace{\frac{1}{2} \gamma (h^m)^2 g \cos \zeta \frac{\partial \phi^s}{\partial x}}_{\text{Phased interplay}} - \underbrace{\frac{\bar{u}^s}{|\bar{u}^s|} \mu^b \left[ \frac{P_b^p}{\varrho^{s\star}} + \kappa h^m \phi^s ((\bar{u}^s)^2 - \gamma (\bar{u}^f)^2) \right]}_{\text{Granular basal friction}}. \quad (59)$$

The terms  $M^f \bar{u}^{f\pm}$  in Equation 57 and 58 represent the interfacial momentum transfer caused by the fluid mass transfer across the interface. Similarly to the under-saturated regime, for  $M^f < 0$ , the fluid velocity  $\bar{u}^{f\pm}$  will take the value of the upper layer pure fluid velocity  $\bar{u}^{pf}$ ,  $\bar{u}^{f\pm} = \bar{u}^{pf}$ , whereas for  $M^f > 0$ ,  $\bar{u}^{f\pm} = \bar{u}^f$ .

There are also some previous studies that have explored the over-saturated mixture flows using the two-layer depth-averaged model, such as the studies of Luca et al. (2012), Bouchut et al. (2016, 2017) and Sun et al. (2023). The similarities and differences between our model and the others are discussed in Section 2.9.

### 2.5.3. Single-Layer Depth-Averaged Model for the Saturated Mixture Regime

The depth-averaged mass and momentum balance equations for the single-layer saturated mixture regime can be obtained by simplifying the depth-averaged model of either the under-saturated or the over-saturated mixture regime. For instance, for the depth-averaged model of the under-saturated mixture regime, in the absence of the pure grain upper layer, Equations 42 and 45 vanish, and there is no granular mass transfer in Equation 43. The reduced depth-averaged mass and momentum balance equations for the saturated mixture regime are

$$\frac{\partial}{\partial t} (h^m \phi^s) + \frac{\partial}{\partial x} (h^m \phi^s \bar{u}^s) = 0, \quad (60)$$

$$\frac{\partial}{\partial t} (h^m \phi^f) + \frac{\partial}{\partial x} (h^m \phi^f \bar{u}^f) = 0, \quad (61)$$

$$\frac{\partial}{\partial t} (h^m \phi^s \bar{u}^s) + \frac{\partial}{\partial x} \left( h^m \phi^s (\bar{u}^s)^2 + \frac{1}{2} (h^m)^2 \phi^s g \cos \zeta \right) = S^s, \quad (62)$$

$$\frac{\partial}{\partial t} (h^m \phi^f \bar{u}^f) + \frac{\partial}{\partial x} \left( h^m \phi^f (\bar{u}^f)^2 + \frac{1}{2} (h^m)^2 \phi^f g \cos \zeta \right) = S^f. \quad (63)$$

In case the upper granular layer vanishes, the coupling terms between the upper and the lower layer appearing in Equation 49, caused by the momentum transfer due to the mass transfer, the inter-layer friction and the layered interplay vanish. Then, the right-hand side source terms of the momentum balance Equations 49 and 50 are simplified as follows

$$S^s = \underbrace{h^m \phi^s g \sin \zeta}_{\text{Gravity}} + \underbrace{\frac{1}{2} \gamma (h^m)^2 g \cos \zeta \frac{\partial \phi^s}{\partial x}}_{\text{Phased interplay}} + \underbrace{\frac{C^d}{\varrho^{s\star}} h^m (\bar{u}^f - \bar{u}^s)}_{\text{Drag force}} - \underbrace{\frac{\bar{u}^s}{|\bar{u}^s|} \mu^b \left[ \frac{P_b^p}{\varrho^{s\star}} + \kappa h^m \phi^s ((\bar{u}^s)^2 - \gamma (\bar{u}^f)^2) \right]}_{\text{Granular basal friction}}, \quad (64)$$

$$S^f = \underbrace{h^m \phi^f g \sin \zeta}_{\text{Gravity}} + \underbrace{\frac{1}{2}(h^m)^2 g \cos \zeta \frac{\partial \phi^f}{\partial x}}_{\text{Phased interplay}} - \underbrace{\frac{C^d}{\rho^{f*}} h^m (\bar{u}^f - \bar{u}^s)}_{\text{Drag force}} - \underbrace{C^f |\bar{u}^f| \bar{u}^f}_{\text{Fluid basal friction}}. \quad (65)$$

#### 2.5.4. Single-Layer Depth-Averaged Model for the Pure Grain Regime

The depth-averaged model for the pure grain regime can be obtained by simplifying the depth-averaged model of the under-saturated mixture regime. As the lower layer saturated mixture is absent, only the balance equations of the pure grain upper layer, (42) and (45), in the under-saturated mixture regime remain. The granular mass and momentum transfer terms and coupling terms between the upper and lower layers emerging in the source term (48) vanish. This yields the following depth-averaged mass and momentum balance equations

$$\frac{\partial(h^s \phi^s)}{\partial t} + \frac{\partial}{\partial x}(h^s \phi^s \bar{u}^s) = 0, \quad (66)$$

$$\frac{\partial}{\partial t}(h^s \phi^s \bar{u}^s) + \frac{\partial}{\partial x} \left( h^s \phi^s (\bar{u}^s)^2 + \frac{1}{2}(h^s)^2 \phi^s g \cos \zeta \right) = S^s \quad (67)$$

with the source term

$$S^s = \underbrace{h^s \phi^s g \sin \zeta}_{\text{Gravity}} - \underbrace{\frac{\bar{u}^s}{|\bar{u}^s|} \mu^b h^s \phi^s (g \cos \zeta + \kappa (\bar{u}^s)^2)}_{\text{Granular basal friction}}. \quad (68)$$

It is noted that the interfacial granular friction in the source term (48) is reduced to the granular basal friction in Equation 68 and the interfacial friction coefficient  $\mu^i$  is replaced by the basal friction coefficient  $\mu^b$ . These depth-averaged equations are consistent with the Savage-Hutter model (see Savage & Hutter, 1989; Wang et al., 2004), if the volume fraction  $\phi^s$  is assumed to be constant, that is,  $\phi^s = \text{const}$ . In the present study, we employ the Savage-Hutter model for the regions of pure grains, that is, for the pure grain regime and for the pure granular upper layer of the under-saturated mixture regime.

#### 2.5.5. Single-Layer Depth-Averaged Model for the Pure Fluid Regime

Similarly, the depth-averaged model of the pure fluid regime can be obtained from the depth-averaged balance equations of the pure fluid upper layer in the over-saturated mixture regime in the absence of the lower layer mixture. In this case, the fluid mass and momentum transfer terms and coupling terms between layers vanish, and the interfacial fluid friction in the source term (57) is reduced to the fluid basal friction. The depth-averaged mass and momentum balance equations for the pure fluid regime are given by

$$\frac{\partial h^{pf}}{\partial t} + \frac{\partial}{\partial x}(h^{pf} \bar{u}^{pf}) = 0, \quad (69)$$

$$\frac{\partial}{\partial t}(h^{pf} \bar{u}^{pf}) + \frac{\partial}{\partial x} \left( h^{pf} (\bar{u}^{pf})^2 + \frac{1}{2}(h^{pf})^2 g \cos \zeta \right) = S^{pf} \quad (70)$$

with the source term

$$S^{pf} = \underbrace{h^{pf} g \sin \zeta}_{\text{Gravity}} - \underbrace{C^f |\bar{u}^{pf}| \bar{u}^{pf}}_{\text{Fluid basal friction}}. \quad (71)$$

These depth-averaged equations correspond to the shallow water equations (see Audusse et al., 2004; Bollermann et al., 2013; De Saint-Venant, 1871; Jin, 2001; Kurganov & Levy, 2002; Kurganov & Petrova, 2007) and are consistent with the model presented in Chertock et al. (2015), which also considered a Chézy-like fluid basal friction. In this study, the model of Chertock et al. (2015) is used for the pure fluid regions, that is, for the pure fluid regime and for the pure fluid upper layer of the over-saturated mixture regime.

## 2.6. Granular and Fluid Mass Transfer Across the Layer Interface

The phase separation is an important characteristic of grain-fluid mixture flows. As previously mentioned, when particles in a fluid-saturated mixture undergo dilation under shear, such as in the case of initial dense packing, the voids between the particles increase, and some of the particles are extruded and separate from the saturated mixture. This results in the formation of a pure particle upper layer and a transition from an initially saturated mixture flow to an under-saturated mixture flow. Conversely, when the particles in the saturated mixture compact under shear, such as in the case of initial loose packing, the voids between the particles decrease, causing the fluid between the particles to be extruded and forming a pure fluid upper layer. This leads to a transition from an initially saturated mixture flow to an over-saturated mixture flow.

To formulate the granular mass transfer  $M^s$  in the under-saturated mixture regime, we first depth-integrate Equation 15 from the base to the mixture surface. Then, we apply the definition of the mass jump condition (Equation 29) to obtain

$$\frac{\partial h^m}{\partial t} + \frac{\partial(h^m \bar{u}^s)}{\partial x} = -\frac{M^s}{\varrho^{s*} \phi^s} + h^m (\dot{\gamma}^s)^b \tan \psi^b. \quad (72)$$

where  $\psi^b$  is the basal dilatancy angle of grains and  $(\dot{\gamma}^s)^b$  is the solid basal shear rate. Assuming that the flows exhibit a parabolic velocity profile (see e.g. Bouchut et al., 2016; Boyer et al., 2011; Cassar et al., 2005; Pailha & Pouliquen, 2009; Sun et al., 2023), the solid basal shear rate can be expressed as  $(\dot{\gamma}^s)^b = 3|\bar{u}^s|/h^m$ , this formulation of the solid basal shear rate will be discussed in the following. Moreover, substituting this into (17) and (18) results in the basal dilatancy

$$\tan \psi^b = K_3 \left( \phi^s - \phi^c + 3K_2 \frac{\eta^f}{p_b} \frac{|\bar{u}^s|}{h^m} \right). \quad (73)$$

Then, adding Equations 43 and 44 yields

$$\frac{\partial h^m}{\partial t} + \frac{\partial}{\partial x} (h^m \phi^s \bar{u}^s + h^m \phi^f \bar{u}^f) = -\frac{M^s}{\varrho^{s*}}. \quad (74)$$

Finally, combining Equation 74 with 72 gives

$$M^s = \frac{\varrho^{s*} \phi^s}{1 - \phi^s} \left( h^m (\dot{\gamma}^s)^b \tan \psi^b - \frac{\partial}{\partial x} (h^m \phi^f (\bar{u}^s - \bar{u}^f)) \right). \quad (75)$$

Similarly, to model the fluid mass transfer  $M^f$  across the layer interface in the over-saturated mixture regime, we depth-integrate also Equation 15 from the base to the mixture surface, and then use the kinematic condition of the granular phase in the over-saturated mixture regime given in Equation 33 to obtain

$$\frac{\partial h^m}{\partial t} + \frac{\partial(h^m \bar{u}^s)}{\partial x} = h^m (\dot{\gamma}^s)^b \tan \psi^b. \quad (76)$$

Then, adding Equations 52 and 53 results in

$$\frac{\partial h^m}{\partial t} + \frac{\partial}{\partial x} (h^m \phi^s \bar{u}^s + h^m \phi^f \bar{u}^f) = -\frac{M^f}{\varrho^{f*}}, \quad (77)$$

and, finally, combining it with Equation 76 yields

$$M^f = -\varrho^{f*} \left( h^m (\dot{\gamma}^s)^b \tan \psi^b - \frac{\partial}{\partial x} (h^m \phi^f (\bar{u}^s - \bar{u}^f)) \right). \quad (78)$$

This formulation is also presented by Bouchut et al. (2016). Equations 75 and 78 reveal that the mass transfer of grains or fluid across the layer interface depends not only on the dilatancy effect of the particles in the saturated mixture but also on the relative tangential motion between the granular and fluid phases in the lower layer mixture.

### 2.7. Particle Basal Pressure

In the classical shallow flow approximation, it is typically assumed that the vertical velocity is small, which results in the fluid pressure being hydrostatic and the particle basal pressure taking the form

$$p_b^p = (\varrho^{s*} - \varrho^{f*}) h^m \phi^s g \cos \zeta, \quad (79)$$

as described in Iverson and Denlinger (2001), Fernández-Nieto et al. (2008), Meng and Wang (2016), and Meng et al. (2017). In this study, we take into account the vertical displacement of particles in the mixture, induced by dilatation or compaction of particles. This relative motion between the grains and fluid results in an excess pore fluid pressure (see Equation B13 in Appendix B), which needs to be included in the particle basal pressure (see Equation B14 in Appendix B) (Bouchut et al., 2016; Iverson & George, 2014; Meng & Wang, 2018; Pailha & Pouliquen, 2009; Sun et al., 2023). The excess pore fluid pressure is formulated according to Pailha and Pouliquen (2009), leading to an additional term for the particle basal pressure as

$$p_b^p = (\varrho^{s*} - \varrho^{f*}) h^m \phi^s g \cos \zeta + K_4 \frac{150 \eta^f (\phi^s)^2}{(1 - \phi^s)^3 d^2} h^m \bar{u}^s \tan \psi^b, \quad (80)$$

where  $K_4$  is a constant and its value will be discussed in Section 4.1.

### 2.8. Friction Coefficients

There are numerous rheological models simulating the frictional behavior of granular type flows. The Coulomb type rheology is the most widely used rheological model (see Askari & Kamrin, 2016; Coulomb, 1773; Iverson, 1997; Meng & Wang, 2016, 2017, 2018; Pitman & Le, 2005; Pelanti et al., 2008, 2011; Pailha & Pouliquen, 2009; Savage & Hutter, 1989; Sun et al., 2023; Wang et al., 2004). In this rheology, the friction coefficient remains constant and is determined by the friction angle of the particles. However, recent studies have demonstrated that the friction coefficient can be a dynamic rheological parameter, indicating the need for a more comprehensive constitutive law. To address this issue, a rheology known as a  $\mu(I)$ -rheology was proposed, which is typically appropriate for simulating thin granular flows (see Forterre & Pouliquen, 2008; Gray & Edwards, 2014; Jop et al., 2005; Mangeney et al., 2007; Pouliquen & Forterre, 2002). The  $\mu(I)$  rheology is a non-linear friction law that considers the dependence of the friction coefficient  $\mu$  on a single dimensionless parameter  $I$ , referred to as the inertial number, and is defined mathematically as  $I = \dot{\gamma}^s d / \sqrt{p^p / \varrho^{s*}}$  (Forterre & Pouliquen, 2008), where  $\dot{\gamma}^s$  signifies the shear rate for pure grains. Some prior studies (Bouchut et al., 2021; Cassar et al., 2005; Gray & Edwards, 2014) have shown that for a dry granular flow down a slope, a Bagnold-like velocity profile is assumed, given as  $u^g(z) = \frac{2I}{3d} \sqrt{\phi^s g \cos \theta} \left[ (h^g)^{\frac{3}{2}} - (h^g - z)^{\frac{3}{2}} \right]$ . From this expression, they computed the depth-averaged velocity of the pure grains as  $\bar{u}^g = \frac{1}{h^g} \int_0^{h^g} u^g(z) dz$  and derived the formulation of the basal granular shear rate of the pure grains in terms of the depth-averaged velocity as

$$\left( \dot{\gamma}^g \right)^b = \frac{5 \bar{u}^g}{2 h^g}. \quad (81)$$

The  $\mu(I)$  rheology has been proved to be appropriate for dry granular flows in the intermediate range of  $I$  (Gray & Edwards, 2014). This friction law made it possible to reproduce very well granular collapse experiments with non-depth-averaged approach (Ionescu et al., 2015; Lagrée et al., 2011; N. Martin et al., 2017) and depth-averaged approach (Bouchut et al., 2021, 2022) and also reproduce channeling flows with levees formation contrary to a constant friction coefficient (Mangeney et al., 2007).

In this paper, we apply a general expression of the  $\mu(I)$  rheology proposed by Jop et al. (2005) and Gray and Edwards (2014) for the basal friction of a pure granular medium as a function of the inertial number

$$\mu^b(I) = \mu_1^g + \frac{\mu_2^g - \mu_1^g}{I_0^g/I + 1}, \quad (82)$$

where the friction coefficients  $\mu_1^g = \tan \zeta_1$  and  $\mu_2^g = \tan \zeta_2$ . These two critical inclination angles,  $\zeta_1$  and  $\zeta_2$ , are determined from measurements of steady-uniform flows. For slope angles below  $\zeta_1$  there is no flow, and for angle above  $\zeta_2$  the flows accelerate. In the case of a static granular material, corresponding to the inertial number  $I \rightarrow 0$ , this expression is simplified to  $\mu^b(I) \rightarrow \mu_1^g$ , where  $\mu_1^g$  stands for the static friction coefficient, which generally corresponds to the Coulomb friction coefficient of the granular material. The constant  $I_0^g$  is defined as follows

$$I_0^g = \frac{5\beta d}{2\sqrt{\phi^g \mathcal{L}}}, \quad (83)$$

where the parameter  $\beta$  is an empirical constant and  $\mathcal{L}$  has the dimensions of a length and is dependent on the properties of the grains and on the bed roughness (Gray & Edwards, 2014). In the following numerical simulations, we adopt the values of these parameters as identical to those in Gray and Edwards (2014), that is,  $\beta = 0.136$  and  $\mathcal{L} = 0.825 \times 10^{-3}$  m. It should be noted that the  $\mu(I)$  rheology for the dry granular flows has been extensively studied in recent works (see e.g. Delannay et al., 2017; Martin et al., 2023; Meng et al., 2024). The following numerical simulations for the dry grains are remade to test the classical depth-averaged model.

For the upper layer of pure grains in the under-saturated mixture regime, the granular friction coefficient  $\mu^i$  at the interface, as presented in the source terms (48) and (49), can also be determined using Equation 82. Considering the non-zero velocity of the lower layer, we assume that the shear rate for the upper layer of pure grains at the interface takes the form

$$\left(\dot{\gamma}^g\right)^i = \frac{5}{2} \frac{|\bar{u}^g - \bar{u}^s|}{h^g}. \quad (84)$$

when the grain-fluid saturated lower layer comes to rest or vanishes, that is,  $\bar{u}^s = 0$ , this expression can degenerate to (81), which corresponds to the basal granular shear rate for the single-layer pure grains.

The dynamic of grain-fluid mixture flows is significantly influenced by the interstitial fluid. Consequently, the constitutive friction law for a fluid-saturated granular material is not dependent on the inertial number  $I$  but rather on a so-called viscous number  $I_v$ . This parameter is defined as  $I_v = \eta^f \dot{\gamma}^s / p^p$ , where  $\dot{\gamma}^s$  represents the shear rate of grains in the saturated mixture. In the study by Cassar et al. (2005), particularly in a viscous regime such as a submarine granular flow sliding down a slope, the velocity profile is assumed to be a half parabola, given by  $u^s(z) = \frac{L_v}{\eta^f} (\rho^{s*} - \rho^{f*}) \phi^s g \cos \theta (h^m - \frac{z}{2}) z$ , resulting in the basal shear rate of grains in the mixture in terms of the depth-averaged velocity as

$$\left(\dot{\gamma}^s\right)^b = \frac{3\bar{u}^s}{h^m}. \quad (85)$$

Then, to describe the friction of the saturated grain-fluid mixture, we utilize the  $\mu(I_v)$  rheology proposed by Boyer et al. (2011). The basal friction of grains in the saturated mixture is a function of the viscous number  $I_v$  and is expressed as follows

$$\mu^b(I_v) = \mu_1^s + \frac{\mu_2^s - \mu_1^s}{I_0^s/I_v + 1} + I_v + \frac{5}{2} \phi^c \sqrt{I_v}. \quad (86)$$

The parameters  $\mu_1^s$ ,  $\mu_2^s$ ,  $I_0^s$  and the critical solid volume fraction  $\phi^c$  can be determined experimentally. Boyer et al. (2011) determined in their experiments  $\mu_1^s = 0.32$ ,  $\mu_2^s = 0.7$ ,  $I_0^s = 0.005$  and  $\phi^c = 0.585$ .

The Chézy drag coefficient  $C^f$  can be modeled in different ways, as demonstrated in previous works such as Kellerhals (1967) and Gerbeau and Perthame (2001). In the present study, we adopt the classical Manning formulation (see Chaudhry, 2008; Chertock et al., 2015; Meng et al., 2022) for the fluid phase in the grain-fluid saturated mixture, given by

$$C^f = \phi^f \frac{gn^2}{(h^m)^{5/3}}, \quad (87)$$

where  $n$  is Manning coefficient. For the pure fluid region, the fluid volume fraction is  $\phi^f = 1$ , and the height of the mixture  $h^m$  is replaced by the height of the pure fluid  $h^{pf}$  in Equation 87. In the computations conducted by Chertock et al. (2015), the Manning coefficient  $n$  ranged from 0.01 to 0.1. In our simulations, we utilize a larger value of this coefficient for the fluid with higher viscosity and a smaller value for the fluid with lower viscosity.

## 2.9. Comparison With Other Depth-Averaged Models

In this subsection, we aim to explain the similarities and differences between our present model and several, at best relevant, previous models in the literature. Since our model includes the models for different flow regimes, we mainly compare these models for the under-saturated and over-saturated grain-fluid mixture flows. In particular, we compare our models with those proposed by Meng et al. (2017), Luca et al. (2012), Bouchut et al. (2016), Sun et al. (2023), and Meng et al. (2022).

### 2.9.1. Depth-Averaged Models for Under-Saturated Grain-Fluid Mixture Flows

For the regime of under-saturated grain-fluid mixture flows, our modeling is most comparable to the model of Meng et al. (2017). We use the same boundary conditions at the flow bed and at the free surface as well as the jump conditions at the interface between the upper layer of pure grains and the lower layer of the saturated mixture as in Meng et al. (2017). In addition, both models have a two-layer two-phase structure, where the solid volume fraction of the pure grains in the upper layer is assumed to be constant, while the solid and fluid volume fraction in the lower layer of the saturated mixture varies. Both models take into account the granular mass and momentum transfer between the layers.

The differences between the two models include, first, the inclusion of granular dilatancy effects and excess pore fluid pressure in the lower layer of the saturated mixture in our model. This allows our model to capture the effects of the initial solid volume fraction on the dynamics of the saturated mixture, such as the significantly different flow behaviors in initially densely or loosely packed granular-fluid mixtures. Second, the granular mass transfer across the interface between the layers in our model depends on the granular dilatancy effect in the lower layer of the mixture, which is different from the modeling of granular mass transfer in Meng et al. (2017). Third, we use the  $\mu(I)$  rheology to characterize the granular friction coefficient of the pure grains in the upper layer and the  $\mu(I_v)$  rheology for the granular friction coefficient of the granular phase in the lower layer of the saturated mixture, while in Meng et al. (2017) the Coulomb friction law was used for both the pure grains and the granular phase in the mixture.

### 2.9.2. Depth-Averaged Models for Over-Saturated Grain-Fluid Mixture Flows

For over-saturated grain-fluid mixture flows, the model proposed by Bouchut et al. (2016) is probably the most relevant to our modeling. We use the boundary conditions introduced by Luca et al. (2012). Our model also incorporates a two-layer two-phase structure, similar to Luca et al. (2012) and Bouchut et al. (2016). It is noteworthy that although Sun et al. (2023) also used a two-layer structure, it treated the lower layer of the saturated mixture as a cohesive bulk, implying identical downward velocities for the solid and fluid phases in the lower layer of the saturated mixture. In addition, our model and the models of Luca et al. (2012), Bouchut et al. (2016), and Sun et al. (2023) take into account the mass and momentum transfer at the interface between the upper layer of pure fluid and the lower layer of saturated mixture. The formulation for the fluid mass transfer across the interface in our model corresponds exactly to that of Bouchut et al. (2016).

However, the model of Luca et al. (2012) did not take into account the granular dilatancy effects and the excess pore fluid pressure in the lower layer of the saturated mixture. In addition, their model lacked the modeling of

fluid mass transfer across the layer interface. Compared to the model proposed by Bouchut et al. (2016), our model includes two major improvements. First, our model considers the shear stress of the pure fluid upper layer interacting at the interface with both the fluid and granular phases in the lower layer mixture according to their volume fractions by using the boundary conditions Equations 38–40. In contrast, Bouchut et al. (2016) applied a Navier fluid friction condition at the interface only between the pure fluid in the upper layer and the fluid phase in the lower layer mixture (see condition (2.40) in their work). A shear stress transition from the pure fluid in the upper layer to the granular phase in the lower layer mixture was neglected, although they are in direct contact at the interface. Second, while Bouchut et al. (2016), Luca et al. (2012), and Sun et al. (2023) all used the Coulomb friction law for the granular phase, we use a more general  $\mu(I_v)$  rheology to characterize the granular friction coefficient for the granular phase in the saturated mixture.

### 2.9.3. Single-Layer Depth-Averaged Model of Meng et al. (2022)

Meng et al. (2022) proposed a two-phase but single-layer depth-averaged model to describe grain-fluid mixture flows, which includes different flow regimes but does not consider granular dilatancy effects. This model is possibly the only other model capable of investigating all flow regimes simultaneously. Their model reproduced the experiments of Davies (1990) well. Since their model adopts a single-layer structure, their depth-averaged equations appear much simpler compared to our two-layer depth-averaged model. In the following, we will explain the reasons for the more complex two-layer depth-averaged model in our study and highlight some key differences with their model.

Our model adopts a two-layer structure in the under- and over-saturated grain-fluid flow regimes, hence allows us to separately describe the different flow behaviors of a single medium, grains or fluid, in the upper layer and a saturated grain-fluid mixture in the lower layer. For instance, in the case of an under-saturated grain-fluid mixture flow regime, the pure grains in the upper layer exhibit different flow characteristics than the grains in the mixture lower layer. On the one hand, the interaction between the granular and fluid phases in the lower layer of the saturated mixture involves factors such as buoyancy force, drag force, and the effect of excess pore fluid pressure generated by the granular dilatancy effect of the fluid phase on the granular phase, while in contrast, no such interactions occur in the upper layer of pure grains. Due to these different effects, it is expected that the grains in the upper layer of pure grains and in the lower layer of the saturated grain-fluid mixture will behave differently, so that separate treatment of the grains in both layers by means of a two-layer approach is necessary. On the other hand, according to the studies by Pouliquen and Forterre (2002), and Boyer et al. (2011), pure grains and grains in a grain-fluid mixture exhibit different frictional behaviors and need to be described by different rheological models. In our model, we use the  $\mu(I)$  rheology to describe the friction of pure grains and the  $\mu(I_v)$  rheology to describe the friction of grains in a grain-fluid mixture.

The situation is similar for an over-saturated grain-fluid mixture flow, in which the fluid in the upper layer of the pure fluid and the fluid phase in the lower layer of the mixture also behave differently. Therefore, it makes sense to use a two-layer model to describe the different flow behaviors of the fluid in both layers. This leads to a much more complex model than that of Meng et al. (2022), who introduced depth averaging over the entire depth of each phase, that is, a single-layer model for such under-saturated or over-saturated mixture regimes, which does not distinguish between the different flow behaviors of the grains or fluid in the upper and lower layers and thus provides a much simpler model.

Furthermore, Meng et al. (2022) assumed a constant solid volume fraction in the entire granular phase. However, the solid volume fraction is not constant during the flow, especially when an initial particle packing strongly deviates from a critical state, and the granular dilatancy effects play a crucial role in the dynamic behavior of mixture flows (Bouchut et al., 2016; Iverson & George, 2014; Sun et al., 2023). In our study, we account for the variability of the solid volume fraction and incorporate the dilatancy effects of the grains in the saturated mixture region.

However, the model of Meng et al. (2022) is the first one that is able to capture different flow regimes and is quite simple, which is beneficial for understanding flow dynamics. In order to describe such different flow regimes with different physical behaviors more accurately, a comprehensive, naturally complex model is required. Our model serves as an improvement to address the aforementioned shortcomings.

### 3. Numerical Method

In this study, a high-resolution central-upwind scheme with a total variation diminishing (TVD) slope limiter is employed to numerically solve the proposed depth-averaged model systems for the five distinct regimes. This scheme has been shown to effectively prevent spurious numerical oscillations and has been successfully used to solve similar systems of equations in various fields, including dry granular flows (see Baker et al., 2016; Chiou et al., 2005; Edwards & Gray, 2015; Meng et al., 2018; Wang et al., 2004), debris flows (see Heß & Wang, 2019; Heß et al., 2019; Meng et al., 2017, 2024; Y. Tai et al., 2019), and submarine avalanches (see Kurganov & Miller, 2014; Sun et al., 2023).

#### 3.1. Numerical Assessment for Different Flow Regimes

In our numerical calculations, we need to simultaneously investigate all five possibly occurring flow regimes with the corresponding different sets of depth-averaged equations in the whole computational domain. To this end, we must first determine which flow regime occurs for each time step at each spatial point and then determine which set of equations to use. Therefore, in our numerical implementation, we use specific assessment criteria to determine the flow regime in each computational cell. The schematic representation of our numerical assessment can be seen in Figure 3. To avoid singularities in our numerical calculations, we set a minimum flow height  $h_{\min}$  for each flow medium in the computational domain, as is common in most depth-averaged models. Test simulations show that the influence of this minimum height on numerical results is negligible if this parameter is chosen sufficiently small. We set the minimum height in our following numerical simulations to  $h_{\min} = 1.0 \times 10^{-4}$  m.

Figure 3 illustrates the strategy implemented in our numerical scheme to determine the appropriate depth-averaged model for each computational cell. At each time step, the height and the other physical quantities of each regime/layer in each computational cell are calculated, and then the judgment for the next time step is performed. For example, if either only pure grains or pure fluid are present and the height of the saturated mixture remains the predefined minimum height, the single-layer depth-averaged model for the pure grain or pure water flow regime is applied in the corresponding computational cell. If the upper layer of pure grains or pure fluid and an underlying saturated grain-fluid mixture are present at the same time, the two-layer depth-averaged model for the under-saturated or over-saturated mixture flow regime is applied in the corresponding calculation cell.

In the case of an initially saturated grain-fluid mixture flow, where the upper layer of pure grains or pure fluid is not present, the mass transfer of grains and fluid is calculated simultaneously in each computational cell to determine whether a granular or a fluid upper layer will develop. If  $M^s > 0$  (hence  $M^f < 0$  due to the opposite signs in Equations 75 and 78), this means that a certain amount of grains from the saturated grain-fluid mixture will move upwards across the surface of the mixture, resulting in the development of a pure grain upper layer. In this case, the two-layer depth-averaged model for the under-saturated mixture regime is used in the corresponding computational cell. If, on the other hand,  $M^f > 0$  (with  $M^s < 0$ ), a fluid upper layer will develop and the two-layer depth-averaged model for the over-saturated mixture regime is used in this calculation cell. In the special case where there are neither grains nor a fluid mass transfer, that is,  $M^s = M^f = 0$ , the single-layer depth-averaged model for the saturated grain-fluid mixture regime is used.

#### 3.2. Semi-Discrete Central-Upwind Scheme

In the following, we present the semi-discrete central-upwind scheme for our model equations. For the sake of brevity, we give briefly the numerical discretization only for the two-layer depth-averaged model in the under-saturated mixture regime. The numerical formulations for the two-layer depth-averaged model in the over-saturated mixture regime and the single-layer depth-averaged models in the pure grain, pure fluid and saturated mixture regimes are analogous.

Equations 42–50 for the under-saturated mixture regime can be rewritten in vector forms as

$$\frac{\partial \mathbf{U}}{\partial t} + \frac{\partial \mathbf{F}(\mathbf{U})}{\partial x} = \mathbf{S}(\mathbf{U}) + \mathbf{N}(\mathbf{U}, U_x) + \mathbf{C}(\mathbf{U}). \quad (88)$$

here,  $\mathbf{U}$  is the vector of unknown physical quantities to be studied numerically

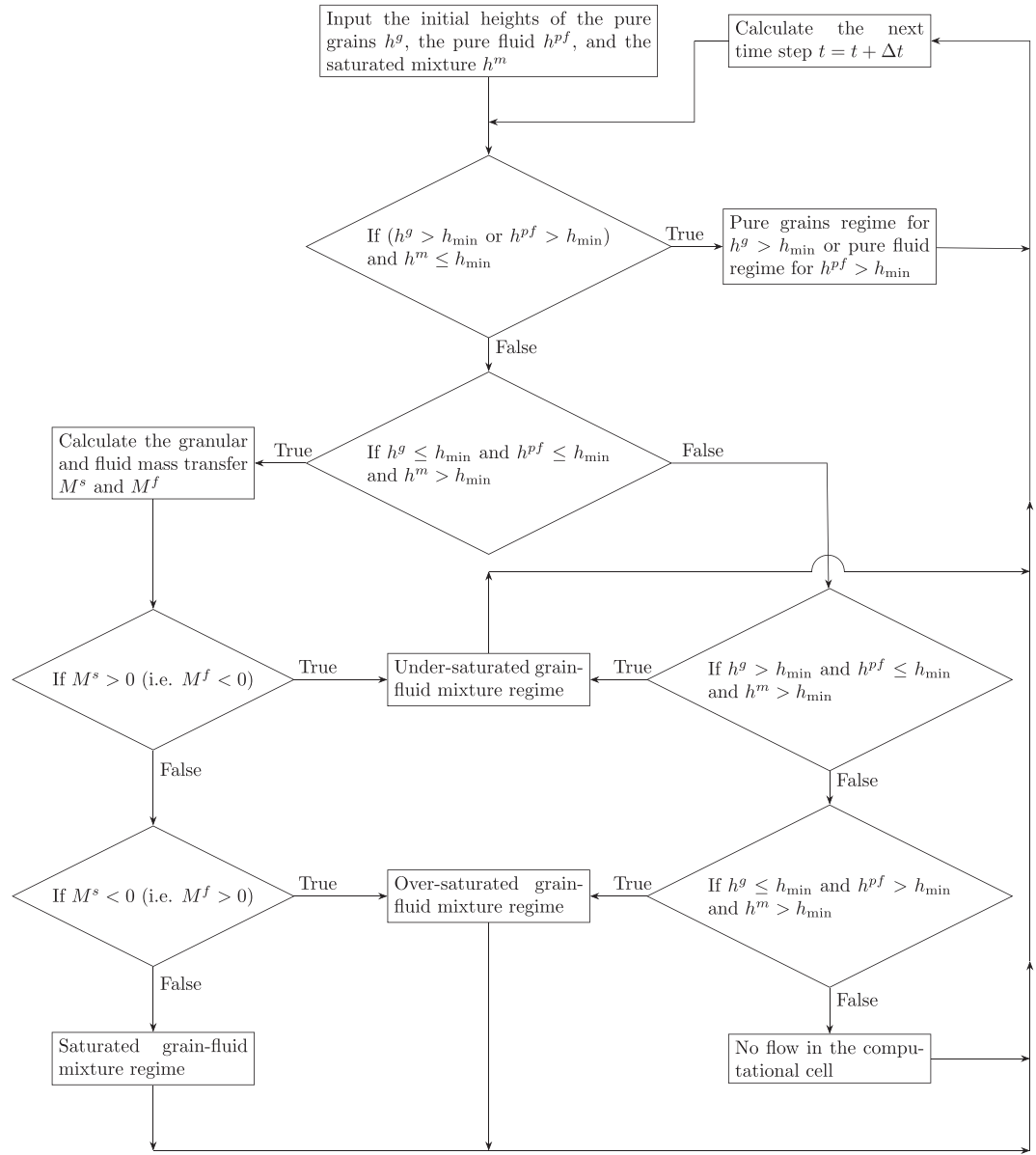


**Figure 3.** Schematic diagram of the numerical scheme for the different flow regimes.

$$\mathbf{U} = (h^g \phi^g, h^m \phi^s, h^m \phi^f, h^g \phi^g \bar{u}^g, h^m \phi^s \bar{u}^s, h^m \phi^f \bar{u}^f)^T, \quad (89)$$

and  $\mathbf{F}(\mathbf{U})$  is the convective flux vectors

$$\mathbf{F}(\mathbf{U}) = \left( h^g \phi^g \bar{u}^g, h^m \phi^s \bar{u}^s, h^m \phi^f \bar{u}^f, h^g \phi^g (\bar{u}^g)^2 + \frac{1}{2} (h^g)^2 \phi^g g \cos \zeta, \right. \\ \left. h^m \phi^s (\bar{u}^s)^2 + \frac{1}{2} (h^m)^2 \phi^s g \cos \zeta, h^m \phi^f (\bar{u}^f)^2 + \frac{1}{2} (h^m)^2 \phi^f g \cos \zeta \right)^T, \quad (90)$$

The source terms in Equations 42–50 are divided into the classical source vector  $\mathbf{S}(\mathbf{U})$ , the so-called non-conservative products  $\mathbf{N}(\mathbf{U}, \mathbf{U}_x)$  including spatial gradients but in non-conservative forms, and friction source terms  $\mathbf{C}(\mathbf{U})$ . These source terms are treated numerically differently. They take the following forms, respectively,

$$S(\mathbf{U}) = \left( \frac{M^s}{\rho^{s*}}, \quad -\frac{M^s}{\rho^{s*}}, \quad 0, \quad S_u^{g*}, \quad S_u^{s*}, \quad S_u^{f*} \right)^T, \quad (91)$$

with

$$S_u^{g*} = h^{pf} g \sin \zeta + \frac{M^s \bar{u}^{s\pm}}{\rho^{s*}}, \quad (92)$$

$$S_u^{s*} = h^m \phi^s g \sin \zeta - \frac{M^s \bar{u}^{s\pm}}{\rho^{s*}} + \frac{C^d}{\rho^{s*}} h^m (\bar{u}^f - \bar{u}^s), \quad (93)$$

$$S_u^{f*} = h^m \phi^f g \sin \zeta - \frac{C^d}{\rho^{f*}} h^m (\bar{u}^f - \bar{u}^s) - C^f |\bar{u}^f| \bar{u}^f, \quad (94)$$

$$N(\mathbf{U}, \mathbf{U}_x) = \left( 0, \quad 0, \quad 0, \quad -h^s \phi^s g \cos \zeta \frac{\partial h^m}{\partial x}, \quad -h^m g \frac{\partial (h^s \phi^s \cos \zeta)}{\partial x} + \frac{1}{2} \gamma (h^m)^2 g \cos \zeta \frac{\partial \phi^s}{\partial x}, \right. \\ \left. \frac{1}{2} (h^m)^2 g \cos \zeta \frac{\partial \phi^f}{\partial x} \right)^T, \quad (95)$$

$$\mathbf{C}(\mathbf{U}) = (0, \quad 0, \quad 0, \quad \mathcal{T}_u^i, \quad -\mathcal{T}_u^i - \mathcal{T}_u^b, \quad 0)^T, \quad (96)$$

where the granular interfacial friction  $\mathcal{T}_u^i$  and basal friction  $\mathcal{T}_u^b$  in the under-saturated mixture regime are

$$\mathcal{T}_u^i = \frac{\bar{u}^s - \bar{u}^g}{|\bar{u}^s - \bar{u}^g|} \mu^i (h^s \phi^s g \cos \zeta + \kappa h^s \phi^s (\bar{u}^s)^2), \quad (97)$$

$$\mathcal{T}_u^b = \frac{\bar{u}^s}{|\bar{u}^s|} \mu^b \left[ \frac{p_b^p}{\rho^{s*}} + \kappa h^m \phi^s \left( (\bar{u}^s)^2 - \gamma (\bar{u}^f)^2 \right) + h^s \phi^s g \cos \zeta + \kappa h^s \phi^s (\bar{u}^s)^2 \right]. \quad (98)$$

The computation domain is discretized with uniform cells  $I_j = [x_{j-\frac{1}{2}}, x_{j+\frac{1}{2}}]$ , where the subscript  $j$  denotes the numbering of the computational grid. The boundaries of each cell are given by  $x_{j\pm\frac{1}{2}} = x_j \pm \Delta x/2$ , where  $\Delta x = x_{j+1} - x_j$ . In each cell  $I_j$ , the cell-averaged variable  $\bar{U}_j(t)$  is defined as

$$\bar{U}_j(t) = \frac{1}{\Delta x} \int_{I_j} \mathbf{U}(t, x) dx, \quad (99)$$

which is updated through the semi-discrete ordinary differential equation,

$$\frac{d}{dt} \bar{U}_j(t) = -\frac{\mathbf{H}_{j+\frac{1}{2}}(t) - \mathbf{H}_{j-\frac{1}{2}}(t)}{\Delta x} + \bar{\mathbf{S}}_j(t) + \bar{\mathbf{N}}_j(t) + \bar{\mathbf{C}}_j(t), \quad (100)$$

where the cell-averaged source, non-conservative and friction terms are

$$\bar{\mathbf{S}}_j(t) = \frac{1}{\Delta x} \int_{I_j} \mathbf{S}(\mathbf{U}(t, x)) dx, \quad \bar{\mathbf{N}}_j(t) = \frac{1}{\Delta x} \int_{I_j} \mathbf{N}(\mathbf{U}(t, x), \mathbf{U}_x(t, x)) dx, \\ \bar{\mathbf{C}}_j(t) = \frac{1}{\Delta x} \int_{I_j} \mathbf{C}(\mathbf{U}(t, x)) dx. \quad (101)$$

The central-upwind numerical flux  $\mathbf{H}_{j+\frac{1}{2}}(t)$  is given by Kurganov and Tadmor (2000) as

$$\mathbf{H}_{j+\frac{1}{2}}(t) = \frac{\mathbf{F}(\mathbf{U}_{j+\frac{1}{2}}^-(t)) + \mathbf{F}(\mathbf{U}_{j+\frac{1}{2}}^+(t))}{2} - \frac{a_{j+\frac{1}{2}}(t)}{2} (\mathbf{U}_{j+\frac{1}{2}}^+(t) - \mathbf{U}_{j+\frac{1}{2}}^-(t)), \quad (102)$$

where  $a_{j+\frac{1}{2}}(t)$  is the maximum wave speed. In Equation 102,  $U_{j+\frac{1}{2}}^\pm(t)$  are the right and left point values of a piecewise linear reconstruction at  $x = x_{j+\frac{1}{2}}$ , given by

$$U_{j+\frac{1}{2}}^+(t) = \bar{U}_{j+1}(t) - \frac{\Delta x}{2}(U_x)_{j+1}(t), \quad U_{j+\frac{1}{2}}^-(t) = \bar{U}_j(t) + \frac{\Delta x}{2}(U_x)_j(t). \quad (103)$$

To maintain the non-oscillatory property of the numerical scheme, the numerical derivatives  $(U_x)_j(t)$  are constructed using a TVD slope limiter. In the present study, a generalized minmod limiter is used, which is given by

$$(U_x)_j(t) = \text{minmod}\left(\theta \frac{\bar{U}_{j+1}(t) - \bar{U}_j(t)}{\Delta x}, \frac{\bar{U}_{j+1}(t) - \bar{U}_{j-1}(t)}{2\Delta x}, \theta \frac{\bar{U}_j(t) - \bar{U}_{j-1}(t)}{\Delta x}\right), \quad (104)$$

with the parameter  $\theta \in [1, 2]$ . It should be noted that in the numerical discretization of the non-conservative products  $\bar{N}_j(t)$ , for example, represented by the term  $-h_j^s \phi_j^s g \cos \zeta_j (\partial h^m / \partial x)_j$ , the gradient  $(\partial h^m / \partial x)_j$  is also calculated using the minmod limiter.

In order to extend the currently used dynamic  $\mu(I)$  or  $\mu(I_s)$  rheology to the description of grains in a static state, we use an operator splitting method to treat the granular friction terms in the semi-discrete ordinary differential Equation 100 (e.g., see Mangeney-Castelnau et al., 2003; Mangeney-Castelnau et al., 2005; Mangeney et al., 2007). This method is represented by the following system of equations:

$$\begin{cases} \frac{d}{dt} \bar{U}_j^*(t) = -\frac{H_{j+\frac{1}{2}}(t) - H_{j-\frac{1}{2}}(t)}{\Delta x} + \bar{S}_j(t) + \bar{N}_j(t), \\ \frac{d}{dt} \bar{U}_j(t) = \bar{C}_j^*(t). \end{cases} \quad (105)$$

In the first step of Equation 105, we calculate an intermediate solution without friction term, denoted as  $\bar{U}_j^*(t)$ , by applying a second-order Runge-Kutta solver (Kurganov & Tadmor, 2000) to the first equation of Equation 105. In a second step, the contribution of the friction term is then taken into account, which is treated as the source term in second equation of Equation 105.

For simplicity, we present this method here only for the pure grain flow regime. In this case, the non-conservative term  $\bar{N}_j(t) = 0$ , and we denote the flow thickness and the momentum of the pure grains in the numerical cell  $I_j$  as  $(\bar{q}_1)_j = (h^s \phi^s)_j$  and  $(\bar{q}_2)_j = (h^s \phi^s \bar{u}^s)_j$ , respectively. Thus, the cell averaged variable is  $\bar{U}_j(t) = [(\bar{q}_1)_j(t), (\bar{q}_2)_j(t)]^T$ . In the second step of Equation 105, the momentum at the new time step  $(\bar{q}_2)_j(t + \Delta t)$  is updated according to the following criterion:

$$(\bar{q}_2)_j(t + \Delta t) = \begin{cases} (\bar{q}_2)_j + (\mathcal{T}_g^{b*})_j \Delta t, & \text{if } |(\bar{q}_2)_j| > \sigma_j^* \Delta t, \\ 0, & \text{otherwise,} \end{cases} \quad (106)$$

where  $(\mathcal{T}_g^{b*})_j$  is the component of  $\bar{C}_j^*(t)$  for the momentum balance equation, that is, the basal granular friction, and  $\sigma_j^*$  represents the yield stress, which according to the source term (68) are given by

$$(\mathcal{T}_g^{b*})_j = -\frac{(\bar{q}_2)_j}{|(\bar{q}_2)_j|} \sigma_j^*, \quad \sigma_j^* = \mu^b g \cos \zeta(\bar{q}_1)_j + \mu^b \kappa \frac{(\bar{q}_2)_j^2}{(\bar{q}_1)_j}. \quad (107)$$

This criterion evaluates whether the momentum in the numerical cell  $I_j$  exceeds a critical threshold  $\sigma_j^* \Delta t$ . If the momentum is below this threshold, that is, if the momentum is not large enough to overcome the frictional force, the grains come to rest in this numerical cell. Otherwise, the momentum for the new time step is calculated with the effect of the frictional force by using  $\mu(I)$  rheology. It should be noted that when the granular mass reaches a

static state, the granular basal friction for the pure granular regime balances with the depth-averaged pressure gradient term in the momentum balance Equation 67 and the gravity in source term (68), resulting in a static granular basal friction that is smaller than the second term of Equation 68 (the  $\mu(I)$  friction force). Of course, this is no longer in our interest. Several previous studies have employed elasto-viscoplastic models to capture a wide range of granular flow behaviors. These models incorporate an elastic response for stress states below the yield criterion, allowing the modeling of the solid-like elastic behavior of grains in a static state. These models are integrated with  $\mu(I)$  or  $\mu(I_v)$  rheology to account for the dynamic response when the stress exceeds the yield criterion (e.g., Baumgarten & Kamrin, 2019; Dunatunga & Kamrin, 2015). Additionally, in the under-saturated mixture flow regime, the interfacial frictional forces between the upper and lower layers make the operator splitting method for handling the friction terms in the upper pure grain layer and the lower mixture layer more complex than that for the single-layer pure grain flows. This method for the under-saturated mixture regime is detailed in Appendix E.

In the numerical calculations, we need to treat all five possibly occurring flow regimes and their transitions simultaneously. Therefore, we must determine the terms on the right-hand side of Equation 100 for the different flow regimes, especially for the transition points between these regimes. The specific methods are as follows.

As an example, we consider the transition between an under-saturated mixture regime and a saturated mixture regime. At each time step, the flow heights  $h_j^s$  and  $h_j^m$  are first determined to establish the flow regime in the current cell  $I_j$  according to the strategy outlined in Figure 3. When the pure grain upper layer disappears and only the saturated mixture lower layer is present, that is,  $h_j^s \leq h_{\min}$  and  $h_j^m > h_{\min}$ , the corresponding terms in Equations 91–96 for the pure grains are set to zero, while the source, non-conservative and friction terms for the saturated mixture flow remain.

Next, for the numerical flux  $\mathbf{H}_{j+\frac{1}{2}}(t)$  in Equation 100, we calculate the flow heights  $(h^s)_{j+\frac{1}{2}}^\pm$  for the pure grains layer and  $(h^m)_{j+\frac{1}{2}}^\pm$  for the saturated mixture layer using Equation 103 at the right-side boundary  $x = x_{j+\frac{1}{2}}$  of the current cell  $I_j$ . If

$$(h^s)_{j+\frac{1}{2}}^- > h_{\min} \quad \text{and} \quad (h^s)_{j+\frac{1}{2}}^+ \leq h_{\min}, \quad \text{and} \quad (h^m)_{j+\frac{1}{2}}^\pm > h_{\min}, \quad (108)$$

this condition indicates the cell boundary  $x = x_{j+\frac{1}{2}}$  is a transition point between the two regimes with an under-saturated mixture regime on the left-hand side and a just saturated mixture regime on the right-hand side of  $x = x_{j+\frac{1}{2}}$ . In this case, the flux term  $\mathbf{F}(U_{j+\frac{1}{2}}^+(t))$  for the pure grains upper layer is set to zero, that is,  $\mathbf{F}(U_{j+\frac{1}{2}}^+(t)) = 0$ , while the flux term  $\mathbf{F}(U_{j+\frac{1}{2}}^+(t))$  for the saturated mixture lower layer is calculated using the second terms on the left-hand side of Equations 60–63. The flux term  $\mathbf{F}(U_{j+\frac{1}{2}}^-(t))$  is calculated using Equation 90 for both the pure grains upper layer and the saturated mixture lower layer in Equation 102. To calculate the numerical flux  $\mathbf{H}_{j-\frac{1}{2}}(t)$  in Equation 100 at the left-side boundary  $x = x_{j-\frac{1}{2}}$  of the current cell  $I_j$ , we apply the same method as above. Analogously, this numerical treatment is also applied to the transitions between the other flow regimes to ensure that all possible transitions are handled accurately.

It should be noted that in our numerical simulations, the mass and the momentum of both the granular and the fluid phases are conserved, ensuring the conservation of total mass and total momentum. In our investigations, the mass and the momentum balance equations of both the granular and the fluid phases are used. In the under-saturated or over-saturated mixture flow regime, the mass and momentum jump conditions at the interface between the upper and lower layers represent the mass and momentum conservation of grains/fluid across the interface. Additionally, the high-resolution central-upwind scheme with a TVD slope limiter used in our numerical simulation is a conservative numerical scheme that ensures mass and momentum conservation for both phases. In our numerical simulations, the only possibility that could lead to the non-conservation of the mass and momentum is the introduction of the minimum height  $h_{\min}$ . However, the value of  $h_{\min}$  is chosen so small (i.e.  $h_{\min} = 1.0 \times 10^{-4}$  m) that its effect on the conservation of mass and momentum is negligible. Our numerical simulations for various cases have demonstrated a very good conservation of the total masses for both phases.

Moreover, local wave speeds  $a_{j\pm\frac{1}{2}}(t)$  in the numerical fluxes  $\mathbf{H}_{j\pm\frac{1}{2}}(t)$ , are calculated by solving eigenvalue problems of the Jacobian matrix  $\mathbf{A} = \partial\mathbf{F}/\partial\mathbf{U}$ ,

$$|\lambda \mathbf{1} - \mathbf{A}| = 0. \quad (109)$$

The characteristic Equation 109 can take different forms depending on the flow regime. Specifically, it can manifest as a sixth-order polynomial equation in the under-saturated and over-saturated mixture regimes, a fourth-order polynomial equation in the single-layer saturated mixture regime, or a second-order polynomial equation in the single-layer pure grain and pure fluid regimes. The solutions of this polynomial equation determine whether the system of Equation 88 is well-posed or ill-posed. However, obtaining an explicit solution for a sixth-order or fourth-order polynomial equation poses mathematical challenges. Moreover, in the under-saturated and over-saturated mixture regimes, as the velocity difference between the layers becomes large, the system of Equation 88 in a multi-layer model tends to lose its hyperbolic property (Pelanti et al., 2008). The technique to prevent the system of equations from degenerating into an ill-posed state has been explored in several previous studies. Baker et al. (2016) introduced high-order depth-averaged viscous-like terms derived from  $\mu(I)$  rheology to regularize the system. These viscous terms turn out to be crucial for other problems as well, for example, for the prediction of the cut-off frequency of roll waves and the determination of the width of self-channeled flows (Gray & Edwards, 2014; Rocha et al., 2019), so that there is independent evidence for them. Sarno, Wang, et al. (2021) suggested that the introduction of mass and momentum exchange across the interface between the layers could exempt the multi-layer model from ill-posedness. This approach is also appropriate for our present model, since in the flows investigated here mass and momentum transfer physically occur at the layer interface. To confirm that our system is well posed, we have carried out an investigation of the grid dependence in our numerical simulations. It turns out that the simulation remains stable and convergent when the grid is refined, and that no unphysical oscillations occur even with a very fine grid.

In the present study, to calculate wave speeds for the numerical fluxes in Equation 100, we only estimate the bounds on the eigenvalues of the Jacobian matrix (109) by using the Lagrange theorem, and a real value within this interval is then selected (see Kurganov & Miller, 2014; Mignotte & Stefanescu, 2002). As the central-upwind scheme is an explicit scheme, the Courant-Friedrichs-Levy (CFL) condition

$$\Delta t \cdot \frac{a}{\Delta x} < Cr, \quad \text{where } a = \max\{|a_i|\}, \quad i = 1, \dots, 6, \quad (110)$$

needs to be satisfied to ensure numerical stability, where  $Cr$  is the Courant number and is usually chosen smaller than one. To satisfy the constraints of the source terms on the time step and ensure a small numerical error, we set a much smaller Courant number of  $Cr = 0.01$  for the numerical simulations.

## 4. Numerical Results

In this section, we utilize the numerical method described in Section 3 to validate the present depth-averaged model by conducting simulations of various scenarios, including saturated granular column collapse in air, dry and partially immersed granular columns collapse, and pure grain and water-saturated grain mixture landslides, and comparing them with experimental data presented by Ceccato et al. (2020), He et al. (2022), and Taylor-Noonan et al. (2022), respectively. Furthermore, to obtain a more comprehensive understanding of the solid-fluid separation phenomena in the grain-fluid mixture flow, we also simulate the behavior of saturated grain-fluid mixture flows in a rotating drum. In the following graphical representations, the experimental data are represented by dashed lines, while our simulated results are shown using solid lines. To distinguish between the different flow regimes, we use red, black, and blue lines to represent the surface/interface of the pure grains, saturated grain-fluid mixture, and pure fluid, respectively.

### 4.1. Collapse of Saturated Granular Column in Air

Ceccato et al. (2020) conducted a small-scale laboratory experiments of saturated column collapses to investigate the interactions between grains and interstitial fluid. In their experiments, the fluid-saturated material was released in air, which enables a better representation of real natural onshore landslides and facilitates the analysis of solid-fluid separation. In the experiments, the saturated granular column was placed in a horizontally lying glass flume with dimensions of 0.7 m in length, 0.05 m in width, and 0.12 m in height, and was initially constrained by a move-able vertical gate. The initial geometry of the column was characterized by a length of

**Table 2**  
*Selected Parameters in Our Numerical Simulations for the Experiments of Ceccato et al. (2020)*

Parameter	Model values	References
Diameter, $d$	$2.5 \times 10^{-3}$ m	Experimental measurement
Fluid density, $\rho^{f*}$	1,000 kg m <sup>-3</sup>	Experimental measurement
Fluid viscosity, $\eta^f$	0.02 Pa · s	–
Solid density, $\rho^{s*}$	2,650 kg m <sup>-3</sup>	Experimental measurement
Initial solid volume fraction, $\phi^s$	0.6	Experimental measurement
Pure granular friction coefficient $\mu_1^g$ ,	0.595	Rauter (2021)
Pure granular friction coefficient $\mu_2^g$ ,	0.895	Rauter (2021)
Fluid-saturated granular friction coefficient $\mu_1^f$ ,	0.32	Boyer et al. (2011)
Fluid-saturated granular friction coefficient $\mu_2^f$ ,	0.7	Boyer et al. (2011)
Static critical granular volume fraction, $\phi^c$	0.585	Boyer et al. (2011)
Dilatancy parameter, $K_2$	25.0	Pailha and Pouliquen (2009)
Dilatancy parameter, $K_3$	4.09	Pailha and Pouliquen (2009)
Dilatancy parameter, $K_4$	1.8	Pailha and Pouliquen (2009)

$L_0 = 0.04$  m and a height of  $H_0 = 0.06$  m. The granular material had a uniform granulometric distribution with a mean diameter of  $d = 2.5 \times 10^{-3}$  m and a grain density of  $\rho^{s*} = 2626$  kg/m<sup>3</sup>. To improve visualization of the solid-fluid separation, the fluid phase was water dyed with a natural colorant and had a density of  $\rho^{f*} = 1000$  kg/m<sup>3</sup>. The initial solid volume fraction was controlled with an average value of  $\phi^s = 0.6$  in the experiments. As the move-able vertical gate was removed, the fluid-saturated granular column began to collapse, and the entire process was captured using a high-speed camera. The camera recorded run-out profiles as well as the separation between the solid and fluid phases. Additionally, they also conducted numerical simulations for these saturated granular column collapses using a two-phase double-point Material Point Method (2P-DP MPM). This method was initially introduced by Abe et al. (2014) and later extended by Bandara and Soga (2015) and Martinelli and Rohe (2015). In their numerical computations, a linear-elastic perfectly plastic model with a Mohr-Coulomb failure criterion was applied to the solid phase, and a Newtonian model was employed to describe the fluid phase. It should be noted that the formulation of the interaction between the granular and fluid phases in their model differs from that in our model.

In our numerical simulations, the computation domain follows the experimental setup, and the physical parameters used in the computation were obtained from experimental measurements. However, some parameters such as  $\phi^c$ ,  $K_2$ ,  $K_3$  and  $K_4$  as well as the granular friction coefficients were not directly measured in the experiments. For these parameters, we used values obtained from other studies. Specifically, we utilized the granular dilatancy effect parameters from the work of Pailha and Pouliquen (2009), the pure granular friction coefficients in the  $\mu(I)$  rheology from the study of Rauter (2021), and the fluid-saturated granular friction coefficients in the  $\mu(I_v)$  rheology from the work of Boyer et al. (2011). All the parameters used in this computation are summarized in Table 2. It should be noted that the selected parameters from other studies, in which different materials were used, may lead to deviations in numerical results compared to experimental data.

Figure 4 illustrates a comparison between their experimental and numerical results and our numerical simulations concerning the temporal evolution of the collapse profiles. The length and height of the profiles are normalized by the initial column height  $H_0$ , and time is normalized with respect to a reference time, defined as  $t_{\text{ref}} = \sqrt{H_0/g(1 - \rho^{f*}/\rho^{s*})}$ . In the initial stage of the collapse, as depicted in Figure 4a, our numerical simulation exhibits a faster flow compared to their experimental and numerical results. A primary reason for this discrepancy is the use of depth-averaged models in our numerical simulation. It is known that the depth-averaged model tends to overestimate the flow velocity at the beginning of the flow (Bouchut et al., 2017; Mangeney-Castelnau et al., 2005). Similar to their numerical simulation result, a layer of pure grains emerges above the fluid-saturated mixture during the flow. However, the extent of separation of the grains from the water-saturated mixture was not clearly established in the experiment. Moreover, there is a small outflow of pure water at the flow

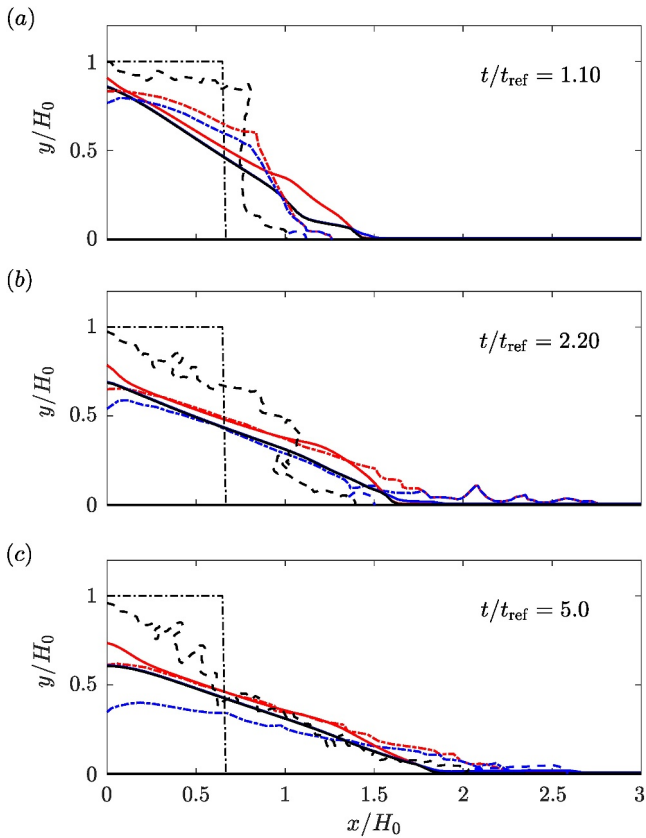


**Figure 4.** Collapse of fluid-saturated granular columns at different time instants. The experimental measurements from Ceccato et al. (2020) are represented by dashed lines, where black dashed lines denote the particle surface profiles, and blue dashed lines indicate the surfaces of the flowing out pure fluid in the front. Their simulated surfaces of particles and fluid obtained using 2P-DP MPM are illustrated by red and blue dash-dotted lines, respectively. Our simulated surfaces for pure grains, fluid-saturated mixture, and outflow of pure fluid are shown by red, black, and blue solid lines, respectively. The initial column shapes are displayed by black dash-dotted lines.

granular columns were experimentally generated by adding water to the dry granular column until both the upper layer of dry particles and the lower layer of water-saturated particles had the same initial height of 0.08 m. The intrinsic density of interstitial water is  $\varphi^{s*} = 1.0 \times 10^3 \text{ kg/m}^3$  and the viscosity of water is  $\eta^f = 1 \times 10^{-3} \text{ Pa} \cdot \text{s}$  in their experiments.

In our numerical simulations, we employ the  $\mu(I)$  rheology for the granular friction in the upper layer of dry particles and the  $\mu(I_v)$  rheology for the granular friction in the lower layer of the saturated mixture in the partially immersed columns. It is noteworthy that the experiments conducted by He et al. (2022) provided only a single granular friction angle, specifically in the range of  $24.8^\circ$ – $26.0^\circ$  for fine dry particles and  $29.8^\circ$ – $31.0^\circ$  for coarse dry particles. However, the application of the  $\mu(I)$  rheology necessitates an additional friction angle. Typically,  $\mu_2^g > \mu_1^g$ , with the value of  $\mu_1^g$  falling in a range slightly greater than  $\tan(20^\circ)$  and the value of  $\mu_2^g$  in a range greater than  $\tan(30^\circ)$ . In the work of Meng et al. (2022), they adopted  $\mu_1^g = \tan(24.57^\circ)$  and  $\mu_2^g = \tan(36.5^\circ)$ , with the value of  $\mu_1^g$  closely matching the friction coefficient for fine dry particles in the experiments of He et al. (2022). Consequently, we selected the value of  $\mu_2^g$  to be the same as that in Meng et al. (2022), that is,  $\mu_2^g = \tan(36.5^\circ)$  in our numerical simulations. Additionally, there is no available data for granular friction coefficients in the saturated mixture in their experiments. Generally, the values of  $\mu_1^s$  and  $\mu_2^s$  in the  $\mu(I_v)$  rheology differ from the values of  $\mu_1^g$  and  $\mu_2^g$  in the  $\mu(I)$  rheology. For these coefficients, we adopt values from the work of Boyer et al. (2011), that is,  $\mu_1^s = 0.32$  and  $\mu_2^s = 0.7$  in the  $\mu(I_v)$  rheology, which are consistent with the values in Table 2. In the study by

front in both our numerical simulations and their experiments, while the front in their numerical simulation consists of a water-saturated mixture.

At the dimensionless time  $t/t_{\text{ref}} = 2.20$ , as shown in Figure 4b, their simulation result is faster than the experiments and our numerical result. They attributed this to the use of the Mohr-Coulomb constitutive model for the granular phase, and their model did not consider the influence of negative excess pore fluid pressure, which can reduce granular mobility. In our numerical simulation, we employ different constitutive models for the granular friction, namely, the  $\mu(I)$  rheology for the pure grains region and  $\mu(I_v)$  rheology for the grains in the fluid-saturated mixture region. Additionally, our model incorporates the influence of negative excess pore fluid pressure through the granular dilatancy effects. These factors enable our model to better capture the flow behavior at this stage than their model.

At the time of deposit,  $t/t_{\text{ref}} = 5.0$ , as indicated in Figure 4c, the run-out distance of grains in our numerical simulation is slightly smaller than in their experimental and numerical results. In both our numerical simulation and their experiment, a thin layer of pure water appears at the front of the flow, whereas in their simulation they observed that the fluid slowly flowed out of the particles after this time. In this experiment, the measured free surface of the particle flow is not smooth. Neither our nor their numerical simulations are able to accurately capture the non-smooth free surface. Our numerical simulation shows an improvement in predicting the deposition height on the left part of the flow compared to their numerical simulation. However, there is still a discrepancy with the experimental results.

#### 4.2. Collapse of Dry and Partially Immersed Granular Columns

He et al. (2022) designed small-scale experiments of subaerial dry and partially immersed granular columns collapses to investigate the effect of interstitial water on the flow dynamic of the partially saturated granular columns. The experiments used ceramic beads of different particle sizes (for fine particles with the diameter of  $d = 0.84 \text{ mm}$  and for coarse particles with  $d = 6.02 \text{ mm}$ ). The intrinsic density of particles is  $\varphi^{s*} = 3.6 \times 10^3 \text{ kg/m}^3$  and the granular volume fraction was 0.6. Both dry and partially immersed granular columns were initially prepared in the reservoir with a constant length of  $L_0 = 13 \text{ cm}$  and a height of  $H_0 = 16 \text{ cm}$ . The partially immersed

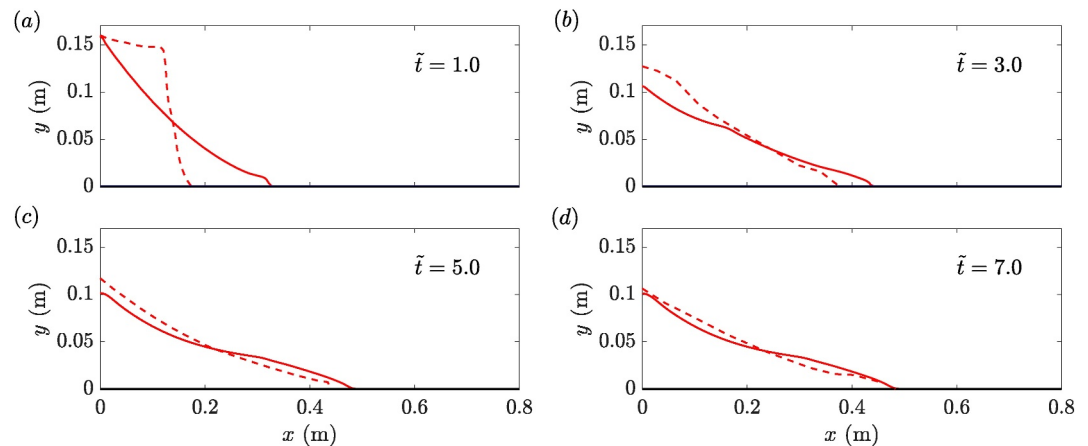


**Figure 5.** Comparison of experimental measurements by He et al. (2022) (red dashed lines) with predictions from the present theory (red solid lines) for the collapse of a dry granular column at different non-dimensional time instants. The non-dimensional time is defined as  $\tilde{t} = t/\sqrt{H_0/g}$ .

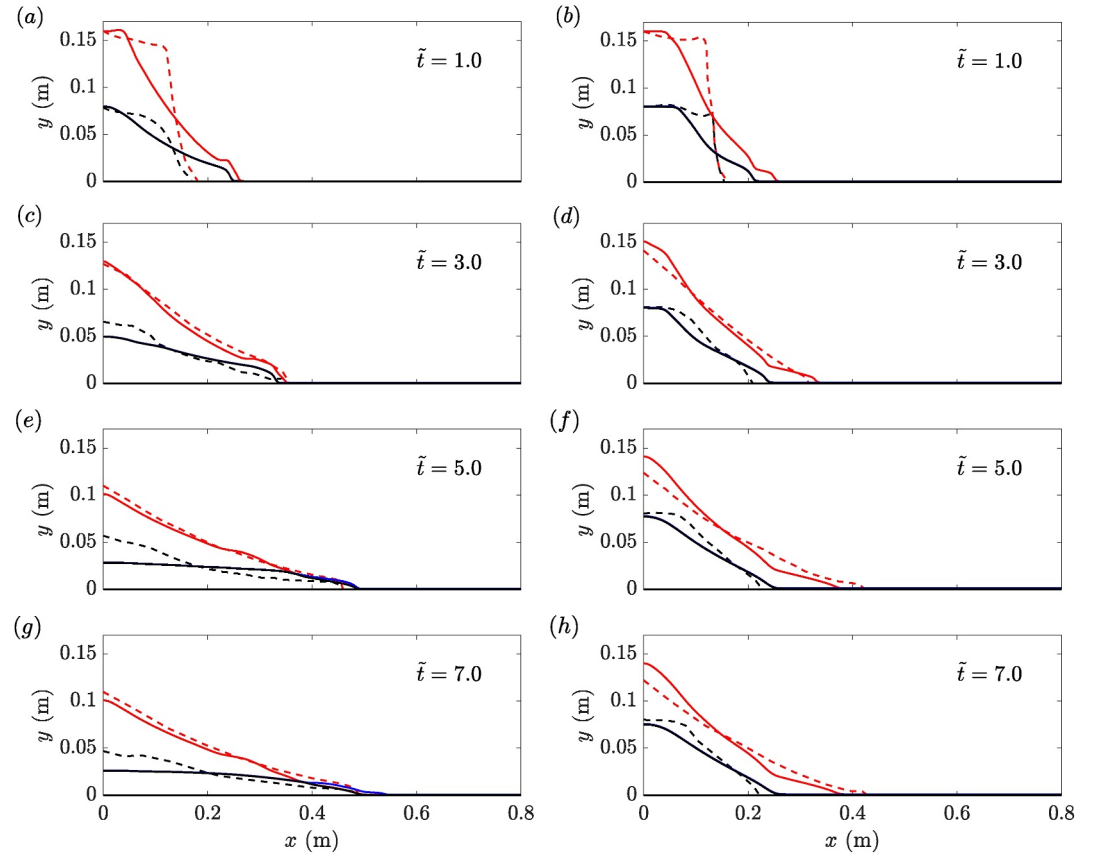
Rauter (2021), different friction coefficients were also employed for dry and wet granular materials, with the friction coefficients in the  $\mu(I_v)$  rheology being smaller than those in the  $\mu(I)$  rheology. In addition to the friction coefficients of the particles, the other physical parameters for both particles and water in our numerical simulations are the same as those in the experiments.

Figure 5 illustrates a comparison between the experimental and numerical results regarding the temporal evolution of flow profiles for a dry granular material. Due to the small impact of particle size on the collapse of the dry granular column, as discussed in He et al. (2022), we present only the comparison between the experimental and numerical results pertaining to the fine particles. At the initial stage of the collapse, as shown in Figure 5a, our numerical simulation exhibits a higher speed than observed in the experiments, aligning with the finding of the first experiment. As mentioned above, this could be a significant drawback of the depth-averaged model. However, in subsequent times, our numerical simulation is able to capture the flow behavior observed in the experiment well.

In addition to the experiment on the collapse of the dry granular column, we also compare the predictions from our present depth-averaged models with experiments on the collapse of partially immersed granular columns containing both coarse and fine particles, as illustrated in Figure 6. It is observed that, for both coarse and fine particles, our numerical simulations indicate a faster collapse than observed in the experiments during the initial stages. In the case of coarse particles, depicted on the left side of Figure 6, the upper layer of pure particles moves forward together with the lower layer of water-saturated particles at the beginning of the collapse (Figure 6a, 6c). In subsequent times (Figure 6e, 6g), the purely granular upper layer in the flow front becomes negligibly thin, while in the flow tail, it remains relatively thick. This is attributed to the weak grain-fluid interaction for coarse grains, allowing the fluid to flow out from the mixture into the grains at the front. However, during the deposition stage, the saturated mixture in the numerical simulation is thinner at the tail of the flow and thicker at the front, compared to the experimental observation. In the case of fine particles, as indicated on the right side of Figure 6, the fine particles exhibit a strong interaction with interstitial water, resulting in a negligible difference in velocity between the particles and water in the lower layer mixture, making it difficult to separate water from the mixture. Additionally, the dilatancy effect plays a crucial role in this case. Since the partially immersed granular columns are initially densely packed, the particles undergo dilatation under shear, leading to negative excess pore fluid pressure, which increases friction between the water-saturated particles. As a result, the water-saturated particle mixture moves slowly, while the upper layer of pure particles moves rapidly, forming a pure particle layer in the front.

### 4.3. Landslides of Dry Grains and Initially Water-Saturated Grain Mixture

In this section, the experimental measurements of Taylor-Noonan et al. (2022) on the temporal and spatial evolution of dry grains and initially water-saturated grain mixture sliding down a slope and the corresponding



**Figure 6.** Comparison of experimental measurements by He et al. (2022) (dashed lines) with predictions from the present theory (solid lines) for the collapse of partially saturated granular columns with coarse particles on the left side and fine particles on the right side at different non-dimensional time instants. The non-dimensional time is defined as  $\tilde{t} = t/\sqrt{H_0/g}$ . The red lines show the surface profiles of the pure granular upper layer, and the black lines represent the surface profiles of the water-saturated mixture. In panels (e) and (g), the almost invisible blue solid line in the front represents the surface of the flowing-out water in the simulation.

simulation results using our depth-averaged model are presented and compared. In their experiments, the diameter of the used ceramic particles is  $d = 3.84$  mm and the intrinsic particle density is  $\rho^{s*} = 2241$  kg/m<sup>3</sup>. The initial solid volume fractions of the dry grains and the initially water-saturated grain mixture are  $\phi^s = 0.63$ , which is close to the random close packing of spheres with  $\phi_s \approx 0.64$  (Allen et al., 1999). The intrinsic density of water is  $\rho^{f*} = 1000$  kg/m<sup>3</sup> and the water viscosity is  $\eta^f = 1 \times 10^{-3}$  Pa · s. The topography of their experiments is a slope, which consists of a 8.23 m long section inclined at 30° from horizontal and a 33 m long horizontal run-out section. In these experiments, Taylor-Noonan et al. (2022) did not provide relevant experimental measurements on the granular friction coefficients, neither for dry nor for wet particles. Recently, Meng et al. (2024) performed numerical simulations for these experiments using their depth-averaged model and obtained a good fit to the measured deposition for dry grains in Taylor-Noonan et al. (2022) using the granular friction coefficients of  $\mu_1^g = \tan(22.2^\circ)$  and  $\mu_2^g = \tan(25.6^\circ)$  for ceramic beads on aluminum. We adopt these values in our numerical simulations, which leads to a similar simulated deposition morphology for dry grains that agrees well with the experimental result, as shown in Figure 7a.

With regard to the granular friction coefficients  $\mu_1^f$  and  $\mu_2^f$  of the  $\mu(I_v)$  rheology for the grains in the water-saturated mixture, we still adopt the values specified in Table 2. Additionally, the experiments on the initially water-saturated grain mixture by Taylor-Noonan et al. (2022) suggest that a critical solid volume fraction  $\phi^c = 0.585$  is a good approximate mean value (see their Figure 7). The parameters for the granular dilatancy model also remain as outlined in Table 2. Using these parameters, the comparison between the simulated and measured deposition morphologies for the initially water-saturated grain mixture are presented in Figure 7b. The

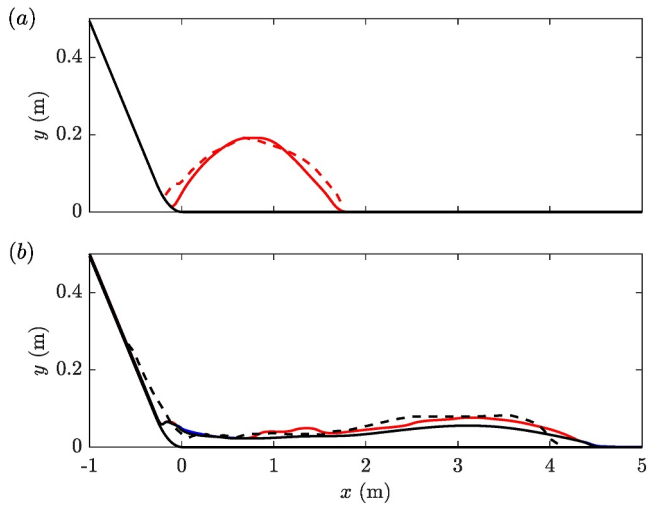


**Figure 7.** Comparison between the experimentally measured deposition morphology from Taylor-Noonan et al. (2022) (dashed lines) and the simulated results using the present model (solid lines) for (a) the dry grains and (b) the initially water-saturated grain mixture, each with an initial volume of  $0.4 \text{ m}^3$ . The dry grain surface is represented by the red lines. In panel (b), the black dashed line shows the experimental free surface, and the black solid lines represent the simulated surface of the saturated mixture. The almost invisible blue solid line at the front and tail of the flow represents the surface of the flowing-out water in the simulation. The vertical axis is magnified by a factor of four for better visualization.

numerical simulation describes the experimental results qualitatively and even quantitatively in terms of the front position and flow height. However, some discrepancies are observed. The flow front in the simulation exhibits a longer run-out distance and a flatter shape compared to the experimental deposit. Additionally, a long thin layer of the mixture remains at the flow tail on the slope in the experiments, whereas the numerical simulation shows a short thin layer of the mixture deposit at the transition between the slope and the horizontal plate. These discrepancies may indicate that the assumed granular friction of the grains in the water-saturated mixture is underestimated in the numerical simulation.

Taylor-Noonan et al. (2022) recorded the temporal evolution of flow heights for both the dry grains and the initially water-saturated grain mixture using a high-speed camera positioned 6.23 m downstream from the initial flow front on the slope, as shown in the insets of Figure 8. The comparisons between the experimentally measured and simulated temporal evolution of flow heights for both the dry grains and the initially water-saturated grain mixture are presented in Figure 8. In the case of the dry grains, depicted in Figure 8a, the simulated flow height is much lower than the experimental measurement. This discrepancy is due to the fact that in the experiments, the dry grains dilute near the free surface during flow, making it more difficult to determine the free surface, as also mentioned by Meng et al. (2024). Additionally, the granular dilatancy effect in the dry grains is not accounted for in our depth-averaged model.

In the case of the initially water-saturated grain mixture, shown in Figure 8b, the simulated flow transitions to a mainly under-saturated mixture due to the dilatancy effect, which is in qualitative agreement with the experimental observations. The flow front consists of a small portion of pure grains followed by an under-saturated mixture. The peak height occurs within the first second after the initial front arrives at the camera, and the flows become much thinner and slower two seconds after the initial front arrival. In the experiment, the flow front is highly under-saturated, but not completely dry. At the flow front, the simulated height of the water-saturated mixture is greater than observed experimentally, whereas the thickness of the pure grain upper layer is less than in the experiment. This discrepancy may be due to an underestimation of the dilatancy effect in the numerical simulation. At the tail of the flow, the simulated flow is almost a water-saturated mixture. Additionally, the viscosity of the interstitial water suppresses the dilatancy of the grains at the free surface, which leads to a better comparison between experimental and numerical results than for the dry grains.

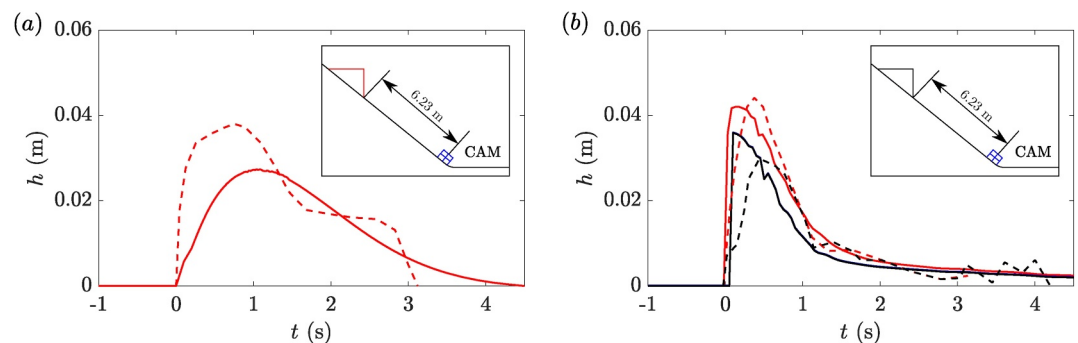


**Figure 8.** Temporal evolution of the flow heights at a given position “CAM” in comparison between the experimental measurements from Taylor-Noonan et al. (2022) (dashed lines) and the simulated results (solid lines) for (a) the dry grains and (b) the initially water-saturated grain mixture, each with an initial volume of  $0.4 \text{ m}^3$ . The initial geometries and the position of the camera (“CAM”) are shown in the insets of both panels. The free surface of the dry grains is represented by red lines, the surface of the water-saturated grain mixture by black lines.

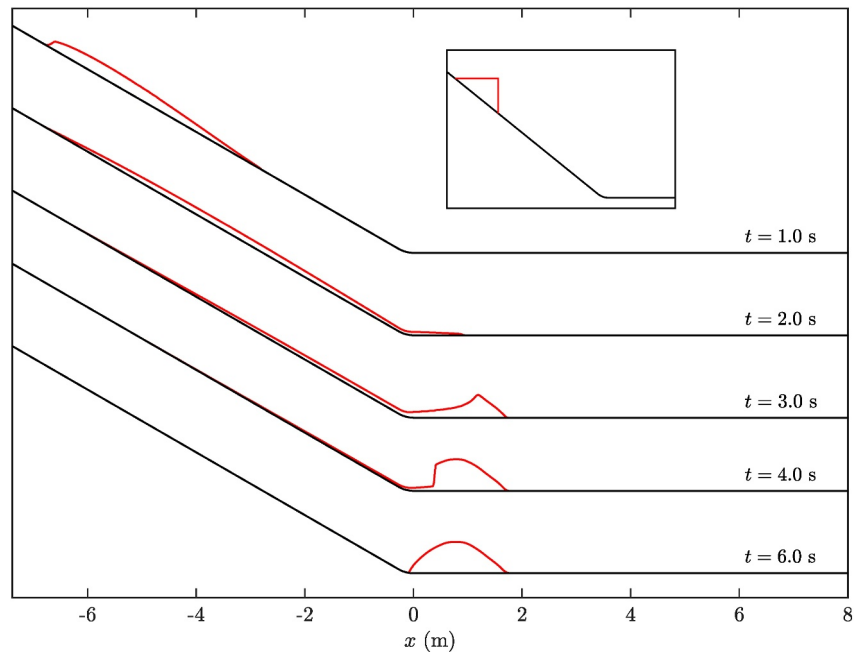


**Figure 9.** Simulated temporal and spatial evolution of the free surface of the dry grains with an initial volume of  $0.4 \text{ m}^3$  sliding down a slope with an inclination angle of  $30^\circ$ , transitioning to a horizontal plane. The flow thickness is magnified three times for a better visualization. The initial geometry of the dry grains is shown in the inset.

To provide a comprehensive overview of the dynamic flows, we present the simulated temporal and spatial evolution of flow heights for both the dry grains and the initially water-saturated grain mixture, each with an initial volume of  $0.4 \text{ m}^3$ , as shown in Figures 9 and 10. Figure 9 shows the downhill motion of the dry grains as they are released. At the onset of flow, the dry grains accelerate downward due to gravity and spread rapidly due to their non-uniform height, hence the gradient of the depth-averaged internal pressure (represented by the term  $\frac{1}{2}(h^g)^2\phi^g g \cos \zeta$  in the depth-averaged Equation 67). At  $t = 2.0 \text{ s}$ , the flow is fully developed and becomes elongated on the slope. At this time, the dry grain front reaches the horizontal plate, where the  $h^g\phi^g g \sin \zeta$  component of the gravitational acceleration becomes zero, and the grains begin to decelerate due to granular friction. By  $t = 3.0 \text{ s}$ , the flow front is deposited, and the following mass rapidly comes to rest, causing a shock wave that propagates upstream, clearly observable at  $t = 4.0 \text{ s}$ . At  $t = 6.0 \text{ s}$ , the entire dry grain flow has deposited on the horizontal plate. This flow process is very similar to the simulated results of Meng et al. (2024) (see their Figure 7).

For the initially water-saturated grain mixture, as shown in Figure 10, the flow transitions from an initially water-saturated mixture regime to an under-saturated mixture regime due to the granular dilatancy effect. The grains in the initially water-saturated mixture are initially densely packed and dilute as they flow down the slope, causing some grains to cross the water interface. This results in the formation of a pure grain upper layer overlying the water-saturated mixture lower layer. Although the presence of interstitial water reduces the basal granular friction due to buoyancy, the grains in the saturated mixture accelerate down the slope and have a high shear rate, resulting in a relatively large positive granular dilatancy angle, which increases the basal granular friction. Therefore, at the beginning of the flow, the difference in run-out distances between the initially water-saturated mixture and the dry grains is not significant. The flow front gradually evolves from an under-saturated mixture to a pure grain front, which is observed at  $t = 2.0 \text{ s}$ , and by this time, more of the flow mass has reached the horizontal plate compared to the dry grains.

At  $t = 3.0 \text{ s}$ , the main flow mass moves on the horizontal plate. The grains decelerate and the granular shear rate decreases. At this point, the granular dilatancy angle decreases as the grains compact. The effect of the buoyancy force of the interstitial water, which reduces the basal granular friction, becomes more significant. This causes the flow mass to travel further, resulting in a longer run-out distance compared to the dry grains. As the grains slow down, the interstitial water continues to move forward due to its low fluid friction, causing the flow front to

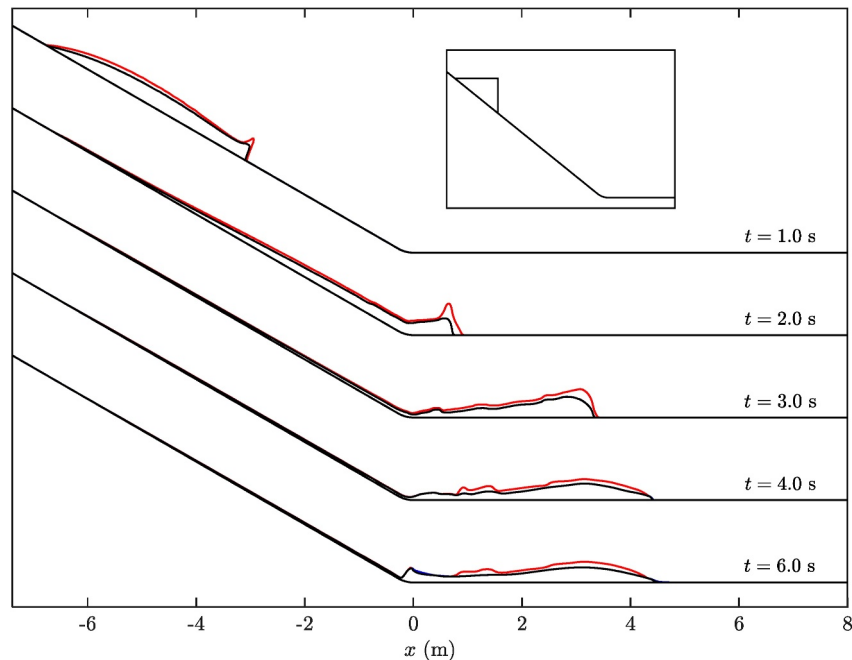


**Figure 10.** Simulated temporal and spatial evolution of the surface of the initially water-saturated grain mixture with an initial volume of  $0.4 \text{ m}^3$  sliding down a slope with an inclination angle of  $30^\circ$ , transitioning to a horizontal plane. The flow thickness is magnified five times for better visualization. The red solid lines indicate the free surface of the pure grains and the black solid lines represent the surface of the water-saturated mixture. At  $t = 6.0 \text{ s}$ , the almost invisible blue solid line at the front and tail of the flow represents the surface of the flowing-out water. The initial geometry of the initially water-saturated grain mixture is shown in the inset.

transition from pure grains back to an under-saturated mixture. At  $t = 4.0 \text{ s}$ , the grains at the flow front come to rest, while the interstitial water continues to move and even slowly percolates through the grains at the front by  $t = 6.0 \text{ s}$ . As a result, the flow front becomes a water-saturated, or even over-saturated, mixture. Meanwhile, the grains at the flow tail compact and a very small amount of interstitial water is extruded from the saturated mixture at the flow tail.

#### 4.4. Saturated Grain-Fluid Mixtures in a Rotating Drum

Leonardi et al. (2015) conducted experiments on initially saturated grain-fluid mixtures in a rotating drum. In their experiments, the material consists of spherical ceramic particles with a visco-plastic fluid. It was observed that the state of the granular flow front is affected by the rotating velocity  $\omega$  of the drum, that is, at low drum speeds, the front of the grain-fluid mixture exhibits an over-saturated state, while at high drum speeds it manifests as an under-saturated mixture flow at the front. To illustrate the ability of our depth-averaged model to capture such phenomena of granular-fluid phase separation, we numerically simulate here such initially saturated grain-fluid mixtures flowing in a rotating drum. However, it should be noted that the particle diameter used in their experiments was  $d = 32.6 \text{ mm}$ , which surpasses the requirement for the assumption of a continuous medium in the present theoretical framework. Additionally, the interstitial fluid in the experiments is a non-Newtonian fluid, approximated as a Bingham fluid, while our current model does not include the Bingham fluid model. These discrepancies could potentially result in significant differences between the numerical and experimental results. Hence, in this section, we present only qualitative simulated results, but no quantitative comparison.

In the numerical simulations, an initially static saturated grain-fluid mixture is released in a drum of radius  $r = 4.75 \text{ m}$ , which is rotated at two different angular speeds, respectively,  $\omega = 0.01 \text{ rad/s}$  for low speed and  $\omega = 0.1 \text{ rad/s}$  for high speed. It is worth noting that the steady-state solution is independent of the initial configuration of the saturated fluid-grain mixture (see e.g. Meng et al., 2018). In our numerical simulations, we use the intrinsic densities of particles and fluid from the experiment by Leonardi et al. (2015), specifically  $\rho^{s*} = 2420 \text{ kg/m}^3$  and  $\rho^{f*} = 1420 \text{ kg/m}^3$ . However, we define the other physical parameters in the following

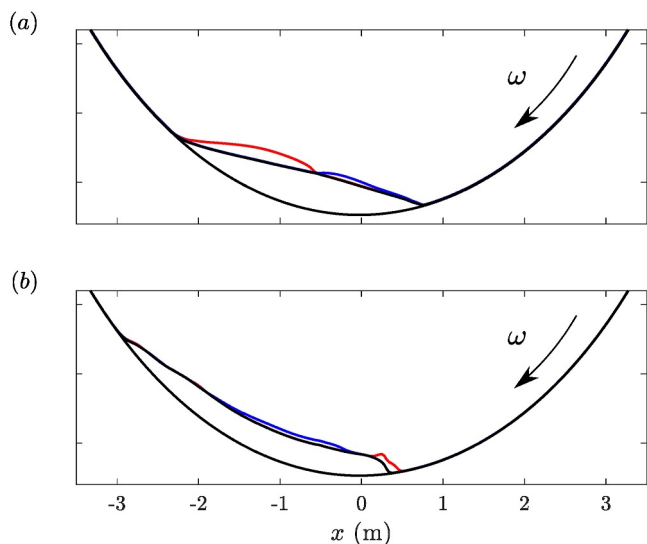


**Figure 11.** Simulated profiles of a grain-fluid mixture flow in a rotating drum, respectively, with two different angular speeds: (a)  $\omega = 0.01$  rad/s and (b)  $\omega = 0.1$  rad/s. The red lines indicate the surface profiles of the pure grains, the blue lines show the surface profiles of the pure fluid, and the black lines represent the surface profiles of the water-saturated grains.

ourselves, as this is not about a quantitative comparison. The particle diameter is  $d = 6$  mm, and the initial granular volume fraction in the saturated grain-fluid mixture is  $\phi^s = 0.6$ . The viscosity of the interstitial fluid is set to  $\eta^f = 0.01$  Pa·s. The granular friction coefficients for the  $\mu(I)$  and  $\mu(I_v)$  rheology, along with the parameters for granular dilatancy effects, are used as outlined in Table 2.

Figure 11 illustrates the simulated profiles of the grain-fluid mixture flows at the steady state in the rotating drum. At a low drum rotation speed of  $\omega = 0.01$  rad/s, the initially saturated grain-fluid mixture results in an over-saturated front and an under-saturated rear, as depicted in Figure 11a. Conversely, at a high drum rotation speed of  $\omega = 0.1$  rad/s, the front of the flow exhibits an under-saturated mixture, while the middle of the flow contains an over-saturated mixture, as shown in Figure 11b. The flow profile at the high drum speed is longer and thinner compared to that at the lower drum speed. These results demonstrate that our numerical simulations can qualitatively capture the experimental findings reported by Leonardi et al. (2015).

## 5. Conclusion

In this work, we have proposed a two-layer depth-averaged model with granular dilatancy effects to study the dynamics of grain-fluid mixture flows. In contrast to single-medium flows, such as pure grain or pure fluid flows, grain-fluid mixtures involve interactions between the granular and fluid

phases. Another important feature of these flows is the phase separation between grains and fluid during the motion, which leads to the emergence, transition and even disappearance of different flow regimes, including the pure grain regime, the pure fluid regime, the saturated grain-fluid mixture regime, and the under-saturated and over-saturated mixture regimes. Various studies have proposed different depth-averaged models for only one of these flow regimes. Several representative depth-averaged models used for different flow regimes are listed in Table 1. In our work, we have improved the previous depth-averaged models, which are only suitable for a single regime, and then integrated them to describe grain-fluid mixture flows, including all flow regimes that may occur, simultaneously.

We started our study with a comprehensive mixture theory for saturated grain-fluid mixtures and established the mass and momentum balance equations for the granular and fluid phases. In addition, the single-phase balance equations for pure grain and pure fluid regimes were presented, which can also be obtained by simplifying the balance equations for saturated mixtures. By depth integration of these equations, together with the application of appropriate boundary conditions and jump conditions, if any, we formulated the two-phase two-layer depth-averaged models for the under-saturated and over-saturated grain-fluid mixture regimes and the single-layer depth-averaged models for the pure grain, pure fluid and saturated grain-fluid mixture regimes. When applying the model to simulate real events, the inclusion of curvature effects is essential (Bouchut & Westdickenberg, 2004; Peruzzetto et al., 2021). In the present study, our model only considers a topography curvature in the downslope direction, but not complex topography.

In particular, we used the boundary conditions of Meng et al. (2017) for the under-saturated mixture regime, while for the over-saturated mixture regime, the boundary conditions of Luca et al. (2012) were employed. However, in contrast to these studies, our models considered granular dilatancy effects and excess pore fluid pressure in the saturated mixture region. The depth-averaged model presented for the over-saturated mixture regime shares some similarities with the model proposed by Bouchut et al. (2016), which also used a two-layer two-phase structure and included granular dilatancy effects. However, there are some differences between the two models. The dynamic boundary conditions at the interface between the layers, the friction conditions of the fluid, and the modeling of the excess pore fluid pressure differ between the two models. As a result, several terms in the depth-averaged models differ, for example, momentum transfer, fluid friction at the interface and at the bottom, and phase-by-phase interaction. In addition, the interfacial friction force exerted by the pure fluid upper layer on the solid phase in the lower layer mixture was neglected in their model. Moreover, in contrast to the two-layer structure of the depth-averaged models proposed for under-saturated and over-saturated mixture regimes,

Meng et al. (2022) developed a two-phase but single-layer depth-averaged model with a single set of equations for all flow regimes to study different flow regimes in grain-fluid mixture flows, neglecting the different behaviors of the pure fluid and the fluid phase in a grain-fluid mixture or the pure grains and the granular phase in a grain-fluid mixture. Based on their simple system of equations with a special velocity profile over the flow depth, they computed an analytical solution for the small-scale moving bed experiments of Davies (1990) and showed that their solutions quantitatively agreed well with the experiments at high bed velocities and slopes. However, the assumption of a constant volume fraction throughout the granular phase in their model precludes consideration of the excess pore fluid pressure, and their model could not independently describe the dynamics of the upper layer of single medium and the lower layer of the saturated mixture due to its single-layer structure. Moreover, a single granular rheology was used to characterize granular friction in all these studies mentioned above. In our study, we used the  $\mu(I)$  rheology for the pure granular region and the  $\mu(I_v)$  rheology for the saturated grain-fluid mixture region to describe the different frictional behavior of the grains in different states.

In our study, the presented sets of depth-averaged models for the different flow regimes were solved numerically simultaneously using a high-resolution central-upwind scheme. This simultaneous numerical simulation of the different depth-averaged models in different regimes posed a challenge. To overcome this, we incorporated a special assessment criteria into our numerical implementation to determine which flow regime is occurring in each computational cell at each time step. The numerical treatment of the flux, source, non-conservative, and friction terms for the transitions between the different flow regimes is detailed in the numerical method section. The physical introduction of granular or fluid mass and momentum transfer across the interface between the layers in the under-saturated or over-saturated mixture regimes brings the positive side effect of exempting the multi-layer model from possible ill-posedness and ensuring the stability of our numerical simulations. Furthermore, we have applied an operator-splitting method to our semi-discrete ordinary differential equations for the numerical treatment of the granular friction terms.

To demonstrate the robustness of the numerical treatment and to evaluate the performance of the presented model, we compared the simulated results with several experimental studies, including the collapse of an initially saturated granular column in air by Ceccato et al. (2020), the collapses of dry and partially immersed granular columns by He et al. (2022), and the landslides of dry grains and initially saturated water-grain mixtures by Taylor-Noonan et al. (2022). It is important to emphasize that most material parameters used in our numerical simulations were provided by the corresponding experiments. Although some parameters in our numerical simulations, such as the granular friction coefficients in the  $\mu(I)$  and  $\mu(I_v)$  rheologies, were not explicitly specified in the experiments, we chose these parameters wisely within a reasonable range based on other similar numerical studies. We have not fitted any parameters to achieve a qualitatively good agreement with the experimental data. During the simulation of the subaerial collapse of an initially saturated granular column, our model can describe the process of phase separation in grain-fluid mixture flows. In particular, fluid leaked from the saturated mixture at the front of the flow, and the main part of the flow transformed from an initially saturated mixture into an under-saturated mixture. However, at the beginning of the collapse, our numerical simulation showed higher velocities than the experiments. This initial discrepancy is attributed to the inherent tendency of depth-averaged models to overestimate the flow velocity in the initial phase, as demonstrated in several previous studies (Bouchut et al., 2017; Mangeney-Castelnau et al., 2005). The simulations performed on experiments with partially submerged granular columns showed remarkable effects of interstitial fluid on the flow dynamics of partially saturated mixtures with different particle sizes. In particular, the presence of interstitial water increases the mobility of the saturated mixture in the partially submerged granular column with coarse particles compared to that with fine particles. These phenomena could only be reproduced if the effects of granule dilatancy and excess pore fluid pressure were taken into account. Furthermore, different from Meng et al. (2022), who introduced shear in their model to capture an under-saturated flow front of grain-fluid mixtures, our numerical simulation of the landslide of the initially water-saturated grain mixture qualitatively describes the transition from an initially water-saturated mixture to an under-saturated mixture during flow through granular mass transfer induced by the dilatancy effects of the particles. The initially water-saturated grain mixture has a longer run-out distance compared to dry grains due to the effect of interstitial water, which is consistent with the experimental observations of Taylor-Noonan et al. (2022). During the deposition stage, a small amount of water flows out at both the front and rear of the flow. In addition, our simulation of the saturated grain-fluid mixture in a rotating drum provided a qualitative description of the influence of the rotation speed of the drum on the formation of the

under-saturated or over-saturated flow front, which is consistent with the findings reported by Leonardi et al. (2015).

In summary, this study attempts to use a two-layer two-phase depth-averaged model to simultaneously describe the dynamic behavior of different flow regimes that can occur during the flow of grain-fluid mixtures. Our Simulations demonstrate that the two-layer structural model, which incorporates the granular dilatancy effects and the different granular frictional rheologies, can qualitatively describe the flow behavior of grain-fluid mixtures. In the future, this research should be applied to the investigation of real debris flows to test its effectiveness.

### Appendix A: Nondimensional Equations for the Under-Saturated Mixture Regime in the Terrain-Following Coordinate System

In this appendix, the nondimensional forms of the governing Equations 1, 8 and 9 for the saturated mixture, and the governing Equations 10 and 11 for the pure grains are presented. Additionally, we include the nondimensional forms of the boundary conditions (19)–(32). To highlight important quantities, scaling is necessary. Following the methodologies of Gray et al. (1999) and Sun et al. (2023), the scaling is presented by the following equation:

$$\left. \begin{aligned} (x, z, \xi^s, \xi^i, b) &= L(\hat{x}, \varepsilon \hat{z}, \varepsilon \hat{\xi}^s, \varepsilon \hat{\xi}^i, \varepsilon \hat{b}), \quad t = (L/g)^{1/2} \hat{t}, \\ (u^\nu, w^\nu, |\mathbf{u}^\nu|) &= (gL)^{1/2} (\hat{u}^\nu, \varepsilon \hat{w}^\nu, |\hat{\mathbf{u}}^\nu|), \quad \nu = g, pf, sf, \\ (\sigma_{xx}^e, \sigma_{xz}^e, \sigma_{zz}^e) &= \varrho^{s*} g H (\hat{\sigma}_{xx}^e, \mu \hat{\sigma}_{xz}^e, \hat{\sigma}_{zz}^e), \\ (p^{f*}, \tau_{xx}^f, \tau_{xz}^f, \tau_{zz}^f) &= \varrho^{f*} g H (\hat{p}^{f*}, \varepsilon \hat{\tau}_{xx}^f, \hat{\tau}_{xz}^f, \varepsilon \hat{\tau}_{zz}^f), \quad \kappa = \hat{\kappa}/R, \\ C^d &= \varrho^{f*} (g/L)^{1/2} \hat{C}^d, \quad M^s = \varepsilon \varrho^{s*} (gL)^{1/2} \hat{M}^s. \end{aligned} \right\} \quad (A1)$$

where the hats represent nondimensional variables. In the present study, we assume that the typical flow thickness  $H$  is much smaller than the typical flow length  $L$ , and hence the aspect ratio  $\varepsilon = H/L \ll 1$ . The curvature of the basal reference surface is defined as  $\kappa = -d\zeta/dx$ , and the scaling of the curvature is  $1/R$ , where  $R$  is the characteristic radius of curvature of the basal topography. Additionally, it requires a slowly varying basal topography, meaning that the characteristic radius of curvature of the basal topography  $R$ , is much larger than the typical flow length  $L$ , that is,  $L/R \ll 1$ .

The nondimensional form of the mass balance equation for the pure grains Equation 10 is given by:

$$\frac{\partial \phi^g}{\partial \hat{t}} + \frac{\partial}{\partial \hat{x}} (\phi^g \hat{u}^g \Psi) + \frac{\partial}{\partial \hat{z}} (\phi^g \hat{w}^g) - \varepsilon \lambda \hat{\kappa}' \hat{z} \phi^g \hat{u}^g \Psi^2 - \varepsilon \lambda \hat{\kappa} \phi^g \hat{w}^g \Psi = 0, \quad (A2)$$

where the nondimensional parameters  $\lambda$  and  $\Psi$  associated with the curvilinear coordinate system arise, given by the following equation:

$$\lambda = L/R, \quad \Psi = 1/(1 - \varepsilon \lambda \hat{\kappa} \hat{z}). \quad (A3)$$

The nondimensional downslope and normal components of the momentum balance Equation 11 are given as follows:

$$\begin{aligned} \frac{\partial}{\partial \hat{t}} (\phi^g \hat{u}^g) + \frac{\partial}{\partial \hat{x}} (\phi^g (\hat{u}^g)^2 \Psi) + \frac{\partial}{\partial \hat{z}} (\phi^g \hat{u}^g \hat{w}^g) - \varepsilon \lambda \hat{\kappa}' \hat{z} \phi^g (\hat{u}^g)^2 \Psi^2 - 2 \varepsilon \lambda \hat{\kappa} \phi^g \hat{u}^g \hat{w}^g \Psi &= \phi^g \sin \zeta \\ - \varepsilon \frac{\partial}{\partial \hat{x}} (\hat{\sigma}_{xx}^e \Psi) - \mu \frac{\partial \hat{\sigma}_{xz}^e}{\partial \hat{z}} + \varepsilon^2 \lambda \hat{\kappa}' \hat{z} \hat{\sigma}_{xx}^e \Psi^2 + 2 \varepsilon \lambda \hat{\kappa} \mu \hat{\sigma}_{xz}^e \Psi, \end{aligned} \quad (A4)$$

$$\begin{aligned} \varepsilon \left( \frac{\partial}{\partial \hat{t}} (\phi^g \hat{w}^g) + \frac{\partial}{\partial \hat{x}} (\phi^g \hat{u}^g \hat{w}^g \Psi) + \frac{\partial}{\partial \hat{z}} (\phi^g (\hat{w}^g)^2) \right) - \varepsilon^2 \lambda \hat{\kappa}' \hat{z} \phi^g \hat{u}^g \hat{w}^g \Psi^2 - \varepsilon^2 \lambda \hat{\kappa} \phi^g (\hat{w}^g)^2 \Psi \\ + \lambda \hat{\kappa} \phi^g (\hat{u}^g)^2 \Psi = -\phi^g \cos \zeta - \varepsilon \mu \frac{\partial}{\partial \hat{x}} (\hat{\sigma}_{xz}^e \Psi) - \frac{\partial \hat{\sigma}_{zz}^e}{\partial \hat{z}} + \varepsilon^2 \lambda \hat{\kappa}' \hat{z} \mu \hat{\sigma}_{xz}^e \Psi^2 + \varepsilon \lambda \hat{\kappa} (\hat{\sigma}_{zz}^e - \hat{\sigma}_{xx}^e) \Psi. \end{aligned} \quad (A5)$$

The nondimensional form of the mass balance Equation 1 for the solid phase of the saturated mixture is as follows:

$$\frac{\partial \phi^s}{\partial \hat{t}} + \frac{\partial}{\partial \hat{x}}(\phi^s \hat{u}^s \Psi) + \frac{\partial}{\partial \hat{z}}(\phi^s \hat{w}^s) - \varepsilon \lambda \hat{\kappa}' \hat{z} \phi^s \hat{u}^s \Psi^2 - \varepsilon \lambda \hat{\kappa} \phi^s \hat{w}^s \Psi = 0, \quad (\text{A6})$$

and the nondimensional downslope and normal components of the momentum balance Equation 8 for the solid phase of the saturated mixture are given as follows:

$$\begin{aligned} & \frac{\partial}{\partial \hat{t}}(\phi^s \hat{u}^s) + \frac{\partial}{\partial \hat{x}}(\phi^s (\hat{u}^s)^2 \Psi) + \frac{\partial}{\partial \hat{z}}(\phi^s \hat{u}^s \hat{w}^s) - \varepsilon \lambda \hat{\kappa}' \hat{z} \phi^s (\hat{u}^s)^2 \Psi^2 - 2\varepsilon \lambda \hat{\kappa} \phi^s \hat{u}^s \hat{w}^s \Psi = \phi^s \sin \zeta \\ & - \varepsilon \frac{\partial}{\partial \hat{x}}(\hat{\sigma}_{xx}^e \Psi) - \varepsilon \gamma \phi^s \frac{\partial}{\partial \hat{x}}(\hat{p}^{f*} \Psi) - \mu \frac{\partial \hat{\sigma}_{xz}^e}{\partial \hat{z}} + \varepsilon^2 \lambda \hat{\kappa}' \hat{z} \hat{\sigma}_{xx}^e \Psi^2 + 2\varepsilon \lambda \hat{\kappa} \mu \hat{\sigma}_{xz}^e \Psi + \gamma \hat{C}^d (\hat{u}^f - \hat{u}^s), \end{aligned} \quad (\text{A7})$$

$$\begin{aligned} & \varepsilon \left( \frac{\partial}{\partial \hat{t}}(\phi^s \hat{w}^s) + \frac{\partial}{\partial \hat{x}}(\phi^s \hat{u}^s \hat{w}^s \Psi) + \frac{\partial}{\partial \hat{z}}(\phi^s (\hat{w}^s)^2) \right) - \varepsilon^2 \lambda \hat{\kappa}' \hat{z} \phi^s \hat{u}^s \hat{w}^s \Psi^2 - \varepsilon^2 \lambda \hat{\kappa} \phi^s (\hat{w}^s)^2 \Psi \\ & + \lambda \hat{\kappa} \phi^s (\hat{u}^s)^2 \Psi = -\phi^s \cos \zeta - \varepsilon \mu \frac{\partial}{\partial \hat{x}}(\hat{\sigma}_{xz}^e \Psi) - \frac{\partial \hat{\sigma}_{zz}^e}{\partial \hat{z}} - \gamma \phi^s \frac{\partial \hat{p}^{f*}}{\partial \hat{z}} + \varepsilon^2 \lambda \hat{\kappa}' \hat{z} \mu \hat{\sigma}_{xz}^e \Psi^2 \\ & + \varepsilon \lambda \hat{\kappa} (\hat{\sigma}_{zz}^e - \hat{\sigma}_{xx}^e) \Psi + \varepsilon \gamma \hat{C}^d (\hat{w}^f - \hat{w}^s), \end{aligned} \quad (\text{A8})$$

where  $\gamma = \rho^{f*}/\rho^{s*}$ , represents the intrinsic density ratio between the fluid and grains.

The nondimensional form of the mass balance Equation 1 for the fluid phase of the saturated mixture is as follows:

$$\frac{\partial \phi^f}{\partial \hat{t}} + \frac{\partial}{\partial \hat{x}}(\phi^f \hat{u}^f \Psi) + \frac{\partial}{\partial \hat{z}}(\phi^f \hat{w}^f) - \varepsilon \lambda \hat{\kappa}' \hat{z} \phi^f \hat{u}^f \Psi^2 - \varepsilon \lambda \hat{\kappa} \phi^f \hat{w}^f \Psi = 0, \quad (\text{A9})$$

and the nondimensional downslope and normal components of the momentum balance Equation 9 for the fluid phase of the saturated mixture are as follows:

$$\begin{aligned} & \frac{\partial}{\partial \hat{t}}(\phi^f \hat{u}^f) + \frac{\partial}{\partial \hat{x}}(\phi^f (\hat{u}^f)^2 \Psi) + \frac{\partial}{\partial \hat{z}}(\phi^f \hat{u}^f \hat{w}^f) - \varepsilon \lambda \hat{\kappa}' \hat{z} \phi^f (\hat{u}^f)^2 \Psi^2 - 2\varepsilon \lambda \hat{\kappa} \phi^f \hat{u}^f \hat{w}^f \Psi = \phi^f \sin \zeta \\ & + \varepsilon^2 \frac{\partial}{\partial \hat{x}}(\hat{\tau}_{xx}^f \Psi) - \varepsilon \phi^f \frac{\partial}{\partial \hat{x}}(\hat{p}^{f*} \Psi) + \frac{\partial \hat{\tau}_{xz}^f}{\partial \hat{z}} - \varepsilon^3 \lambda \hat{\kappa}' \hat{z} \hat{\tau}_{xx}^f \Psi^2 - 2\varepsilon \lambda \hat{\kappa} \hat{\tau}_{xz}^f \Psi - \hat{C}^d (\hat{u}^f - \hat{u}^s), \end{aligned} \quad (\text{A10})$$

$$\begin{aligned} & \varepsilon \left( \frac{\partial}{\partial \hat{t}}(\phi^f \hat{w}^f) + \frac{\partial}{\partial \hat{x}}(\phi^f \hat{u}^f \hat{w}^f \Psi) + \frac{\partial}{\partial \hat{z}}(\phi^f (\hat{w}^f)^2) \right) - \varepsilon^2 \lambda \hat{\kappa}' \hat{z} \phi^f \hat{u}^f \hat{w}^f \Psi^2 - \varepsilon^2 \lambda \hat{\kappa} \phi^f (\hat{w}^f)^2 \Psi \\ & + \lambda \hat{\kappa} \phi^f (\hat{u}^f)^2 \Psi = -\phi^f \cos \zeta + \varepsilon \frac{\partial}{\partial \hat{x}}(\hat{\tau}_{xz}^f \Psi) + \varepsilon \frac{\partial \hat{\tau}_{zz}^f}{\partial \hat{z}} - \phi^f \frac{\partial \hat{p}^{f*}}{\partial \hat{z}} - \varepsilon^2 \lambda \hat{\kappa}' \hat{z} \hat{\tau}_{xz}^f \Psi^2 \\ & - \varepsilon^2 \lambda \hat{\kappa} (\hat{\tau}_{zz}^f - \hat{\tau}_{xx}^f) \Psi - \varepsilon \hat{C}^d (\hat{w}^f - \hat{w}^s). \end{aligned} \quad (\text{A11})$$

The nondimensional forms of the kinematic boundary conditions on the grain free surface Equation 19, the interface Equation 27, and the bottom Equations 20 and 24 are given as follows:

$$\left. \begin{aligned} & \frac{\partial \hat{\xi}^s}{\partial \hat{t}} + \hat{u}^s \Psi \frac{\partial \hat{\xi}^s}{\partial \hat{x}} - \hat{w}^s = 0, & \hat{z} &= \hat{\xi}^s(\hat{x}, \hat{t}), \\ & \frac{\partial \hat{\xi}^i}{\partial \hat{t}} + \hat{u}^f \Psi \frac{\partial \hat{\xi}^i}{\partial \hat{x}} - \hat{w}^f = 0, & \hat{z} &= \hat{\xi}^i(\hat{x}, \hat{t}), \\ & \hat{u}^s \Psi \frac{\partial \hat{b}}{\partial \hat{x}} - \hat{w}^s = 0, & \hat{z} &= \hat{b}(\hat{x}), \\ & \hat{u}^f \Psi \frac{\partial \hat{b}}{\partial \hat{x}} - \hat{w}^f = 0, & \hat{z} &= \hat{b}(\hat{x}). \end{aligned} \right\} \quad (\text{A12a-d})$$

On the free surface of the upper layer of pure grains, the nondimensional downslope and normal components of the traction free boundary condition (Equation 21) are as follows:

$$\left. \begin{aligned} -\varepsilon \hat{\sigma}_{xx}^e \Psi \frac{\partial \hat{\xi}^s}{\partial \hat{x}} + \mu \hat{\sigma}_{xz}^e &= 0, & \hat{z} &= \hat{\xi}^s(\hat{x}, \hat{t}), \\ -\varepsilon \mu \hat{\sigma}_{xz}^e \Psi \frac{\partial \hat{\xi}^s}{\partial \hat{x}} + \hat{\sigma}_{zz}^e &= 0, & \hat{z} &= \hat{\xi}^s(\hat{x}, \hat{t}). \end{aligned} \right\} \quad (\text{A13a-b})$$

On the bottom, the nondimensional downslope and normal components of the friction conditions Equation 22 for the solid phase and Equation 26 for the fluid phase of the lower layer of mixture are given as follows:

$$\left. \begin{aligned} -\varepsilon \hat{\sigma}_{xx}^e \Psi \frac{\partial \hat{b}}{\partial \hat{x}} + \mu \hat{\sigma}_{xz}^e &= -\left( \varepsilon \Psi \frac{\partial \hat{b}}{\partial \hat{x}} + |\nabla F^b| \mu^b \frac{\hat{u}_b^s}{|\hat{u}_b^s|} \right) (\mathbf{n}^b \cdot \hat{\boldsymbol{\sigma}}^e \mathbf{n}^b), \\ -\varepsilon \mu \hat{\sigma}_{xz}^e \Psi \frac{\partial \hat{b}}{\partial \hat{x}} + \hat{\sigma}_{zz}^e &= \left( 1 - \varepsilon |\nabla F^b| \frac{\hat{w}_b^s}{|\hat{u}_b^s|} \right) (\mathbf{n}^b \cdot \hat{\boldsymbol{\sigma}}^e \mathbf{n}^b), \end{aligned} \right\} \quad (\text{A14a-b})$$

$$\left. \begin{aligned} \varepsilon \phi^f \hat{p}^{f*} \Psi \frac{\partial \hat{b}}{\partial \hat{x}} - \varepsilon^2 \hat{\tau}_{xx}^f \Psi \frac{\partial \hat{b}}{\partial \hat{x}} + \hat{\tau}_{xz}^f &= -\varepsilon (\mathbf{n}^b \cdot \hat{\boldsymbol{\sigma}}^f \mathbf{n}^b) \Psi \frac{\partial \hat{b}}{\partial \hat{x}} + |\nabla \hat{F}^b| C^f |\bar{\mathbf{u}}^f| |\bar{\mathbf{u}}^f|, \\ -\varepsilon \hat{\tau}_{xz}^f \Psi \frac{\partial \hat{b}}{\partial \hat{x}} - \phi^f \hat{p}^{f*} + \varepsilon \hat{\tau}_{zz}^f &= (\mathbf{n}^b \cdot \hat{\boldsymbol{\sigma}}^f \mathbf{n}^b) + \varepsilon |\nabla \hat{F}^b| C^f |\bar{\mathbf{w}}^f| |\bar{\mathbf{w}}^f|, \end{aligned} \right\} \quad (\text{A15a-b})$$

respectively, where  $|\hat{\mathbf{u}}_b^s| = \sqrt{(\hat{u}_b^s)^2 + \varepsilon (\hat{w}_b^s)^2}$  and  $|\nabla \hat{F}^b| = \sqrt{(\varepsilon \Psi (\partial \hat{b} / \partial \hat{x}))^2 + 1}$ .

In the under-saturated mixture regime, the interface between layers is a material surface of the fluid phase of the mixture. Across this interface, a mass transfer of grains can occur. On this interface, the nondimensional granular mass transfer (29) is as follows:

$$\hat{M}^s = -\frac{1}{|\nabla \hat{F}^f|} \phi^g \left( \frac{\partial \hat{\xi}^i}{\partial \hat{t}} + \hat{u}^g \Psi \frac{\partial \hat{\xi}^i}{\partial \hat{x}} - \hat{w}^g \right) = -\frac{1}{|\nabla \hat{F}^f|} \phi^s \left( \frac{\partial \hat{\xi}^i}{\partial \hat{t}} + \hat{u}^s \Psi \frac{\partial \hat{\xi}^i}{\partial \hat{x}} - \hat{w}^s \right), \quad (\text{A16})$$

where  $|\nabla \hat{F}^f| = \sqrt{(\varepsilon \Psi (\partial \hat{\xi}^i / \partial \hat{x}))^2 + 1}$ .

On the interface, the nondimensional downslope and normal components of the momentum conditions (30) for the fluid phase and (31) for the solid phase of the lower layer of the mixture are given as follows:

$$\left. \begin{aligned} \varepsilon \phi^f \hat{p}^{f*} \Psi \frac{\partial \hat{\xi}^i}{\partial \hat{x}} - \varepsilon^2 \hat{\tau}_{xx}^f \Psi \frac{\partial \hat{\xi}^i}{\partial \hat{x}} + \hat{\tau}_{xz}^f &= 0, \\ -\varepsilon \hat{\tau}_{xz}^f \Psi \frac{\partial \hat{\xi}^i}{\partial \hat{x}} - \phi^f \hat{p}^{f*} + \varepsilon \hat{\tau}_{zz}^f &= 0, \end{aligned} \right\} \quad (\text{A17a-b})$$

$$\left. \begin{aligned} -\varepsilon \hat{\sigma}_{xx}^{e-} \Psi \frac{\partial \hat{\xi}^i}{\partial \hat{x}} + \mu \hat{\sigma}_{xz}^{e-} &= -\varepsilon \hat{\sigma}_{xx}^{e+} \Psi \frac{\partial \hat{\xi}^i}{\partial \hat{x}} + \mu \hat{\sigma}_{xz}^{e+} + \hat{M}^s (\hat{u}^g - \hat{u}^s), \\ -\varepsilon \mu \hat{\sigma}_{xz}^{e-} \Psi \frac{\partial \hat{\xi}^i}{\partial \hat{x}} + \hat{\sigma}_{zz}^{e-} &= -\varepsilon \mu \hat{\sigma}_{xz}^{e+} \Psi \frac{\partial \hat{\xi}^i}{\partial \hat{x}} + \hat{\sigma}_{zz}^{e+} + \varepsilon \hat{M}^s (\hat{w}^g - \hat{w}^s), \end{aligned} \right\} \quad (\text{A18a-b})$$

respectively, where  $\hat{\boldsymbol{\sigma}}^{e+}$  and  $\hat{\boldsymbol{\sigma}}^{e-}$  represent the solid effective stresses of the upper and the lower layer of grains materials, respectively.

Additionally, on the interface, the nondimensional downslope and normal components of the friction conditions (32) for the solid phase of the lower layer of mixture are as follows:

$$\left. \begin{aligned} -\varepsilon \hat{\sigma}_{xx}^{e-} \Psi \frac{\partial \hat{\xi}^i}{\partial \hat{x}} + \mu \hat{\sigma}_{xz}^{e-} &= \left( -\varepsilon \Psi \frac{\partial \hat{\xi}^i}{\partial \hat{x}} + |\nabla F^i| \mu^i \frac{\hat{u}^s - \hat{u}^g}{|\hat{u}^s - \hat{u}^g|} \right) (\mathbf{n}^i \cdot \hat{\sigma}^e \mathbf{n}^i), \\ -\varepsilon \mu \hat{\sigma}_{xz}^{e-} \Psi \frac{\partial \hat{\xi}^i}{\partial \hat{x}} + \hat{\sigma}_{zz}^{e-} &= \left( 1 + \varepsilon |\nabla F^i| \frac{\hat{w}^s - \hat{w}^g}{|\hat{u}^s - \hat{u}^g|} \right) (\mathbf{n}^i \cdot \hat{\sigma}^e \mathbf{n}^i). \end{aligned} \right\} \quad (\text{A19a-b})$$

## Appendix B: The Grain Normal Stress and the Pore Fluid Pressure for the Under-Saturated Mixture Regime

In the present study, we assume that the basal topography varies slowly. Consequently, the parameters  $\lambda$  and  $\Psi$ , and the functions  $|\nabla F^i|$  and  $|\nabla F^b|$ , exhibit magnitudes given by

$$\lambda = O(\varepsilon^\alpha), \quad \Psi = 1 + O(\varepsilon^{1+\alpha}), \quad |\nabla F^i| = 1 + O(\varepsilon^2), \quad |\nabla F^b| = 1 + O(\varepsilon^2), \quad (\text{B1})$$

where  $0 < \alpha < 1$ , as described in Gray et al. (1999) and Sun et al. (2023).

Applying the above ordering of nondimensional parameters, it follows that the normal component of momentum Equation A5 for the upper layer of pure grains is reduced to

$$\frac{\partial \hat{\sigma}_{zz}^e}{\partial \hat{z}} = -\phi^g \cos \zeta - \lambda \hat{\kappa} \phi^g (\hat{u}^g)^2 + O(\varepsilon), \quad \hat{\xi}^i \leq \hat{z} \leq \hat{\xi}^s. \quad (\text{B2})$$

In contrast to the assumption of hydrostatic pore fluid pressure, we take the vertical relative motion between the solid and fluid phases of the lower layer of mixture into account. Consequently, the excess pore fluid pressure is generated by the vertical relative motion, exerting a significant influence on the flow dynamic of the mixture. The normal component of momentum equations (Equation A11) for the fluid phase and (Equation A8) for the solid phase of the mixture reduce to

$$\left. \begin{aligned} -\frac{\partial \hat{p}^{f*}}{\partial \hat{z}} &= \cos \zeta + \varepsilon \hat{C}^d (\hat{w}^f - \hat{w}^s) / \phi^f + \lambda \hat{\kappa} (\hat{u}^f)^2 + O(\varepsilon), \\ -\frac{\partial \hat{\sigma}_{zz}^e}{\partial \hat{z}} &= (1 - \gamma) \phi^s \cos \zeta - \varepsilon \gamma \hat{C}^d (\hat{w}^f - \hat{w}^s) / \phi^f \\ &\quad + \lambda \hat{\kappa} \phi^s \left( (\hat{u}^s)^2 - \gamma (\hat{u}^f)^2 \right) + O(\varepsilon), \end{aligned} \right\} \quad \hat{b} \leq \hat{z} \leq \hat{\xi}^i, \quad (\text{B3a-b})$$

respectively.

The integration of Equation B2 to the grain free surface, alongside the traction-free condition (Equation A13b), yields:

$$\hat{\sigma}_{zz}^e(\hat{z}) = (\hat{\xi}^s - \hat{z}) \phi^g \cos \zeta + (\hat{\xi}^s - \hat{z}) \lambda \hat{\kappa} \phi^g (\hat{u}^g)^2 + O(\varepsilon), \quad \hat{\xi}^i \leq \hat{z} \leq \hat{\xi}^s. \quad (\text{B4})$$

Therefore, on the interface  $\hat{z} = \hat{\xi}^i(\hat{x}, \hat{t})$ , the normal solid effective stress for the upper layer of grains is as follows:

$$\hat{\sigma}_{zz}^e(\hat{\xi}^i) = \hat{h}^g \phi^g \cos \zeta + \lambda \hat{\kappa} \hat{h}^g \phi^g (\hat{u}^g)^2 + O(\varepsilon), \quad \hat{\xi}^i \leq \hat{z} \leq \hat{\xi}^s. \quad (\text{B5})$$

Subsequently, integrating the Equations B3 to the interface, alongside the interface conditions Equations A17b and A18b for the fluid and solid phases of the lower layer of mixture, it follows that:

$$\left. \begin{aligned} \hat{p}_e^{f*}(\hat{z}) &= (\hat{\xi}^i - \hat{z}) \cos \zeta + (\hat{\xi}^i - \hat{z}) \lambda \hat{\kappa} (\hat{u}^f)^2 + \hat{p}_e^{f*} + O(\varepsilon), \\ \hat{\sigma}_{zz}^e(\hat{z}) &= \hat{\sigma}_{zz}^{e+}(\hat{\xi}^i) + (\hat{\xi}^i - \hat{z})(1 - \gamma) \phi^s \cos \zeta - \gamma \hat{p}_e^{f*} \\ &\quad + (\hat{\xi}^i - \hat{z}) \lambda \hat{\kappa} \phi^s \left( (\hat{u}^s)^2 - \gamma (\hat{u}^f)^2 \right) + O(\varepsilon), \end{aligned} \right\} \hat{b} \leq \hat{z} \leq \hat{\xi}^i, \quad (\text{B6a-b})$$

respectively, where the excess pore fluid pressure is defined as follows:

$$\hat{p}_e^{f*} = \int_{\hat{z}}^{\hat{\xi}^i} \varepsilon \hat{C}^d (\hat{w}^f - \hat{w}^s) / \phi^f d\hat{z}. \quad (\text{B7})$$

Substituting Equation B5 into Equation B6b gives the following equation:

$$\begin{aligned} \hat{\sigma}_{zz}^e(\hat{z}) &= \hat{h}^s \phi^s \cos \zeta + \lambda \hat{\kappa} \hat{h}^s \phi^s (\hat{u}^s)^2 + (\hat{\xi}^s - \hat{z})(1 - \gamma) \phi^s \cos \zeta - \gamma \hat{p}_e^{f*} \\ &\quad + (\hat{\xi}^s - \hat{z}) \lambda \hat{\kappa} \phi^s \left( (\hat{u}^s)^2 - \gamma (\hat{u}^f)^2 \right) + O(\varepsilon), \quad \hat{b} \leq \hat{z} \leq \hat{\xi}^i. \end{aligned} \quad (\text{B8})$$

Then, on the bottom, the basal pore fluid pressure and the basal solid effective stress are given as follows:

$$\hat{p}_e^{f*}(\hat{b}) = \hat{h}^m \cos \zeta + \lambda \hat{\kappa} \hat{h}^m (\hat{u}^f)^2 + \int_{\hat{b}}^{\hat{\xi}^i} \varepsilon \hat{C}^d (\hat{w}^f - \hat{w}^s) / \phi^f d\hat{z} + O(\varepsilon), \quad (\text{B9})$$

$$\begin{aligned} \hat{\sigma}_{zz}^e(\hat{b}) &= \hat{h}^s \phi^s \cos \zeta + (1 - \gamma) \hat{h}^m \phi^s \cos \zeta + \lambda \hat{\kappa} \left[ \hat{h}^s \phi^s (\hat{u}^s)^2 + \hat{h}^m \phi^s \left( (\hat{u}^s)^2 - \gamma (\hat{u}^f)^2 \right) \right] \\ &\quad - \gamma \int_{\hat{b}}^{\hat{\xi}^i} \varepsilon \hat{C}^d (\hat{w}^f - \hat{w}^s) / \phi^f d\hat{z} + O(\varepsilon), \end{aligned} \quad (\text{B10})$$

respectively.

In our work, we assume that the vertical relative motion between the solid and fluid phases is induced by the dilatancy effects of grains in the lower layer of mixture, as described in Pailha and Pouliquen (2009) and Sun et al. (2023). Therefore, vertical integration of Equation 16 from the bottom to any position within the saturated mixture, alongside the kinematic conditions (A12 c-d) on the bottom, results in the following equation:

$$\varepsilon \phi^f (\hat{w}^s - \hat{w}^f) = \int_{\hat{b}}^{\hat{z}} \hat{\gamma}^s \tan \psi d\hat{z}, \quad (\text{B11})$$

Additionally, we adopt the assumption from Sun et al. (2023) that

$$\int_{\hat{b}}^{\hat{\xi}^i} \hat{C}^d \left( \int_{\hat{b}}^{\hat{z}} \hat{\gamma}^s \tan \psi d\hat{z} \right) d\hat{z} = K_4 \hat{C}^d (\hat{h}^m)^2 (\hat{\gamma}^s)^b \tan \psi^b. \quad (\text{B12})$$

Substituting Equation B12 into Equations B9 and B10, respectively, reveals that the basal pore fluid pressure and the basal solid effective stress take the following forms:

$$\hat{p}_e^{f*}(\hat{b}) = \hat{h}^m \cos \zeta + \lambda \hat{\kappa} \hat{h}^m (\hat{u}^f)^2 - K_4 \hat{C}^d (\hat{h}^m)^2 (\hat{\gamma}^s)^b \tan \psi^b / (\phi^f)^2 + O(\varepsilon), \quad (\text{B13})$$

$$\begin{aligned} \hat{\sigma}_{zz}^e(\hat{b}) &= \hat{h}^s \phi^s \cos \zeta + (1 - \gamma) \hat{h}^m \phi^s \cos \zeta + \lambda \hat{\kappa} \left[ \hat{h}^s \phi^s (\hat{u}^s)^2 + \hat{h}^m \phi^s \left( (\hat{u}^s)^2 - \gamma (\hat{u}^f)^2 \right) \right] \\ &\quad + K_4 \hat{C}^d (\hat{h}^m)^2 (\hat{\gamma}^s)^b \tan \psi^b / (\phi^f)^2 + O(\varepsilon), \end{aligned} \quad (\text{B14})$$

respectively.

## Appendix C: Nondimensional Depth-Averaged Equations for the Under-Saturated Mixture Regime

### C1. Depth-Averaged Mass Balance Equations

Applying the aforementioned ordering of nondimensional parameters and integrating the nondimensional mass balance Equation A2 for the upper layer of pure grains from the interface to the free surface using Leibniz's rule to swap the order of differentiation and integration, and incorporating the kinematic boundary condition (A12a) on the free surface and the left-hand side of the granular mass transfer condition (A16), yields the following equation:

$$\frac{\partial}{\partial \hat{t}}(\hat{h}^g \phi^g) + \frac{\partial}{\partial \hat{x}}(\hat{h}^g \phi^g \bar{u}^g) = \hat{M}^s + O(\varepsilon^{1+\alpha}). \quad (C1)$$

Integrating the nondimensional mass balance Equation A6 for the solid phase of the lower layer of mixture from the bottom to the interface and applying the kinematic boundary condition on the bottom (A12c) and the right-hand side of the granular mass transfer condition (A16), we obtain the equation as follows:

$$\frac{\partial}{\partial \hat{t}}(\hat{h}^m \phi^s) + \frac{\partial}{\partial \hat{x}}(\hat{h}^m \phi^s \bar{u}^s) = -\hat{M}^s + O(\varepsilon^{1+\alpha}). \quad (C2)$$

Similarly, integrating the nondimensional mass balance Equation A9 for the fluid phase of the lower layer of mixture from the bottom to the interface and applying the kinematic boundary conditions (A12 c–d) results in:

$$\frac{\partial}{\partial \hat{t}}(\hat{h}^m \phi^f) + \frac{\partial}{\partial \hat{x}}(\hat{h}^m \phi^f \bar{u}^f) = O(\varepsilon^{1+\alpha}). \quad (C3)$$

Applying the reverse transformation based on the scaling Equation A1, the nondimensional depth-averaged mass balance Equations C1–C3 are converted back into their dimensional forms. The resulting dimensional equations correspond to Equations 42–44 presented in the main text.

### C2. Depth-Averaged Momentum Balance Equations

The non-dimensional downslope component of the momentum balance Equation A4 for the upper layer of pure grains can be integrated from the interface to the free surface using Leibniz's rule to swap the order of differentiation and integration. By applying the kinematic boundary condition (A12a), the left-hand side of the granular mass transfer condition (A16), the downslope traction free condition (A13a), and the granular momentum jump condition (A18a), coupled with the downslope friction condition (A19a) for the solid phase of the mixture on the interface, the following equation is obtained:

$$\begin{aligned} \frac{\partial}{\partial \hat{t}}(\hat{h}^g \phi^g \bar{u}^g) + \frac{\partial}{\partial \hat{x}}(\hat{h}^g \phi^g \overline{(\hat{u}^g)^2}) &= \hat{h}^g \phi^g \sin \zeta + \hat{M}^s \bar{u}^s - \varepsilon \frac{\partial}{\partial \hat{x}}(\hat{h}^g \phi^g \bar{\sigma}_{xx}^e) \\ &+ \left( -\varepsilon \frac{\partial \hat{\zeta}^i}{\partial \hat{x}} + \mu^i \frac{\hat{u}^s - \hat{u}^g}{|\hat{u}^s - \hat{u}^g|} \right) (\mathbf{n}^i \cdot \hat{\boldsymbol{\sigma}}^e \mathbf{n}^i) + O(\varepsilon^{1+\alpha}). \end{aligned} \quad (C4)$$

here, the interfacial solid normal effective stress ( $\mathbf{n}^i \cdot \hat{\boldsymbol{\sigma}}^e \mathbf{n}^i$ ) is necessary to be expressed explicitly. From the conditions (A18b), (A19b), and the Equation B5, we can obtain that

$$(\mathbf{n}^i \cdot \hat{\boldsymbol{\sigma}}^e \mathbf{n}^i) = \hat{h}^g \phi^g \cos \zeta + \lambda \hat{k} \hat{h}^g \phi^g (\hat{u}^g)^2 + O(\varepsilon). \quad (C5)$$

Additionally, in our model, we postulate that  $\bar{\sigma}_{xx}^e = \bar{\sigma}_{zz}^e$  for grains in the upper and lower layers. The depth-averaged solid effective normal stress  $\bar{\sigma}_{zz}^e$  for the upper layer grains can be obtained by depth-averaging equation (B4), leading to the following result:

$$\bar{\sigma}_{zz}^e = \frac{1}{\hat{h}^g} \int_{\hat{z}}^{\hat{z}^g} \hat{\sigma}_{zz}^e(\hat{z}) d\hat{z} = \frac{1}{2} \hat{h}^g \phi^g \cos \zeta + O(\epsilon^\alpha). \quad (C6)$$

By substituting the expressions for the interfacial solid normal effective stress (C5) and the depth-averaged solid effective normal stress (C6) for the upper layer grains into equation (C4), we obtain the depth-averaged momentum equation for the pure grains upper layer in the following form:

$$\begin{aligned} \frac{\partial}{\partial \hat{t}} (\hat{h}^g \phi^g \bar{u}^g) + \frac{\partial}{\partial \hat{x}} \left( \hat{h}^g \phi^g \overline{(\hat{u}^g)^2} + \epsilon \frac{1}{2} (\hat{h}^g)^2 \phi^g \cos \zeta \right) &= \hat{h}^g \phi^g \sin \zeta + \hat{M}^s \bar{u}^s - \epsilon \hat{h}^g \phi^g \cos \zeta \frac{\partial \hat{h}^m}{\partial \hat{x}} \\ &+ \mu^i \frac{\hat{u}^s - \hat{u}^g}{|\hat{u}^s - \hat{u}^g|} \left( \hat{h}^g \phi^g \cos \zeta + \lambda \hat{k} \hat{h}^g \phi^g (\hat{u}^g)^2 \right) + O(\epsilon^{1+\alpha}). \end{aligned} \quad (C7)$$

Integrating the nondimensional downslope component of the momentum balance Equation A7 for the solid phase of the lower layer of mixture from the bottom to the interface and incorporating the kinematic boundary condition (A12c), the right-hand side of the granular mass transfer condition (A16), the downslope friction conditions (A19a) for the solid phase of the mixture on the interface, and on the bottom (A14a) yields the following equation:

$$\begin{aligned} \frac{\partial}{\partial \hat{t}} (\hat{h}^m \phi^s \bar{u}^s) + \frac{\partial}{\partial \hat{x}} \left( \hat{h}^m \phi^s \overline{(\hat{u}^s)^2} \right) &= \hat{h}^m \phi^s \sin \zeta - \hat{M}^s \bar{u}^s - \epsilon \frac{\partial}{\partial \hat{x}} (\hat{h}^m \bar{\sigma}_{xx}^e) - \epsilon \gamma \phi^s \frac{\partial}{\partial \hat{x}} (\hat{h}^m \bar{p}^{f*}) \\ - \epsilon \gamma \phi^s \bar{p}^{f*} \frac{\partial \hat{b}}{\partial \hat{x}} - \left( -\epsilon \frac{\partial \hat{\xi}^j}{\partial \hat{x}} + \mu^i \frac{\hat{u}^s - \hat{u}^g}{|\hat{u}^s - \hat{u}^g|} \right) (\mathbf{n}^i \cdot \hat{\sigma}^e \mathbf{n}^i) &- \left( \epsilon \frac{\partial \hat{b}}{\partial \hat{x}} + \mu^b \frac{\hat{u}_b^s}{|\hat{u}_b^s|} \right) (\mathbf{n}^b \cdot \hat{\sigma}^e \mathbf{n}^b) \\ + \gamma \hat{C}^d \hat{h}^m (\bar{u}^f - \bar{u}^s) &+ O(\epsilon^{1+\alpha}). \end{aligned} \quad (C8)$$

According to condition (A19b) and Equation B14, the basal solid normal effective stress ( $\mathbf{n}^b \cdot \hat{\sigma}^e \mathbf{n}^b$ ) in Equation C8 is given by:

$$\begin{aligned} (\mathbf{n}^b \cdot \hat{\sigma}^e \mathbf{n}^b) &= \hat{h}^g \phi^g \cos \zeta + (1 - \gamma) \hat{h}^m \phi^s \cos \zeta + \lambda \hat{k} \left[ \hat{h}^g \phi^g (\hat{u}^g)^2 + \hat{h}^m \phi^s \left( (\hat{u}^s)^2 - \gamma (\hat{u}^f)^2 \right) \right] \\ &+ K_4 \hat{C}^d (\hat{h}^m)^2 \left( \hat{\gamma}^s \right)^b \tan \psi^b / (\phi^f)^2 + O(\epsilon). \end{aligned} \quad (C9)$$

Moreover, the depth-averaged pore fluid pressure  $\bar{p}^{f*}$  and the depth-averaged solid effective normal stress  $\bar{\sigma}_{zz}^e$  for the solid phase of the lower layer of mixture can be obtained by depth-integrating Equations B6a and B8, resulting in the following equations:

$$\bar{p}^{f*} = \frac{1}{\hat{h}^m} \int_{\hat{z}}^{\hat{z}^j} \hat{p}^{f*}(\hat{z}) d\hat{z} = \frac{1}{2} \hat{h}^m \cos \zeta + O(\epsilon^\alpha). \quad (C10)$$

$$\bar{\sigma}_{zz}^e = \frac{1}{\hat{h}^m} \int_{\hat{z}}^{\hat{z}^j} \hat{\sigma}_{zz}^e(\hat{z}) d\hat{z} = \hat{h}^g \phi^g \cos \zeta + \frac{1}{2} (1 - \gamma) \hat{h}^m \phi^s \cos \zeta + O(\epsilon^\alpha). \quad (C11)$$

In our model, we assume the absence of shallow topography superimposed over the reference coordinate surface, meaning  $\hat{b}(\hat{x}) = 0$ . Consequently, the terms corresponding to the gradient of the basal topography in Equation C9 vanish. Additionally, it is worth reminding that  $\bar{\sigma}_{xx}^e = \bar{\sigma}_{zz}^e$  for the solid phase of the lower layer of the mixture. Then, substituting the interfacial solid normal effective stress (C5), the basal solid normal effective stress (C9), the depth-averaged pore fluid pressure (C10), and the depth-averaged solid effective normal stress (C11) for the solid phase of the lower layer of mixture into equation (C8) yields the depth-averaged momentum equation for the solid phase of the lower layer of saturated mixture in the following form:

$$\begin{aligned}
\frac{\partial}{\partial t}(\hat{h}^m \phi^s \bar{u}^s) + \frac{\partial}{\partial \hat{x}} \left( \hat{h}^m \phi^s \overline{(\hat{u}^s)^2} + \varepsilon \frac{1}{2} (\hat{h}^m)^2 \phi^s \cos \zeta \right) &= \hat{h}^m \phi^s \sin \zeta - \hat{M}^s \bar{u}^s + \varepsilon \gamma \frac{1}{2} (\hat{h}^m)^2 \cos \zeta \frac{\partial \phi^s}{\partial \hat{x}} \\
-\varepsilon \hat{h}^m \frac{\partial}{\partial \hat{x}} (\hat{h}^s \phi^s \cos \zeta) - \mu^i \frac{\hat{u}^s - \hat{u}^g}{|\hat{u}^s - \hat{u}^g|} (\hat{h}^s \phi^s \cos \zeta + \lambda \hat{\kappa} \hat{h}^s \phi^s (\hat{u}^s)^2) + \gamma \hat{C}^d \hat{h}^m (\bar{u}^f - \bar{u}^s) \\
-\mu^b \frac{\hat{u}_b^s}{|\hat{u}_b^s|} \left\{ \hat{h}^s \phi^s \cos \zeta + (1 - \gamma) \hat{h}^m \phi^s \cos \zeta + \lambda \hat{\kappa} \left[ \hat{h}^s \phi^s (\hat{u}^s)^2 + \hat{h}^m \phi^s \left( (\hat{u}^s)^2 - \gamma (\hat{u}^f)^2 \right) \right] \right\} \\
+ K_4 \hat{C}^d (\hat{h}^m)^2 \left( \hat{\gamma}^s \right)^b \tan \psi^b / (\phi^f)^2 \Big\} + O(\varepsilon^{1+\alpha}).
\end{aligned} \tag{C12}$$

Analogously, by integrating the nondimensional downslope component of the momentum balance Equation A10 for the fluid phase of the lower layer of mixture from the bottom to the interface and applying the kinematic boundary conditions (A12 b,d), the normal component of the momentum condition (A17a) for the fluid phase of the mixture on the interface and the normal component of the friction condition (A15a) for the fluid phase on the bottom, we obtain the following equation:

$$\begin{aligned}
\frac{\partial}{\partial t}(\hat{h}^m \phi^f \bar{u}^f) + \frac{\partial}{\partial \hat{x}} \left( \hat{h}^m \phi^f \overline{(\hat{u}^f)^2} \right) &= \hat{h}^m \phi^f \sin \zeta - \varepsilon \phi^f \frac{\partial}{\partial \hat{x}} (\hat{h}^m \bar{p}^{f*}) + \varepsilon (\mathbf{n}^b \cdot \hat{\boldsymbol{\sigma}}^f \mathbf{n}^b) \frac{\partial \hat{b}}{\partial \hat{x}} \\
-\varepsilon \phi^f \hat{p}^{f*} \frac{\partial \hat{b}}{\partial \hat{x}} - \hat{C}^d \hat{h}^m (\bar{u}^f - \bar{u}^s) - C^f |\bar{u}^f| |\bar{u}^f| + O(\varepsilon^{1+\alpha}).
\end{aligned} \tag{C13}$$

According to the friction condition for the fluid phase on the bottom (A15b) and the expression for the basal pore fluid pressure (B9), the basal fluid normal stress ( $\mathbf{n}^b \cdot \hat{\boldsymbol{\sigma}}^f \mathbf{n}^b$ ) in (C13) can be expressed as follows:

$$(\mathbf{n}^b \cdot \hat{\boldsymbol{\sigma}}^f \mathbf{n}^b) = - \left( \hat{h}^m \phi^f \cos \zeta + \lambda \hat{\kappa} \hat{h}^m \phi^f (\hat{u}^f)^2 \right) + O(\varepsilon). \tag{C14}$$

After substituting the expression for the depth-averaged pore fluid pressure (C10) and the basal fluid normal stress (C14) into Equation C13 and considering  $\hat{b}(\hat{x}) = 0$ , the resulting depth-averaged momentum equation for the fluid phase of the saturated mixture lower layer is given by:

$$\begin{aligned}
\frac{\partial}{\partial t}(\hat{h}^m \phi^f \bar{u}^f) + \frac{\partial}{\partial \hat{x}} \left( \hat{h}^m \phi^f \overline{(\hat{u}^f)^2} + \varepsilon \frac{1}{2} (\hat{h}^m)^2 \phi^f \cos \zeta \right) &= \hat{h}^m \phi^f \sin \zeta + \varepsilon \frac{1}{2} (\hat{h}^m)^2 \cos \zeta \frac{\partial \phi^f}{\partial \hat{x}} \\
- \hat{C}^d \hat{h}^m (\bar{u}^f - \bar{u}^s) - C^f |\bar{u}^f| |\bar{u}^f| + O(\varepsilon^{1+\alpha}).
\end{aligned} \tag{C15}$$

Then, employing the reverse transformation using the scaling Equation A1, the nondimensional depth-averaged momentum balance Equations C1–C3 are converted back into their dimensional forms. The resulting dimensional Equations 45–50 presented in the main text are obtained.

## Appendix D: Nondimensional Equations for the Over-Saturated Mixture Regime

In this appendix, we exclusively present the nondimensional forms of the governing Equations 12 and 13 for the upper layer of pure fluid and the boundary conditions (23) and (25) on the pure fluid free surface and (33)–(40) on the granular interface in the over-saturated mixture regime. The nondimensional governing equations for the lower layer of the mixture and the boundary conditions on the bottom remain identical to those in the appendix for the under-saturated mixture regime. Hence, we do not repeat them here.

The nondimensional form of the mass balance equation for the upper layer of pure fluid (12) is as follows:

$$\frac{\partial}{\partial \hat{x}} (\hat{u}^{pf} \Psi) + \frac{\partial \hat{w}^{pf}}{\partial \hat{z}} - \varepsilon \lambda \hat{\kappa}' \hat{z} \hat{u}^{pf} \Psi^2 - \varepsilon \lambda \hat{\kappa} \hat{w}^{pf} \Psi = 0, \tag{D1}$$

and the nondimensional downslope and normal components of the momentum balance Equation 13 for the pure fluid are as follows:

$$\begin{aligned} \frac{\partial \hat{u}^{pf}}{\partial \hat{t}} + \frac{\partial}{\partial \hat{x}} \left( (\hat{u}^{pf})^2 \Psi \right) + \frac{\partial}{\partial \hat{z}} \left( \hat{u}^{pf} \hat{w}^{pf} \right) - \varepsilon \lambda \hat{\kappa}' \hat{z} (\hat{u}^{pf})^2 \Psi^2 - 2\varepsilon \lambda \hat{\kappa} \hat{u}^{pf} \hat{w}^{pf} \Psi = \sin \zeta \\ + \varepsilon^2 \frac{\partial}{\partial \hat{x}} (\hat{\tau}_{xx}^f \Psi) - \varepsilon \frac{\partial}{\partial \hat{x}} (\hat{p}^{f*} \Psi) + \frac{\partial \hat{\tau}_{xz}^f}{\partial \hat{z}} - \varepsilon^3 \lambda \hat{\kappa}' \hat{z} \hat{\tau}_{xx}^f \Psi^2 - 2\varepsilon \lambda \hat{\kappa} \hat{\tau}_{xz}^f \Psi, \end{aligned} \quad (D2)$$

$$\begin{aligned} \varepsilon \left( \frac{\partial \hat{w}^{pf}}{\partial \hat{t}} + \frac{\partial}{\partial \hat{x}} (\hat{u}^{pf} \hat{w}^{pf} \Psi) + \frac{\partial}{\partial \hat{z}} \left( (\hat{w}^{pf})^2 \right) \right) - \varepsilon^2 \lambda \hat{\kappa}' \hat{z} \hat{u}^{pf} \hat{w}^{pf} \Psi^2 - \varepsilon^2 \lambda \hat{\kappa} (\hat{w}^{pf})^2 \Psi + \lambda \hat{\kappa} (\hat{u}^{pf})^2 \Psi \\ = -\cos \zeta + \varepsilon \frac{\partial}{\partial \hat{x}} (\hat{\tau}_{xz}^f \Psi) + \varepsilon \frac{\partial \hat{\tau}_{zz}^f}{\partial \hat{z}} - \frac{\partial \hat{p}^{f*}}{\partial \hat{z}} - \varepsilon^2 \lambda \hat{\kappa}' \hat{z} \hat{\tau}_{xz}^f \Psi^2 - \varepsilon^2 \lambda \hat{\kappa} (\hat{\tau}_{zz}^f - \hat{\tau}_{xx}^f) \Psi. \end{aligned} \quad (D3)$$

The nondimensional forms of the kinematic boundary conditions on the pure fluid free surface (23) and the granular interface (33) are given as follows:

$$\left. \begin{aligned} \frac{\partial \hat{\xi}^f}{\partial \hat{t}} + \hat{u}^{pf} \Psi \frac{\partial \hat{\xi}^f}{\partial \hat{x}} - \hat{w}^{pf} = 0, \quad \hat{z} = \hat{\xi}^f(\hat{x}, \hat{t}), \\ \frac{\partial \hat{\xi}^i}{\partial \hat{t}} + \hat{u}^s \Psi \frac{\partial \hat{\xi}^i}{\partial \hat{x}} - \hat{w}^s = 0, \quad \hat{z} = \hat{\xi}^i(\hat{x}, \hat{t}). \end{aligned} \right\} \quad (D4a-b)$$

On the free surface of the upper layer of pure fluid, the nondimensional downslope and normal components of the traction free boundary condition (25) are as follows:

$$\left. \begin{aligned} \varepsilon \hat{p}^{f*} \Psi \frac{\partial \hat{\xi}^f}{\partial \hat{x}} - \varepsilon^2 \hat{\tau}_{xx}^f \Psi \frac{\partial \hat{\xi}^f}{\partial \hat{x}} + \hat{\tau}_{xz}^f = 0, \quad \hat{z} = \hat{\xi}^f(\hat{x}, \hat{t}), \\ -\varepsilon \hat{\tau}_{xz}^f \Psi \frac{\partial \hat{\xi}^f}{\partial \hat{x}} - \hat{p}^{f*} + \varepsilon \hat{\tau}_{zz}^f = 0, \quad \hat{z} = \hat{\xi}^f(\hat{x}, \hat{t}). \end{aligned} \right\} \quad (D5a-b)$$

In the over-saturated mixture regime, the interface between layers is a granular material surface. Across this interface, a mass transfer of fluid can occur. On this interface, the nondimensional fluid mass transfer (35) is as follows:

$$\hat{M}^f = -\frac{1}{|\nabla \hat{F}^f|} \left( \frac{\partial \hat{\xi}^i}{\partial \hat{t}} + \hat{u}^{pf} \Psi \frac{\partial \hat{\xi}^i}{\partial \hat{x}} - \hat{w}^{pf} \right) = -\frac{1}{|\nabla \hat{F}^f|} \phi^f \left( \frac{\partial \hat{\xi}^i}{\partial \hat{t}} + \hat{u}^f \Psi \frac{\partial \hat{\xi}^i}{\partial \hat{x}} - \hat{w}^f \right). \quad (D6)$$

On this granular interface, the nondimensional downslope and normal components of the momentum conditions (38) for the fluid phase and (39) for the solid phase of the lower layer of the mixture, coupled with the definition of the partial granular stress (5), are given as follows:

$$\left. \begin{aligned} \varepsilon \phi^f (\hat{p}^{f*})^- \Psi \frac{\partial \hat{\xi}^i}{\partial \hat{x}} - \varepsilon^2 \hat{\tau}_{xx}^{f-} \Psi \frac{\partial \hat{\xi}^i}{\partial \hat{x}} + \hat{\tau}_{xz}^{f-} = \varepsilon \phi^f (\hat{p}^{f*})^+ \Psi \frac{\partial \hat{\xi}^i}{\partial \hat{x}} - \varepsilon^2 \phi^f \hat{\tau}_{xx}^{f+} \Psi \frac{\partial \hat{\xi}^i}{\partial \hat{x}} \\ + \phi^f \hat{\tau}_{xz}^{f+} - \hat{M}^f (\hat{u}^{pf} - \hat{u}^f), \\ -\varepsilon \hat{\tau}_{xz}^{f-} \Psi \frac{\partial \hat{\xi}^i}{\partial \hat{x}} - \phi^f (\hat{p}^{f*})^- + \varepsilon \hat{\tau}_{zz}^{f-} = -\varepsilon \phi^f \hat{\tau}_{xz}^{f+} \Psi \frac{\partial \hat{\xi}^i}{\partial \hat{x}} - \phi^f (\hat{p}^{f*})^+ + \varepsilon \phi^f \hat{\tau}_{zz}^{f+} \\ - \varepsilon \hat{M}^f (\hat{w}^{pf} - \hat{w}^f). \end{aligned} \right\} \quad (D7a-b)$$

$$\left. \begin{aligned} \varepsilon\gamma\phi^s(\hat{p}^{f*})^-\Psi\frac{\partial\hat{\xi}^i}{\partial\hat{x}} + \varepsilon\hat{\sigma}_{xx}^e\Psi\frac{\partial\hat{\xi}^i}{\partial\hat{x}} - \mu\hat{\sigma}_{xz}^e &= \varepsilon\gamma\phi^s(\hat{p}^{f*})^+\Psi\frac{\partial\hat{\xi}^i}{\partial\hat{x}} - \varepsilon^2\gamma\phi^s\hat{\tau}_{xx}^{f+}\Psi\frac{\partial\hat{\xi}^i}{\partial\hat{x}} \\ &\quad + \gamma\phi^s\hat{\tau}_{xz}^{f+}, \\ \varepsilon\mu\hat{\sigma}_{xz}^e\Psi\frac{\partial\hat{\xi}^i}{\partial\hat{x}} - \gamma\phi^f(\hat{p}^{f*})^- - \hat{\sigma}_{zz}^e &= -\varepsilon\gamma\phi^s\hat{\tau}_{xz}^{f+}\Psi\frac{\partial\hat{\xi}^i}{\partial\hat{x}} - \gamma\phi^s(\hat{p}^{f*})^+ + \varepsilon\gamma\phi^s\hat{\tau}_{zz}^{f+}, \end{aligned} \right\} \quad (\text{D8a-b})$$

respectively.

Additionally, on the interface, the nondimensional downslope and normal components of the friction conditions (40) for the upper layer of pure fluid are as follows:

$$\left. \begin{aligned} \varepsilon(\hat{p}^{f*})^+\Psi\frac{\partial\hat{\xi}^i}{\partial\hat{x}} - \varepsilon^2\hat{\tau}_{xx}^{f+}\Psi\frac{\partial\hat{\xi}^i}{\partial\hat{x}} + \hat{\tau}_{xz}^{f+} &= -\varepsilon(\mathbf{n}^i \cdot \hat{\boldsymbol{\sigma}}^{f+}\mathbf{n}^i)\Psi\frac{\partial\hat{\xi}^i}{\partial\hat{x}} \\ &\quad + C^f|\bar{u}^{pf} - \bar{u}^m|(\bar{u}^{pf} - \bar{u}^m), \\ -\varepsilon\hat{\tau}_{xz}^{f+}\Psi\frac{\partial\hat{\xi}^i}{\partial\hat{x}} - (\hat{p}^{f*})^+ + \varepsilon\hat{\tau}_{zz}^{f+} &= (\mathbf{n}^i \cdot \hat{\boldsymbol{\sigma}}^{f+}\mathbf{n}^i) + \varepsilon C^f|\bar{w}^{pf} - \bar{w}^m|(\bar{w}^{pf} - \bar{w}^m). \end{aligned} \right\} \quad (\text{D9a-b})$$

By integrating the nondimensional Equations D1–D3 for the upper layer of pure fluid from the granular interface to the pure fluid free surface and the nondimensional Equations A6–A11 for the solid and fluid phases of the lower layer of mixture from the bottom to the granular interface, along with the corresponding aforementioned nondimensional kinematic and dynamic boundary conditions, we can obtain the nondimensional depth-averaged equations for the over-saturated mixture regime. The depth-integrating process is analogous to that in the appendix for the under-saturated mixture regime, and we do not repeat it again. Subsequently, employing the reverse transformation using the scaling Equation A1, the nondimensional depth-averaged mass and momentum balance equations for the over-saturated mixture regime can be converted back to their dimensional forms (51)–(59), as presented in the main text.

## Appendix E: Operator Splitting Method for Frictional Forces in the Under-Saturated Mixture Regime

In this appendix, we present the operator splitting method used to handle the friction terms for the upper pure grain layer and the lower mixture layer in the under-saturated mixture regime. First, we calculate the intermediate solution for both the upper and lower layers without the friction terms, using a second-order Runge-Kutta solver applied to the first equation of 105. In the second step, as described in the second equation of 105, the contribution of the friction terms is taken into account. In the under-saturated mixture flow regime, the flow thickness and the momentum of the pure grains in the upper layer and the granular phase in the lower layer of the mixture in the numerical cell  $I_j$  are denoted as  $(\bar{q}_1^g)_j = (h^g\phi^g)_j$ ,  $(\bar{q}_2^g)_j = (h^g\phi^g\bar{u}^g)_j$ , and  $(\bar{q}_1^s)_j = (h^m\phi^s)_j$ ,  $(\bar{q}_2^s)_j = (h^m\phi^s\bar{u}^s)_j$ , respectively.

In this flow regime, the motions of the upper pure grain layer and the lower mixture layer are mutually influenced by the interfacial frictional force. When the upper pure grain layer exceeds its yield stress, there will be relative motion between the upper and lower layers. Otherwise, the two layers move at same velocity, either flowing together or stopping simultaneously. To handle this, we first calculate the momentum of the granular phase in the lower mixture layer at the new time step,  $(\bar{q}_2^s)_j(t + \Delta t)$ , according to the following criterion:

$$\begin{aligned} \text{if } |(\bar{q}_1^{g*})_j(\bar{u}_j^{g*} - \bar{u}_j^{s*})| > \sigma_j^{g*} \Delta t, \\ (\bar{q}_2^s)_j(t + \Delta t) &= \begin{cases} (\bar{q}_2^{s*})_j + [(\mathcal{T}_u^{b*})_j - (\mathcal{T}_u^{i*})_j]\Delta t, & \text{if } |(\bar{q}_2^{s*})_j - (\mathcal{T}_u^{i*})_j|\Delta t > \sigma_j^{s*} \Delta t, \\ 0, & \text{otherwise,} \end{cases} \end{aligned} \quad (\text{E1})$$

else,

$$(\bar{q}_2^s)_j(t + \Delta t) = \begin{cases} (\bar{q}_2^{s*})_j + (\bar{q}_1^{g*})_j(\bar{u}_j^{g*} - \bar{u}_j^{s*}) + (\mathcal{T}_u^{b*})_j \Delta t, & \text{if } |(\bar{q}_2^{s*})_j + (\bar{q}_1^{g*})_j(\bar{u}_j^{g*} - \bar{u}_j^{s*})| \\ > \sigma_j^{s*} \Delta t, \\ 0, & \text{otherwise,} \end{cases} \quad (\text{E2})$$

where  $(\mathcal{T}_u^{i*})_j$  and  $(\mathcal{T}_u^{b*})_j$  represent the interfacial and basal granular frictional forces, respectively.  $\sigma_j^{g*}$  and  $\sigma_j^{s*}$  are the yield stresses for the upper pure grain layer and the granular phase in the lower layer of the mixture. According to the source term (49), these terms are given by

$$\begin{aligned} (\mathcal{T}_u^{i*})_j &= \frac{\bar{u}_j^{s*} - \bar{u}_j^{g*}}{|\bar{u}_j^{s*} - \bar{u}_j^{g*}|} \sigma_j^{g*}, & (\mathcal{T}_u^{b*})_j &= -\frac{\bar{u}_j^{s*}}{|\bar{u}_j^{s*}|} \sigma_j^{s*}, \\ \sigma_j^{g*} &= \mu^i \left( g \cos \zeta(\bar{q}_1^{g*})_j + \kappa(\bar{q}_1^{g*})_j (\bar{u}_j^{g*})^2 \right), \\ \sigma_j^{s*} &= \mu^b \left( \frac{(p_b^{p*})_j}{\rho^{s*}} + \kappa(\bar{q}_1^{s*})_j \left( (\bar{u}_j^{s*})^2 - \gamma(\bar{u}_j^{f*})^2 \right) + g \cos \zeta(\bar{q}_1^{s*})_j + \kappa(\bar{q}_1^{s*})_j (\bar{u}_j^{s*})^2 \right). \end{aligned} \quad (\text{E3})$$

Once  $(\bar{q}_2^s)_j(t + \Delta t)$  is obtained, the velocity of the granular phase in the lower layer of the mixture at the new time step can be calculated as

$$\bar{u}_j^s(t + \Delta t) = \frac{(\bar{q}_2^s)_j(t + \Delta t)}{(\bar{q}_1^s)_j(t + \Delta t)}. \quad (\text{E4})$$

Then, the momentum of the upper pure grain layer at the new time step,  $(\bar{q}_2^g)_j(t + \Delta t)$ , is updated according to the following criterion:

$$(\bar{q}_2^g)_j(t + \Delta t) = \begin{cases} (\bar{q}_2^{g*})_j + (\mathcal{T}_u^{i*})_j \Delta t, & \text{if } |(\bar{q}_1^{g*})_j(\bar{u}_j^{g*} - \bar{u}_j^{s*})| > \sigma_j^{g*} \Delta t, \\ (\bar{q}_1^{g*})_j \bar{u}_j^s(t + \Delta t), & \text{otherwise.} \end{cases} \quad (\text{E5})$$

It should be noted that when the lower layer of the mixture vanishes, the velocity of the granular phase in the lower layer of the mixture becomes  $\bar{u}_j^s = 0$ , and the interfacial frictional force  $(\mathcal{T}_u^{i*})_j$  degenerates to the basal granular frictional force  $(\mathcal{T}_u^{b*})_j$ . Consequently, (E5) reduces to (106), which describes the case of the single-layer pure grain flows.

## Conflict of Interest

The authors declare no conflicts of interest relevant to this study.

## Data Availability Statement

The data used in this research (Sun, 2024) are archived in the repository of the Technical University of Darmstadt: <https://doi.org/10.48328/tudatalib-1619>.

## References

- Abe, K., Soga, K., & Bandara, S. (2014). Material point method for coupled hydromechanical problems. *Journal of Geotechnical and Environmental Engineering*, 140(3), 04013033. [https://doi.org/10.1061/\(asce\)jt.1943-5606.0001011](https://doi.org/10.1061/(asce)jt.1943-5606.0001011)
- Abril, J., & Knight, D. (2004). Stage-discharge prediction for rivers in flood applying a depth-averaged model. *Journal of Hydraulic Research*, 42(6), 616–629. <https://doi.org/10.1080/00221686.2004.9628315>
- Allen, S. M., Thomas, E. L., & Jones, R. A. (1999). *The structure of materials*. J. Wiley.
- Anderson, T., & Jackson, R. (1967). A fluid mechanical description of fluidized beds: Equations of motion. *Industrial & Engineering Chemistry Fundamentals*, 6(4), 527–539. <https://doi.org/10.1021/i160024a007>

## Acknowledgments

We are grateful to the financial support by the German Research Foundation (DFG, German Research Foundation) through Project No. 425259073. Open Access funding enabled and organized by Projekt DEAL.

- Askari, H., & Kamrin, K. (2016). Intrusion rheology in grains and other flowable materials. *Nature Materials*, *15*(12), 1274–1279. <https://doi.org/10.1038/nmat4727>
- Audusse, E., Bouchut, F., Bristeau, M.-O., Klein, R., & Perthame, B. t. (2004). A fast and stable well-balanced scheme with hydrostatic reconstruction for shallow water flows. *SIAM Journal on Scientific Computing*, *25*(6), 2050–2065. <https://doi.org/10.1137/s1064827503431090>
- Baker, J., Johnson, C., & Gray, J. (2016). Segregation-induced finger formation in granular free-surface flows. *Journal of Fluid Mechanics*, *809*, 168–212. <https://doi.org/10.1017/jfm.2016.673>
- Bandara, S., & Soga, K. (2015). Coupling of soil deformation and pore fluid flow using material point method. *Computers and Geotechnics*, *63*, 199–214. <https://doi.org/10.1016/j.compgeo.2014.09.009>
- Baumgarten, A., & Kamrin, K. (2019). A general fluid-sediment mixture model and constitutive theory validated in many flow regimes. *Journal of Fluid Mechanics*, *861*, 721–764. <https://doi.org/10.1017/jfm.2018.914>
- Bollerlmann, A., Chen, G., Kurganov, A., & Noelle, S. (2013). A well-balanced reconstruction of wet/dry fronts for the shallow water equations. *Journal of Scientific Computing*, *56*(2), 267–290. <https://doi.org/10.1007/s10915-012-9677-5>
- Bouchut, F., Delgado-Sánchez, J. M., Fernández-Nieto, E. D., Mangeney, A., & Narbona-Reina, G. (2022). A bed pressure correction of the friction term for depth-averaged granular flow models. *Applied Mathematical Modelling*, *106*, 627–658. <https://doi.org/10.1016/j.apm.2022.01.034>
- Bouchut, F., Fernández-Nieto, E. D., Koné, E. H., Mangeney, A., & Narbona-Reina, G. (2017). A two-phase solid-fluid model for dense granular flows including dilatancy effects: Comparison with submarine granular collapse experiments. In *EPJ web of conferences* (Vol. 140, p. 09039). <https://doi.org/10.1051/epjconf/201714009039>
- Bouchut, F., Fernandez-Nieto, E. D., Mangeney, A., & Narbona-Reina, G. (2015). A two-phase shallow debris flow model with energy balance. *ESAIM: Mathematical Modelling and Numerical Analysis*, *49*(1), 101–140. <https://doi.org/10.1051/m2an/2014026>
- Bouchut, F., Fernández-Nieto, E. D., Mangeney, A., & Narbona-Reina, G. (2016). A two-phase two-layer model for fluidized granular flows with dilatancy effects. *Journal of Fluid Mechanics*, *801*, 166–221. <https://doi.org/10.1017/jfm.2016.417>
- Bouchut, F., Fernández-Nieto, E. D., Koné, E. H., Mangeney, A., & Narbona-Reina, G. (2021). Dilatancy in dry granular flows with a compressible  $\mu(i)$  rheology. *Journal of Computational Physics*, *429*, 110013. <https://doi.org/10.1016/j.jcp.2020.110013>
- Bouchut, F., & Westdickenberg, M. (2004). Gravity driven shallow water models for arbitrary topography. *Communications in Mathematical Sciences*, *2*(3), 359–389. <https://doi.org/10.4310/cms.2004.v2.n3.a2>
- Bougouin, A., Lacaze, L., & Bonometti, T. (2019). Collapse of a liquid-saturated granular column on a horizontal plane. *Physical Review Fluids*, *4*(12), 124306. <https://doi.org/10.1103/physrevfluids.4.124306>
- Boyer, F., Guazzelli, É., & Pouliquen, O. (2011). Unifying suspension and granular rheology. *Physical Review Letters*, *107*(18), 188301. <https://doi.org/10.1103/physrevlett.107.188301>
- Cassar, C., Nicolas, M., & Pouliquen, O. (2005). Submarine granular flows down inclined planes. *Physics of Fluids*, *17*(10), 103301. <https://doi.org/10.1063/1.2069864>
- Ceccato, F., Leonardi, A., Girardi, V., Simonini, P., & Pirulli, M. (2020). Numerical and experimental investigation of saturated granular column collapse in air. *Soils and Foundations*, *60*(3), 683–696. <https://doi.org/10.1016/j.sandf.2020.04.004>
- Chaudhry, M. H. (2008). *Open-channel flow* (Vol. 523). Springer.
- Chertock, A., Cui, S., Kurganov, A., & Wu, T. (2015). Well-balanced positivity preserving central-upwind scheme for the shallow water system with friction terms. *International Journal for Numerical Methods in Fluids*, *78*(6), 355–383. <https://doi.org/10.1002/ld.4023>
- Chiou, M.-C., Wang, Y., & Hutter, K. (2005). Influence of obstacles on rapid granular flows. *Acta Mechanica*, *175*(1–4), 105–122. <https://doi.org/10.1007/s00707-004-0208-9>
- Coulomb, C. A. (1773). *Essai sur une application des regles de maximis et minimis a quelques problemes de statique relatifs a l'architecture*. Mem. Div. Sav. Acad.
- Davies, T. R. (1990). Debris-flow surges—Experimental simulation. *Journal of Hydrology (New Zealand)*, 18–46.
- De Haas, T., Braat, L., Leuven, J. R., Lokhorst, I. R., & Kleinhans, M. G. (2015). Effects of debris flow composition on runout, depositional mechanisms, and deposit morphology in laboratory experiments. *Journal of Geophysical Research: Earth Surface*, *120*(9), 1949–1972. <https://doi.org/10.1002/2015jgf003525>
- Delannay, R., Valance, A., Mangeney, A., Roche, O., & Richard, P. (2017). Granular and particle-laden flows: From laboratory experiments to field observations. *Journal of Physics D: Applied Physics*, *50*(5), 053001. <https://doi.org/10.1088/1361-6463/50/5/053001>
- Delgado-Sánchez, J. M., Bouchut, F., Fernández-Nieto, E. D., Mangeney, A., & Narbona-Reina, G. (2020). A two-layer shallow flow model with two axes of integration, well-balanced discretization and application to submarine avalanches. *Journal of Computational Physics*, *406*, 109186. <https://doi.org/10.1016/j.jcp.2019.109186>
- De Saint-Venant, A. J. C. (1871). Théorie du mouvement non-permanent des eaux, avec application aux crues des rivières et à l'introduction des marées dans leur lit. *CR Acad. Sci. Paris*, *73*(147–154), 237–240.
- Dunatunga, S., & Kamrin, K. (2015). Continuum modelling and simulation of granular flows through their many phases. *Journal of Fluid Mechanics*, *779*, 483–513. <https://doi.org/10.1017/jfm.2015.383>
- Edwards, A., & Gray, J. (2015). Erosion–deposition waves in shallow granular free-surface flows. *Journal of Fluid Mechanics*, *762*, 35–67. <https://doi.org/10.1017/jfm.2014.643>
- Fernández-Nieto, E. D., Bouchut, F., Bresch, D., Diaz, M. C., & Mangeney, A. (2008). A new Savage–Hutter type model for submarine avalanches and generated tsunami. *Journal of Computational Physics*, *227*(16), 7720–7754. <https://doi.org/10.1016/j.jcp.2008.04.039>
- Forterre, Y., & Pouliquen, O. (2008). Flows of dense granular media. *Annual Review of Fluid Mechanics*, *40*, 1–24. <https://doi.org/10.1146/annurev.fluid.40.111406.102142>
- Gerbeau, J.-F., & Perthame, B. (2001). Derivation of viscous Saint-venant system for laminar shallow water; numerical validation. *Discrete and Continuous Dynamical Systems - B*, *1*(1), 89–102. <https://doi.org/10.3934/dcdsb.2001.1.89>
- Gray, J., & Edwards, A. (2014). A depth-averaged  $\mu(I)$ -rheology for shallow granular free-surface flows. *Journal of Fluid Mechanics*, *755*, 503–534. <https://doi.org/10.1017/jfm.2014.450>
- Gray, J., Wieland, M., & Hutter, K. (1999). Gravity-driven free surface flow of granular avalanches over complex basal topography. *Proceedings of the Royal Society of London. Series A: Mathematical, Physical and Engineering Sciences*, *455*(1985), 1841–1874. <https://doi.org/10.1098/rspa.1999.0383>
- He, K., Shi, H., & Yu, X. (2022). Effects of interstitial water on collapses of partially immersed granular columns. *Physics of Fluids*, *34*(2), 023306. <https://doi.org/10.1063/5.0079468>
- Heß, J., Tai, Y.-C., & Wang, Y. (2019). Debris flows with pore pressure and intergranular friction on rugged topography. *Computers & Fluids*, *190*, 139–155. <https://doi.org/10.1016/j.compfluid.2019.06.015>

- Heß, J., & Wang, Y. (2019). On the role of pore-fluid pressure evolution and hypoplasticity in debris flows. *European Journal of Mechanics - B: Fluids*, 74, 363–379. <https://doi.org/10.1016/j.euromechflu.2018.09.005>
- Ionescu, I. R., Mangeney, A., Bouchut, F., & Roche, O. (2015). Viscoplastic modeling of granular column collapse with pressure-dependent rheology. *Journal of Non-Newtonian Fluid Mechanics*, 219, 1–18. <https://doi.org/10.1016/j.jnnfm.2015.02.006>
- Iverson, L. M., LaHusen, R. G., & Berti, M. (2010). The perfect debris flow? Aggregated results from 28 large-scale experiments. *Journal of Geophysical Research*, 115(F3), F03005. <https://doi.org/10.1029/2009jf001514>
- Iverson, R., George, D. L., Allstadt, K., Reid, M. E., Collins, B. D., Vallance, J. W., et al. (2015). Landslide mobility and hazards: Implications of the 2014 OSO disaster. *Earth and Planetary Science Letters*, 412, 197–208. <https://doi.org/10.1016/j.epsl.2014.12.020>
- Iverson, R. M. (1997). The physics of debris flows. *Reviews of Geophysics*, 35(3), 245–296. <https://doi.org/10.1029/97rg00426>
- Iverson, R. M. (2005). Regulation of landslide motion by dilatancy and pore pressure feedback. *Journal of Geophysical Research*, 110(F2), F02015. <https://doi.org/10.1029/2004jf000268>
- Iverson, R. M., & Denlinger, R. P. (2001). Flow of variably fluidized granular masses across three-dimensional terrain: I. Coulomb mixture theory. *Journal of Geophysical Research*, 106(B1), 537–552. <https://doi.org/10.1029/2000jb900329>
- Iverson, R. M., & George, D. (2014). A depth-averaged debris-flow model that includes the effects of evolving dilatancy. I. Physical basis. *Proceedings of the Royal Society of London A*, 470(2170), 20130819. <https://doi.org/10.1098/rspa.2013.0819>
- Iverson, R. M., Nakagawa, M., & Luding, S. (2009). Elements of an improved model of debris-flow motion. In *AIP conference proceedings* (Vol. 1145, pp. 9–16). <https://doi.org/10.1063/1.3180101>
- Iverson, R. M., Reid, M., Iverson, N., LaHusen, R., Logan, M., Mann, J., & Brien, D. (2000). Acute sensitivity of landslide rates to initial soil porosity. *Science*, 290(5491), 513–516. <https://doi.org/10.1126/science.290.5491.513>
- Jackson, R. (2000). *The dynamics of fluidized particles*. Cambridge university press.
- Lin, S. (2001). A steady-state capturing method for hyperbolic systems with geometrical source terms. *ESAIM: Mathematical Modelling and Numerical Analysis*, 35(4), 631–645. <https://doi.org/10.1051/m2an:2001130>
- Johnson, C., Kokelaar, B., Iverson, R. M., Logan, M., LaHusen, R., & Gray, J. (2012). Grain-size segregation and levee formation in geophysical mass flows. *Journal of Geophysical Research*, 117(F1), F01032. <https://doi.org/10.1029/2011jf002185>
- Jop, P., Forterre, Y., & Pouliquen, O. (2005). Crucial role of sidewalls in granular surface flows: Consequences for the rheology. *Journal of Fluid Mechanics*, 541(1), 167–192. <https://doi.org/10.1017/s0022112005005987>
- Kaitna, R., Hsu, L., Rickenmann, D., & Dietrich, W. (2011). On the development of an unsaturated front of debris flow. *Italian journal of engineering geology and environment*, 351–358.
- Kellerhals, R. (1967). Stable channels with gravel-paved beds. *Journal of the Waterways and Harbors Division*, 93(1), 63–84. <https://doi.org/10.1061/jwheau.0000482>
- Kowalski, J., & McElwaine, J. N. (2013). Shallow two-component gravity-driven flows with vertical variation. *Journal of Fluid Mechanics*, 714, 434–462. <https://doi.org/10.1017/jfm.2012.489>
- Kurganov, A., & Levy, D. (2002). Central-upwind schemes for the Saint-Venant system. *ESAIM: Mathematical Modelling and Numerical Analysis*, 36(3), 397–425. <https://doi.org/10.1051/m2an:2002019>
- Kurganov, A., & Miller, J. (2014). Central-upwind scheme for Savage–Hutter type model of submarine landslides and generated tsunami waves. *Computational Methods in Applied Mathematics*, 14(2), 177–201. <https://doi.org/10.1515/cmam-2014-0003>
- Kurganov, A., & Petrova, G. (2007). A second-order well-balanced positivity preserving central-upwind scheme for the Saint-Venant system. *Communications in Mathematical Sciences*, 5(1), 133–160. <https://doi.org/10.4310/cms.2007.v5.n1.a6>
- Kurganov, A., & Tadmor, E. (2000). New high-resolution central schemes for nonlinear conservation laws and convection–diffusion equations. *Journal of Computational Physics*, 160(1), 241–282. <https://doi.org/10.1006/jcph.2000.6459>
- Lagrée, P.-Y., Staron, L., & Popinet, S. (2011). The granular column collapse as a continuum: Validity of a two-dimensional Navier–Stokes model with a  $\mu(I)$ -rheology. *Journal of Fluid Mechanics*, 686, 378–408. <https://doi.org/10.1017/jfm.2011.335>
- Leonardi, A., Cabrera, M., Wittel, F. K., Kaitna, R., Mendoza, M., Wu, W., & Herrmann, H. J. (2015). Granular-front formation in free-surface flow of concentrated suspensions. *Physical Review E*, 92(5), 052204. <https://doi.org/10.1103/physreve.92.052204>
- Luca, I., Kuo, C., Hutter, K., & Tai, Y. (2012). Modeling shallow over-saturated mixtures on arbitrary rigid topography. *Journal of Mechanics*, 28(3), 523–541. <https://doi.org/10.1017/jmech.2012.62>
- Mangeney, A., Bouchut, F., Thomas, N., Vilotte, J.-P., & Bristeau, M.-O. (2007). Numerical modeling of self-channeling granular flows and of their levee-channel deposits. *Journal of Geophysical Research*, 112(F2), F02017. <https://doi.org/10.1029/2006jf000469>
- Mangeney-Castelnau, A., Bouchut, F., Vilotte, J.-P., Lajeunesse, E., Aubertin, A., & Pirulli, M. (2005). On the use of Saint Venant equations to simulate the spreading of a granular mass. *Journal of Geophysical Research*, 110(B9), B09103. <https://doi.org/10.1029/2004JB003161>
- Mangeney-Castelnau, A., Vilotte, J.-P., Bristeau, M.-O., Perthame, B., Bouchut, F., Simeoni, C., & Yerneni, S. (2003). Numerical modeling of avalanches based on saint venant equations using a kinetic scheme. *Journal of Geophysical Research*, 108(B11), 2527. <https://doi.org/10.1029/2002jb002024>
- Martin, H. A., Peruzzetto, M., Viroulet, S., Mangeney, A., Lagrée, P.-Y., Popinet, S., et al. (2023). Numerical simulations of granular dam break: Comparison between discrete element, Navier–Stokes, and thin-layer models. *Physical Review E*, 108(5), 054902. <https://doi.org/10.1103/physreve.108.054902>
- Martin, N., Ionescu, I., Mangeney, A., Bouchut, F., & Farin, M. (2017). Continuum viscoplastic simulation of a granular column collapse on large slopes:  $\mu(I)$  rheology and lateral wall effects. *Physics of Fluids*, 29(1). <https://doi.org/10.1063/1.4971320>
- Martinelli, M., & Rohe, A. (2015). Modelling fluidisation and sedimentation using material point method. In *1st Pan-American congress on computational mechanics* (pp. 1–12).
- Meng, X., Johnson, C., & Gray, J. (2022). Formation of dry granular fronts and watery tails in debris flows. *Journal of Fluid Mechanics*, 943, A19. <https://doi.org/10.1017/jfm.2022.400>
- Meng, X., Taylor-Noonan, A., Johnson, C., Take, W., Bowman, E., & Gray, J. (2024). Granular-fluid avalanches: The role of vertical structure and velocity shear. *Journal of Fluid Mechanics*, 980, A11. <https://doi.org/10.1017/jfm.2023.1023>
- Meng, X., & Wang, Y. (2016). Modelling and numerical simulation of two-phase debris flows. *Acta Geotechnica*, 11(5), 1027–1045. <https://doi.org/10.1007/s11440-015-0418-4>
- Meng, X., & Wang, Y. (2018). Modeling dynamic flows of grain–fluid mixtures by coupling the mixture theory with a dilatancy law. *Acta Mechanica*, 229(6), 2521–2538. <https://doi.org/10.1007/s00707-018-2111-9>
- Meng, X., Wang, Y., Feng, F., Wang, C., & Zhou, Y. (2018). Granular flows in a rotating drum and on an inclined plane: Analytical and numerical solutions. *Physics of Fluids*, 30(10), 106605. <https://doi.org/10.1063/1.5045308>
- Meng, X., Wang, Y., Wang, C., & Fischer, J.-T. (2017). Modeling of unsaturated granular flows by a two-layer approach. *Acta Geotechnica*, 12(3), 677–701. <https://doi.org/10.1007/s11440-016-0509-x>

- Mignot, E., Paquier, A., & Haider, S. (2006). Modeling floods in a dense urban area using 2D shallow water equations. *Journal of Hydrology*, 327(1–2), 186–199. <https://doi.org/10.1016/j.jhydrol.2005.11.026>
- Mignotte, M., & Stefanescu, D. (2002). *On an estimation of polynomial roots by Lagrange (Tech. Rep.)*. Technical Report 025/2002. IRMA Strasbourg.
- Nunziato, J., Passman, S., Givler, C., Mactigue, D., & Brady, J. (1986). Continuum theories for suspensions. In R. Arndt, A. Stefan, C. Farrell, & S. N. Peterson (Eds.), *Advancements in aerodynamics, fluid mechanics and hydraulics (Proc. ASCE Special. Conf., Minneapolis, Minn.)*.
- Pailha, M., Nicolas, M., & Pouliquen, O. (2008). Initiation of underwater granular avalanches: Influence of the initial volume fraction. *Physics of Fluids*, 20(11), 111701. <https://doi.org/10.1063/1.3013896>
- Pailha, M., & Pouliquen, O. (2009). A two-phase flow description of the initiation of underwater granular avalanches. *Journal of Fluid Mechanics*, 633, 115–135. <https://doi.org/10.1017/s0022112009007460>
- Pelanti, M., Bouchut, F., & Mangeney, A. (2008). A roe-type scheme for two-phase shallow granular flows over variable topography. *ESAIM: Mathematical Modelling and Numerical Analysis*, 42(5), 851–885. <https://doi.org/10.1051/m2an:2008029>
- Pelanti, M., Bouchut, F., & Mangeney, A. (2011). A Riemann solver for single-phase and two-phase shallow flow models based on relaxation. Relations with Roe and VFRoe solvers. *Journal of Computational Physics*, 230(3), 515–550. <https://doi.org/10.1016/j.jcp.2010.10.001>
- Pellegrino, A., Schippa, L., Guazzelli, E., & Pouliquen, O. (2014). Experiments in shear flow of granular-fluid suspension and dense mixture. In *Proceedings of the international conference on fluvial hydraulics, river flow, Lausanne, Switzerland* (pp. 3–5).
- Peruzzetto, M., Mangeney, A., Bouchut, F., Grandjean, G., Levy, C., Thiery, Y., & Lucas, A. (2021). Topography curvature effects in thin-layer models for gravity-driven flows without bed erosion. *Journal of Geophysical Research: Earth Surface*, 126(4), e2020JF005657. <https://doi.org/10.1029/2020jf005657>
- Pitman, E. B., & Le, L. (2005). A two-fluid model for avalanche and debris flows. *Philosophical Transactions of the Royal Society A: Mathematical, Physical & Engineering Sciences*, 363(1832), 1573–1601. <https://doi.org/10.1098/rsta.2005.1596>
- Poullain, P., Friant, A. L., Mangeney, A., Viroulet, S., Fernandez-Nieto, E., Castro Diaz, M., et al. (2023). Performance and limits of a shallow-water model for landslide-generated tsunamis: From laboratory experiments to simulations of flank collapses at Montagne Pelée (Martinique). *Geophysical Journal International*, 233(2), 796–825. <https://doi.org/10.1093/gji/ggac482>
- Pouliquen, O., & Forterre, Y. (2002). Friction law for dense granular flows: Application to the motion of a mass down a rough inclined plane. *Journal of Fluid Mechanics*, 453, 133–151. <https://doi.org/10.1017/s0022112001006796>
- Pudasaini, S. P. (2012). A general two-phase debris flow model. *Journal of Geophysical Research*, 117(F3), F03010. <https://doi.org/10.1029/2011jf002186>
- Rauter, M. (2021). The compressible granular collapse in a fluid as a continuum: Validity of a Navier-Stokes model with  $\mu(J)$ ,  $\phi(J)$ -rheology. *Journal of Fluid Mechanics*, 915, A87. <https://doi.org/10.1017/jfm.2021.107>
- Rocha, F., Johnson, C., & Gray, J. (2019). Self-channelisation and levee formation in monodisperse granular flows. *Journal of Fluid Mechanics*, 876, 591–641. <https://doi.org/10.1017/jfm.2019.518>
- Rondon, L., Pouliquen, O., & Aussillous, P. (2011). Granular collapse in a fluid: Role of the initial volume fraction. *Physics of Fluids*, 23(7), 073301. <https://doi.org/10.1063/1.3594200>
- Roux, S., & Radjai, F. (1997). Texture-dependent rigid plastic behaviour. In H. Herrmann (Ed.), *Proceedings: Physics of dry granular media* (pp. 305–311). Kluwer.
- Roux, S., & Radjai, F. (2001). Statistical approach to the mechanical behavior of granular media. In H. A. J. Phillips (Ed.), *Mechanics for a new millennium* (pp. 181–196). Kluwer.
- Sarno, L., Tai, Y.-C., Wang, Y., & Oberlack, M. (2021). A well-posed multilayer model for granular avalanches with  $\mu(i)$ -rheology. *Physics of Fluids*, 33(10), 103319. <https://doi.org/10.1063/5.0065697>
- Sarno, L., Wang, Y., Tai, Y.-C., Martino, R., & Carravetta, A. (2021). Asymptotic analysis of the eigenstructure of the two-layer model and a new family of criteria for evaluating the model hyperbolicity. *Advances in Water Resources*, 154, 103966. <https://doi.org/10.1016/j.advwatres.2021.103966>
- Savage, S. B., & Hutter, K. (1989). The motion of a finite mass of granular material down a rough incline. *Journal of Fluid Mechanics*, 199, 177–215. <https://doi.org/10.1017/s0022112089000340>
- Savage, S. B., & Iverson, R. (2003). Surge dynamics coupled to pore-pressure evolution in debris flows. In D. Rickenmann & C. L. Chen (Eds.), *Proc. 3rd int. conf. on debris-flow hazards mitigation: Mechanics, prediction, and assessment, Davos, Switzerland* (pp. 503–514). Millpress, Rotterdam.
- Sun, W. (2024). Modeling phase separation in grain-fluid mixture flows by a depth-averaged approach with dilatancy effects [Dataset]. <https://doi.org/10.48328/tudatalib-1619>
- Sun, W., Meng, X., Wang, Y., Hsiao, S., & You, Z. (2023). A depth-averaged description of submarine avalanche flows and induced surface waves. *Journal of Geophysical Research: Earth Surface*, 128(4), e2022JF006893. <https://doi.org/10.1029/2022jf006893>
- Tai, Y., Heß, J., & Wang, Y. (2019). Modeling two-phase debris flows with grain-fluid separation over rugged topography: Application to the 2009 hsiainlin event, Taiwan. *Journal of Geophysical Research: Earth Surface*, 124(2), 305–333. <https://doi.org/10.1029/2018jf004671>
- Taylor-Noonan, A. M., Bowman, E. T., McArdeil, B. W., Kaitna, R., McElwaine, J. N., & Take, W. A. (2022). Influence of pore fluid on grain-scale interactions and mobility of granular flows of differing volume. *Journal of Geophysical Research: Earth Surface*, 127(12), e2022JF006622. <https://doi.org/10.1029/2022jf006622>
- Terzaghi, K. (1943). *Theoretical soil mechanics*. John Wiley and Sons.
- Truesdell, C. (1984). *Rational thermodynamics*. Springer.
- Trujillo-Vela, M. G., Ramos-Cañón, A. M., Escobar-Vargas, J. A., & Galindo-Torres, S. A. (2022). An overview of debris-flow mathematical modelling. *Earth-Science Reviews*, 232, 104135. <https://doi.org/10.1016/j.earscirev.2022.104135>
- Vallejo, L. (1997). Surge wave development in debris flows. *Soils and Foundations*, 37(4), 115–119. [https://doi.org/10.3208/sandf.37.4\\_115](https://doi.org/10.3208/sandf.37.4_115)
- Wang, Y., Hutter, K., & Pudasaini, S. P. (2004). The Savage-Hutter theory: A system of partial differential equations for avalanche flows of snow, debris, and mud. *ZAMM-Journal of Applied Mathematics and Mechanics/Zeitschrift für Angewandte Mathematik und Mechanik: Applied Mathematics and Mechanics*, 84(8), 507–527. <https://doi.org/10.1002/zamm.200310123>
- Wartman, J., Montgomery, D. R., Anderson, S. A., Keaton, J. R., Benoît, J., dela Chapelle, J., & Gilbert, R. (2016). The 22 march 2014 Oso landslide, Washington, USA. *Geomorphology*, 253, 275–288. <https://doi.org/10.1016/j.geomorph.2015.10.022>
- Wieland, M., Gray, J., & Hutter, K. (1999). Channelized free-surface flow of cohesionless granular avalanches in a chute with shallow lateral curvature. *Journal of Fluid Mechanics*, 392, 73–100. <https://doi.org/10.1017/s0022112099005467>
- Zanuttigh, B., & Lamberti, A. (2007). Instability and surge development in debris flows. *Reviews of Geophysics*, 45(3), RG3006. <https://doi.org/10.1029/2005rg000175>